Fundamental Properties of Molecules on Surfaces

Molecular Switching and Interaction of Magnetic Molecules with Superconductors

Nino Hatter

im Fachbereich Physik
der Freien Universität Berlin
eingereichte Dissertation

Berlin, 2016

Diese Arbeit entstand in der Arbeitsgruppe von Prof. Dr. Katharina J. Franke am Fachbereich Physik der Freien Universität Berlin.

Berlin, 28.10.2016

Erstgutachterin: Prof. Dr. Katharina J. Franke
Zweitgutachter: Prof. Dr. Martin Wolf

Datum der Disputation: 14.12.2016

Kurzfassung

Die vorliegende Dissertation beschäftigt sich mit einzelnen molekularen Schaltern sowie mit metallorganischen Molekülen auf Oberflächen. Diese Systeme werden mithilfe von Rastertunnelmikroskopie (STM) und Rastertunnelspektroskopie (STS) untersucht. Ein Schwerpunkt der Arbeit liegt in der Untersuchung der Schaltbarkeit und des zugrundeliegenden Schaltmechanismus eines Diarylethenmoleküls auf der Ag(111) Oberfläche. Einen weiteren Schwerpunkt bildet die Auflösung und die gezielte Änderung der magnetischen Wechselwirkung einzelner Moleküle mit Supraleitern.

Ein Musterbeispiel eines photochromen molekularen Schalters ist *4,4'-(4,4'-(perfluorocyclopent-1-ene-1,2-diyl)bis(5-methylthiophene-4,2-diyl)dipyridine* (PDTE). Mit der STM-Spitze können einzelne PDTE Moleküle auf der Ag(111)-Oberfläche verändert werden. Dabei ändert sich die Struktur der Moleküle und die elektronische Bandlücke zwischen besetzen und unbesetzten Orbitalen wird verringert. Berechnungen mithilfe von Dichtefunktionaltheorie (DFT) zeigen, dass die induzierte Änderung eine Ringschlussreaktion des PDTE von einem offenen, flach adsorbierten, in ein geschlossenes Isomer in einer *cis* Konfiguration ist. Das Reaktionsprodukt wird durch Dispersionswechselwirkungen mit der Oberfläche thermodynamisch stabilisiert. Eine lineare Abhängigkeit der Schaltspannung vom Abstand zwischen Spitze und Probe wird beobachtet, wobei eine Mindestspannung von 1.4 V zum Schalten nötig ist. Dies deutet auf eine Kombination aus elektrischem Feld und Tunnelelektronen als Ursache des Schaltens hin. DFT-Rechnungen offenbaren eine hohe Energiebarriere für die Ringschlussreaktion vom offenen, flach adsorbierten Isomer in die geschlossene *cis* Form.

Die Wechselwirkung zwischen magnetischen Molekülen und Supraleitern wird an Mangan-Phthalocyanin (MnPc), adsorbiert auf einer Pb(111) Oberfläche, untersucht. Bei einer Temperatur von 1.2 K werden Tripletts von Shiba-Zuständen in der supraleitenden Energielücke beobachtet. Verschiedene Adsorptionsplätze von MnPc auf Pb(111) ermöglichen die Untersuchung einer großen Bandbreite von Austauschwechselwirkungen und folglich Shiba-Zuständen bei verschiedenen Energien. Die Aufspaltung in Tripletts ist ein Indiz für magnetische Anisotropy in diesem System, die unterschiedliche Spin-Projektionen energetisch aufspaltet. Zudem können wir einen Phasenübergang zwischen einem "Kondo-geschirmten" und einem "ungeschirmten" Grundzustand beobachten, der durch die Änderung der relativen Intensitäten der Shiba-Zustände am Phasenübergang deutlich wird. Im "Kondo-geschirmten" Grundzustand besitzen alle drei Shiba-Zustände gleiche relative Intensitäten. Dieses Verhalten deutet auf einen Spin von $S = 1/2$ im Grundzustand hin. Die Shiba-Zustände entsprechen Anregungen des Systems in einen Zustand mit einem Spin von $S = 1$, welcher energetisch in drei Niveaus aufgespalten ist. Im "ungeschirmten" Grundzustand hingegen verhalten sich die Intensitäten der Shiba-Zustände gemäß einer Boltzmannverteilung. Dieses Verhalten kann mit einer thermischen Besetzung der aufgespalteten Grundzustandsniveaus des Systems erklärt werden, das nun einen Spin von $S = 1$ besitzt.

Zusätzlich wird Ammoniak auf das auf Pb(111) adsorbierte MnPc aufgedampft, welches direkt an das Mangan bindet. Bei 1.2 K tritt nur ein Paar von Shiba-Zuständen in der supraleitenden Energielücke auf. Die Shiba-Zustände sind dicht am Rand der Energielücke und weisen eine höhere Intensität bei positiver Energie auf. Weitere Shiba-Zustände werden bei erhöhter Temperatur sichtbar. Die Energieaufspaltung der Shiba-Tripletts für MnPc-NH_3 ist größer als für reines MnPc. Das Verhalten der relativen Intensitäten lässt schlussfolgern, dass sich alle MnPc Moleküle mit Ammoniak im "ungeschirmten" Grundzustand mit einem Spin von $S = 1$ befinden. Das Mangan wird durch die Bindung zu Ammoniak elektronisch von der Oberfläche entkoppelt. Im normalleitenden Zustand ist eine Resonanz um die Fermienergie sichtbar als Effekt von Kondo-Austauschprozessen des Spins von Mangan mit den Spins der Leitungselektronen im Substrat. Das Temperaturverhalten der Resonanz deutet auf eine sehr schwache Wechselwirkung hin. Zusätzlich sind auf dieser Resonanz inelastische Spinanregungen sichtbar. Die Energieverschiebung der Anregungen in einem äußeren Magnetfeld bestärkt die Annahme des Spinzustandes von $S = 1$.

Abstract

In this thesis, we investigate individual molecular switches and metal-organic complexes on surfaces with scanning tunneling microscopy (STM) and spectroscopy (STS) at low temperatures. One focus addresses the switching ability and mechanism of diarylethene on Ag(111). The other focus lies on resolving and tuning magnetic interactions of individual molecules with superconductors.

4,4'-(4,4'-(perfluorocyclopent-1-ene-1,2-diyl)bis(5-methylthiophene-4,2-diyl)dipyridine (PDTE) is a prototypical photochromic switch. We can induce a structural change of individual PDTE molecules on Ag(111) with the STM tip. This change is accompanied by a reduction of the energy gap between the occupied and unoccupied molecular orbitals. Density functional theory (DFT) calculations reveal that the induced switching corresponds to a ring-closing reaction from an open isomer in a flat adsorption configuration to a ring-closed isomer with its methyl groups in a *cis* configuration. The final product is thermodynamically stabilized by strong dispersion interactions with the surface. A linear dependence of the switching threshold with the tip-sample distance with a minimal threshold of 1.4 V is found, which we assign to a combination of an electric-field induced process and a tunneling-electron contribution. DFT calculations suggest a large activation barrier for a ring-closing reaction from the open flat configuration into the closed *cis* configuration.

The interaction of magnetic molecules with superconductors is studied on manganese phthalocyanine (MnPc) adsorbed on Pb(111). We find triplets of Shiba states inside the superconducting gap. Different adsorption sites of MnPc provide a large variety of exchange coupling strengths, which lead to a collective energy shift of the Shiba triplets. We can assign the splitting of the Shiba states to be an effect of magnetic anisotropy in the system. A quantum phase transition from a "Kondo screened" to a "free spin" ground state is observed. At the point of the phase transition, the relative intensities of the Shiba states in the triplets change. In the "Kondo screened" ground state, equal relative intensities of the Shiba states are a manifestation of a spin of 1/2 in the ground state, where the Shiba states correspond to excitations to an anisotropy-split excited state with a spin of $S = 1$. In the "free spin" ground state, the relative intensities follow a Boltzmann distribution, which indicates a thermal occupation of energy-split ground state levels of the $S = 1$ state.

In the last experiment, we deposited ammonia to MnPc on Pb(111). Ammonia coordinates to the central Mn ion. At 1.2 K, only one pair of Shiba states is found at energies close to the superconducting gap edge and with higher intensity at positive energies. By increasing the temperature, up to three Shiba states appear. They exhibit a larger energy splitting compared to pure MnPc on Pb(111) and their relative intensity distribution suggests that all MnPc-NH_3 are in the "free spin" ground state with a spin of $S = 1$. We conclude that ammonia leads to a reduction of the exchange coupling strength to the surface. A zero-bias resonance is observed in the normal conducting state, which is attributed to spin correlations in the weak coupling Kondo regime. Inelastic spin excitations are superimposed on this zero-bias resonance. Their characteristic shift in a magnetic field confirms the spin state of $S = 1$.

Contents

Chapter 1

Introduction

The Nobel prize in chemistry in 2016 has been awarded to the three scientists Jean-Pierre Sauvage, Sir J. Fraser Stoddart and Bernard L. Feringa for their groundbreaking works on molecular machines [1]. This choice confirms the importance of new approaches in the quest to develop more powerful devices. The famous "nano car", which was developed in 2011 [2], is an impressive example of the functionalization of single molecules on surfaces. Already in 1974, Aviram and Ratner proposed a molecular rectifier based on a charge transfer complex [3]. Since then, numerous studies have shown the feasibility of different molecular electronics building blocks, such as single-molecule transistors [4], single-atom transistors [5] or ultra dense memory circuits based on bistable rotaxanes [6]. The advantages of these tiny machines on the performance are manifold and include, *e.g.*, a higher density, higher processing speed, specific assembly due to intermolecular interaction and new functionalities arising from quantum effects [7]. These attributes might be especially useful for portable electronic devices, body implants or even space missions [8].

The field of molecular engineering was already mentioned in the 1950s by A. von Hippel, who proposed that electronic devices should be built from scratch by assembling atoms in order to attain the desired functionality [9]. An important prerequisite is the enhancement of techniques for the chemical synthesis. Nowadays, functional groups at molecules can be changed nearly at will and therefore the purpose of a single molecule can be adapted or substantially changed [10]. The array of available single-molecule machines comprises molecular motors [11–13] and molecular switches [14–18] that can be reversibly switched between their configurations by light, an electric field, chemical stimuli or tunneling electrons.

Despite the rapid progress in recent years, there are still many obstacles to overcome in order to built fully functional circuits that can compete with semiconductor-based electronics. The influence of a supporting surface plays a crucial role in this matter, as it can donate/accept charge to/from the adsorbed molecules via charge transfer [19, 20]. Additionally, upon adsorption, the electronic structure of the molecule is altered [21]. All these interactions with the substrate can substantially change the properties of the molecules and might impact the switching behavior [22], reverse the thermal stability of the reaction educt and product [23] or inhibit a back switching [24].

The study of these systems is only possible thanks to the development of powerful experimental techniques. Among those, scanning tunneling microscopy (STM) holds a special role, as it en-

ables the real-space imaging of molecular and atomic structures on conducting substrates or thin insulating layers [25–27]. It is not only suited to probe a given system, but can be actively used to assemble structures from scratch in a bottom-up approach [28–31]. Additionally, scanning tunneling spectroscopy (STS) is employed to obtain information about the internal electronic structure of nanometer-sized objects as well as fingerprints of their interaction with the surface.

We make use of the capabilities of the STM to study the switching behavior of photochromic *4,4'-(4,4'-(perfluorocyclopent-1-ene-1,2-diyl)bis(5-methylthiophene-4,2-diyl)dipyridine* (PDTE), induced by the STM tip (presented in chapter 4). We study the adsorption behavior of PDTE on the Ag(111) surface. Our measurements are complemented by density functional theory (DFT) calculations of the adsorption energies and thermal stabilities of possible isomers. By this, we get a clear picture of the influence of the underlying surface on the stability of the different isomers. At last, we explore the mechanisms involved in the ring-closing reaction and try to understand, why the back reaction is not seen in the STM studies.

Besides the use of atoms and molecules as active elements in nanoelectronic circuits, there is great demand to read and write information with increasingly high densities. In this respect, the STM has been used to rearrange vacancies on a chlorinated Cu(100) surface in order to write a kilobyte of information on a surface area of just a few nm^2 [32]. The storage density reached with this method was $502 Tb/in^2$, which is nearly 500 times more than densities of up-to-date hard disks [33].

Conventional storage devices rely on the magnetic properties of a material and the information is stored by differently magnetizing certain areas of the hard disc. Shrinking the size of these magnetic domains leads to their thermal instability and information can not be stored for sufficiently long time.

An alternative approach for high-density storage devices and electronic devices deals with magnetism in single atoms and molecules, which originates from the electron spin. The idea is to store information in the spin state of a single atom or molecule. However, in an isotropic environment, each direction of the spin is equally likely. In order to get two different spin states, which are separated by a potential barrier, an anisotropic environment needs to be created. This can be achieved, for example, by using an anisotropic surface [34, 35], exchange coupling to other spins on the surface [36] or molecular ligands around the central metal ion [37].

Brought on a metallic surface, electrons in the surface will interact with the atomic spin and thereby screen the spin, which might lead to the formation of a non-magnetic ground state [38]. This screening of the impurity spin is known as the Kondo effect. At the same time, the polarizability of surface electrons transmits the exchange coupling between two separate spins on the surface via the so-called Rudermann-Kittel-Kasuya-Yosida (RKKY) interaction [39, 40], which is characterized by a specific oscillatory distance dependence. Linear chains of a few atoms coupled via this RKKY interaction have been used to perform simple logic operations [41]. However, in order to stabilize the magnetization of these chains, they need to be coupled to a ferromagnetic electrode. An insulating layer can be used to decouple the electronic states of the impurity from the surface and restore the spin state and the bistability [42, 43]. A precise understanding of the interaction of spins in atoms and molecules with the substrate is necessary to taylor systems where this property can be applied.

An especially well-suited system to study the effects of exchange interaction are superconductors. There, the formation of bound pairs of electrons opens a superconducting gap around the Fermi level. The exchange interaction of a magnetic impurity with the superconducting quasiparticles induces localized states inside the superconducting gap, which are called Yu-Shiba-Rusinov (Shiba) states [44–46]. Their energy is a precise measure of the exchange coupling strength. For such studies, quantum dots can be tuned in order to access different coupling regimes and spin states [47, 48]. Another approach consists of magnetic atoms on superconducting surfaces, where Shiba states have been observed in the vicinity of the atoms [49, 50]. The interaction can be tuned by an organic ligand surrounding the central ion, which changes the exchange coupling and induces magnetic anisotropy for systems with spin $S \geq 1$. In these systems, intermolecular interactions can drive the formation of molecular islands and therefore provide many different adsorption sites on the substrate. This is related to a large variety of exchange coupling strengths [51, 52]. Additionally, if the ligand design is such that the coupling to the substrate is very weak, the superconducting gap preserves excited spin states for much longer times than on normal metallic substrates [53].

In chapter 5 and 6, we investigate the interaction of metal-organic complexes with quasiparticles in the superconductor Pb. We start by characterizing the Shiba states induced by manganese phthalocyanine (MnPc) on Pb(111) in chapter 5. For an increased spectral resolution on the subgap structure, we employ superconducting STM tips. At temperatures of 1.2 K, triplets of Shiba states are resolved. We assign the origin of these multiple Shiba states to a splitting in the presence of magnetic anisotropy. Depending on the adsorption site of the different MnPc molecules, a collective shift of the triplets is found. By analyzing the relative intensities of the Shiba states, a change in the behavior is found when the Shiba states cross the Fermi level. This change can be associated with a phase transition of the system from a “Kondo screened“ ground state to a “free spin“ ground state. We can unambiguously determine the spin state of both ground states.

In chapter 6, we manipulate this system of MnPc on Pb(111) by adsorbing ammonia, which coordinates to the central Mn ion. A reduction of the exchange coupling strength is found, evidenced by the change of the Shiba state energies and splittings in the superconducting state. In contrast to MnPc, all MnPc-NH_3 molecules are found in the “free spin“ ground state, which is confirmed by a thermal occupation of anisotropy split ground state levels. When investigating the normal state behavior, we find a strong resonance around the Fermi level, which is usually an indication of an efficient Kondo screening. However, its temperature dependence leads to the conclusion that the impurity spin is only weakly coupled to the substrate electron bath. Additionally, a narrow dip is superimposed on the resonance. We analyze the nature of this dip around the Fermi level in a magnetic field. The evolution into symmetric steps and their characteristic shift in a magnetic field confirms their nature as inelastic spin excitations of a system with a ground state spin of $S = 1$. With this analysis, we are able to characterize the effect of ammonia as axial ligand on the interaction of MnPc with Pb in both the superconducting state and the normal state. This research provides essential information on how to control the spin state and interaction of magnetic molecules with superconductors.

To lay the foundation for the following experiments, the thesis starts with an introduction to the basic principles of scanning tunneling microscopy as well as spectroscopy in chapter 2. There, also the experimental setup will be introduced.

Chapter 3 provides a brief introduction to magnetic anisotropy, which is responsible for paramagnetism in atoms and molecules. Moreover, the Kondo effect will be explained, as it plays an important role in the interaction of magnetic impurities with metallic substrates. The second part of this chapter describes the Bardeen-Cooper-Schrieffer (BCS) theory of superconductivity and the formation of Shiba states, when magnetic impurities are placed on superconductors.

Chapter 2

Theory and Experimental Setup

Before the 1980s, the structure and electronic properties of molecules adsorbed on surfaces could only be investigated for large ensembles and in reciprocal space. Techniques, such as low-energy electron diffraction (LEED) and angle-resolved photoemission spectroscopy (ARPES) provided information on the structure and the electronic properties with spot sizes in the order of μm. Real-space information was not available until the invention of scanning tunneling microscopy (STM) by Binnig, Rohrer and Weibel in 1982 [26]. The STM consists of a sharp metallic tip scanning across a conducting substrate. It provides a spatial resolution beyond the optical limit and allows the investigation of single molecules or atoms. Additionally, using scanning tunneling spectroscopy (STS), information about the electronic structure around the Fermi energy (E_F).

Due to its versatility, scanning tunneling microscopy is still an actively evolving technique and new possible applications are explored. Inelastic electron tunneling spectroscopy (IETS), for example, is used to investigate molecular vibrations [54, 55] or spin-flip excitations [56]. More recently, a combination of STM measurements with X-ray magnetic circular dichroism (XMCD) has shown element sensitivity on single adatoms, a lacking feature in the past [57].

In this chapter, we introduce the basic concepts of scanning tunneling microscopy and spectroscopy. First, we describe the working principle of the STM. Then, we give a brief derivation of the tunneling current as well as of the differential conductance, which is measured by scanning tunneling spectroscopy and is proportional to the local density of states. Additionally, inelastic electron tunneling spectroscopy is explained. At the end of this chapter, the experimental setup is described.

2.1 Scanning Tunneling Microscopy

The essential part of a scanning tunneling microscope is the scanning head. It consists of an atomically sharp tip in close proximity (usually a few Å) to a conducting substrate. The vacuum gap between the tip and the sample constitutes a potential barrier for electrons to cross from one electrode to the other.

In a classical picture, electrons can not traverse this barrier, unless their energy is sufficiently high to overcome it. This energy corresponds to the work function of the surface or the tip, respectively. However, electrons are quantum mechanical objects, thus they exhibit a wave-like nature. This enables a process known as tunnel effect, where the wave function of the electron penetrates the potential barrier. A typical schematic of an electron wave is shown in Fig. 2.1(a). The electron is represented by the blue sinusoidal wave on the left of the potential barrier of height V_0. Inside the classically forbidden barrier region the wave decays exponentially. If the barrier is sufficiently narrow, there is a finite transmission probability that the electron crosses the barrier. The transmission probability depends exponentially on the barrier thickness which is associated with the distance between the tip and the sample. If no bias is applied between the tip and the sample, the tunneling currents from both sides are equal and no net current is flowing. In order to measure a directional current, a finite bias has to be applied. We will give a derivation of the tunneling current in the next section. Here, we will introduce some basic scanning modes used in STM measurements.

In most experimental setups, the bias is applied to the sample while the tip is connected to a virtual ground. A piezoelectric element, to which the tip is attached, regulates the lateral position and the height of the scanning tip. To this end, the piezoelectric crystal is normally divided into five segments, as shown in Fig. 2.1(b). Each segment is contacted by an electrode and a voltage is applied between opposite electrodes. This arrangement allows the motion of the tip along the x- and y-axis, as seen in the inset in Fig. 2.1(b). The central segment is controls the vertical position of the tip, thus regulates the distance of the tip from the sample.

Two main scanning modes are employed for the imaging process. More widely used is the constant-current mode, which requires an internal feedback loop. During scanning, the tunneling current is regulated. The feedback adjusts the voltage of the z-piezo in order to keep a constant tunneling current, thus reproducing the surface structure, as shown in Fig. 2.1(c). To visualize the surface topography, the voltage applied at the z-piezo is recorded for each point of the scan. All values are converted into an image, which is related to the apparent height of the atomic structure measured. This scanning mode is preferred for large structures and rough surfaces, as the tip adjusts to the sample structure.

The second mode is called constant-height scanning mode. During the scan, the feedback is disabled. The tip sweeps across the surface in the same height (see Fig. 2.1(d)). Instead of the piezo voltage, now the tunneling current is recorded and its values converted into an image. This mode requires rather flat surfaces in order for the tip not to crash into the surface. The advantage of this mode is a faster scanning speed. However, to obtain images of molecules on surfaces, the constant-current mode is preferred and will be throughout this thesis.

2.1.1 Derivation of the Tunneling Current

One of the key observables in scanning tunneling microscopy is the tunneling current. Intuitively, it is clear that this tunneling current depends on the applied bias as well as the density of states in the sample and tip. Due to the importance of the tunneling current, a short derivation shall be given here.

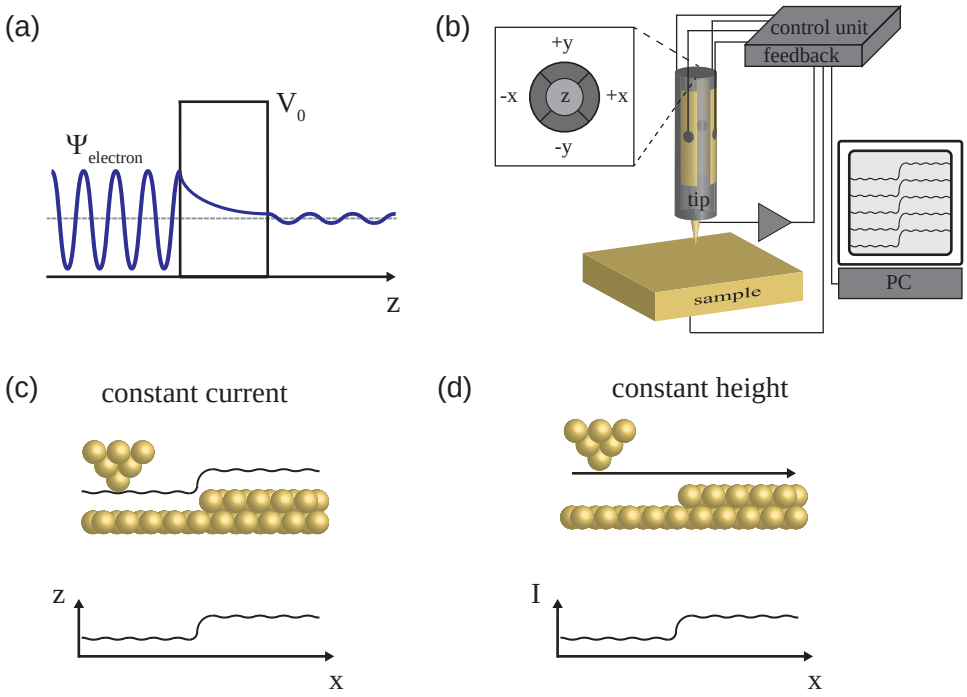

Figure 2.1: (a) Illustration of the tunnel effect. An electron, modeled as a wave (Ψ_{electron}) hits a potential barrier of height V_0. The electron can tunnel through the barrier with a certain probability. (b) A simplified scheme of an STM to illustrate the working principle. Shown is the tip attached to a piezo crystal, which is contacted to an electronically operated feedback loop and the equipment for visualization. Inset: Segments of the piezo crystal to implement motion in all three spatial directions. (c) Tip-sample scheme in constant-current scanning mode with output of the apparent height, here z. (d) As (c), but for constant-height scanning mode, where the tunneling current I is recorded.

In a tunnel junction, in which both electrodes have the same work function, at zero applied bias voltage the tunnel rates between the two electrodes are equal to each other. In experiments, a small bias voltage is applied to one electrode. A scheme of the density of states (DOS) of tip and sample is shown in Fig. 2.2(a), where a positive voltage is applied to the sample. As a consequence, the Fermi level of the sample is shifted down by eV with respect to the Fermi level of the tip. At positive bias, electrons tunnel from the occupied states of the tip into the unoccupied states of the sample. At negative bias, electrons tunnel from the sample into the tip. The tunneling current across the junction is the sum of all tunneling processes from the sample to the tip and vice versa. Tersoff and Hamann developed a theoretical model addressing this problem. They assumed two independent systems representing the tip and the surface with non-orthogonal eigenstates of the tip, ψ_μ, and sample, ψ_ν. In first-order perturbation theory the

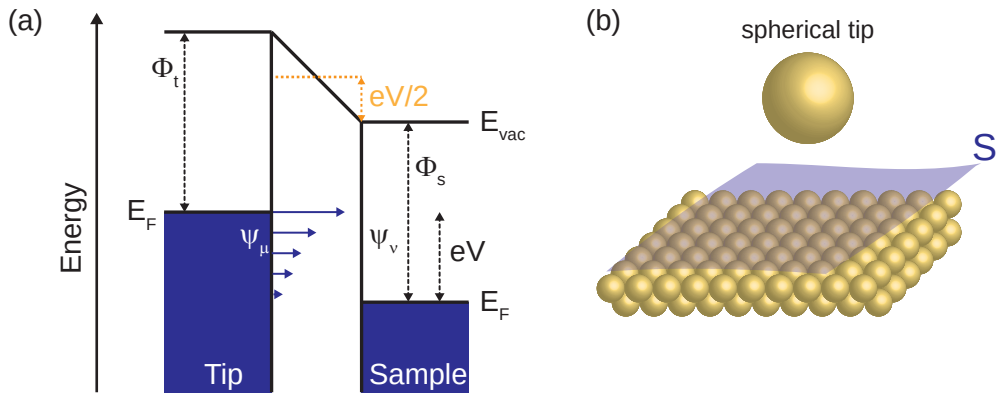

Figure 2.2: Model used to describe the tunneling current for a metal-insulator metal junction. (a) Sample and tip DOS are separated by a vacuum barrier and a bias voltage is applied at the tip. Electrons can tunnel from the tip to the sample (blue arrows). The vacuum barrier is assumed to be rectangular (orange). The work functions of the tip Φ_t and the sample Φ_s are shown as well as the states in the tip and the sample, Ψ_t and Ψ_s, respectively. (b) Model used to treat the tunnel junction with a spherical tip in front of a flat surface. Integration is performed over the surface area within the vacuum barrier (blue plane).

tunneling current is given by the expression obtained by Bardeen [58, 59],

$$I_\mathrm{t} = \frac{2\pi e}{\hbar} \sum_{\mu,\nu} f(E_\mu)\left[1 - f(E_\nu + eV)\right] |M_{\mu\nu}|^2 \delta(E_\mu - E_\nu). \tag{2.1}$$

Here, $f(E)$ is the Fermi-Dirac distribution and V the applied bias voltage. The tunnel matrix element $M_{\mu\nu}$ is associated with the transmission probability between tip and sample states. Eq. (2.1) takes into account only elastic tunneling processes, which is ensured by the delta function in which E_μ and E_ν are the energies of tip and sample states, respectively. The tunnel matrix element is given as [58]

$$M_{\mu\nu} = \frac{\hbar^2}{2m} \int d\vec{S} \cdot (\psi_\mu^* \vec{\nabla} \psi_\nu - \psi_\nu \vec{\nabla} \psi_\mu^*), \tag{2.2}$$

with the integration performed over a surface S, which is entirely within the vacuum barrier region (light blue surface sheet in Fig. 2.2(b)). The term in parentheses is the so-called current operator. To obtain a solution for finite but small bias values, the semi-classical WKB (Wentzel-Kramer-Brillouin) approximation is used. In this approximation, the potential barrier is divided into many small rectangular potential barriers. In a simplified model, we replace the barrier at a finite bias voltage by one rectangular barrier with height $\Phi_\mathrm{s} + eV/2$ at the sample side [60]. At the tip side, the barrier is effectively reduced to $\Phi_\mathrm{t} - eV/2$, marked by the orange line in Fig. 2.2(a). With the surface being inside the vacuum barrier, the two effects cancel out and the solution

should give a good approximation to the exact matrix element. It results in [60, 61]

$$|M_{\mu\nu}|^2 \propto exp\left\{-2z\frac{\sqrt{2m}}{\hbar}\sqrt{\Phi+\frac{eV}{2}-E}\right\} \tag{2.3}$$

where Φ is now the average work function. For equal tip and sample work functions, $\Phi{=}\Phi_\mathrm{s}{=}\Phi_\mathrm{t}$. We can now simplify Eq. (2.1), first by replacing the sum over all states by an integration over the energies, as the tunnel matrix element depends only on the state energies. The result reads

$$I_\mathrm{t} = \frac{2\pi e}{\hbar}\int_{-\infty}^{+\infty} dE_\mu \int_{-\infty}^{+\infty} dE_\nu \rho_\mathrm{t}(E_\mu)\rho_\mathrm{s}(E_\nu+eV)f(E_\mu)\left[1-f(E_\nu+eV)\right]|M_{\mu\nu}|^2\delta(E_\mu-E_\nu). \tag{2.4}$$

In this equation, $\rho_\mathrm{s}(E)$ and $\rho_\mathrm{t}(E)$ are the density of states (DOS) of the sample and the tip, respectively. They correspond to the number of states at a given energy E. The δ-function is now taken into account by performing the integration over one variable, here E_ν, and renaming the other $E_\mu = E$. Eq. (2.4) now becomes

$$I_\mathrm{t} = \frac{2\pi e}{\hbar}\int_{-\infty}^{+\infty} dE_\mu \rho_\mathrm{t}(E_\mu)\rho_\mathrm{s}(E_\mu+eV)f(E_\mu)\left[1-f(E_\mu+eV)\right]|M_{\mu\nu}|^2. \tag{2.5}$$

Only tip states in the energy interval from $E_\mathrm{F}-eV$ to E_F contribute to a net tunneling current. This is equivalent to sample states in the energy range from E_F to $E_\mathrm{F}+eV$, which will be more handy for later derivations. The integral has to be evaluated within these limits. Assuming low temperatures, which is reasonable in the present experiments, the Fermi-Dirac distribution becomes a step and leads to $f(E_\mathrm{F}) \approx 1$, $f(E_\mathrm{F}+eV) \approx 0$. With this simplification, we obtain

$$I_\mathrm{t} = \frac{2\pi e}{\hbar}\int_{E_\mathrm{F}}^{E_\mathrm{F}+eV} dE \rho_\mathrm{t}(E-eV)\rho_\mathrm{s}(E)|M_{\mu\nu}|^2. \tag{2.6}$$

This result exhibits some crucial features of the tunneling current. Firstly, the exponential dependence of the tunneling current on the barrier thickness is implicitly included in the tunneling matrix element. Secondly, apart from the distance dependence, the tunneling current also depends on the density of states in the tip and the sample. Atomic or molecular orbitals of an adsorbate will contribute to the tunneling current hence alter the recorded topography. Therefore, the image obtained in a scan is a combination of the topography of the sample and the electronic structure of the system under investigation. We refer to the height obtained in STM measurements as apparent height in the remainder of this thesis. The dependence of the tunneling current on the density of states can be taken advantage of to investigate the electronic structure of the system in detail.

2.2 Scanning Tunneling Spectroscopy

Besides the topographic information about the surface and adsorbates, scanning tunneling spectroscopy (STS) may be recruited to probe the local density of states (LDOS) of the system. The advantage of the STM is that local variations in the density of states can be detected within, *e.g.*, a single molecule.

2.2.1 Local Density of States

From the expression for the tunneling current, its dependence on the DOS of both the tip and the sample becomes evident. Generally speaking, it is the weighted sum of all states from E_F up to the applied bias voltage. If we take the derivative of the tunneling current in Eq. (2.6) with respect to the bias voltage V, we obtain

$$\begin{aligned}\frac{dI_\mathrm{t}}{dV} &\propto \rho_t(E_F)\rho_s(E_F+eV)|M_{\mu\nu}|^2 \\ &+ \int_{E_\mathrm{F}}^{E_\mathrm{F}+eV} dE\rho_t(E-eV)\rho_s(E)\frac{\mathrm{d}|M_{\mu\nu}|^2}{\mathrm{d}V} \\ &+ \int_{E_\mathrm{F}}^{E_\mathrm{F}+eV} dE\rho_s(E)\frac{\mathrm{d}\rho_t(E')}{\mathrm{d}E'}|M_{\mu\nu}|^2.\end{aligned} \tag{2.7}$$

Assuming small bias voltages and a constant tip-sample distance, the tunnel matrix element is approximately constant and its derivative vanishes. An ideal setup for tunneling spectroscopy is when the tip shows no sharp features around E_F and its DOS is constant. In this case, the derivative of $\rho_\mathrm{t}(E)$ becomes zero and the third term in Eq. (2.7) disappears as well. The result is a signal proportional to the density of states of the sample,

$$\frac{dI_t}{dV} \propto \rho_s(E_\mathrm{F}+eV) \tag{2.8}$$

with $|M_{\mu\nu}|^2$ and $\rho_\mathrm{t}(E_\mathrm{F})$ being constant, therefore omitted here.

In scanning tunneling spectroscopy, the differential conductance ($\mathrm{d}I/\mathrm{d}V$) is recorded. Two different operation modes are usually applied. The first mode is the so-called constant-height mode (*(I-V)* mode), where the feedback loop is disabled and a constant tip-sample distance is provided during spectroscopy. In this case, the STM tip is placed at the site of interest. At a certain the setpoint current, the feedback is disabled and the bias is varied in the range of interest and the tunneling current is recorded. Information about the density of states is contained in the derivative of the tunneling current with respect to the bias voltage [Eq. (2.8)]. Fig. 2.3 presents two simplified schemes of the tip and sample DOS at both bias polarities. At positive sample bias, shown in Fig. 2.3(a), electrons tunnel from the tip to the sample and probe unoccupied sample states. At negative bias [Fig. 2.3(b)], occupied states of the sample are probed. At bias values, where a resonance of the sample is present, the spectrum shows a larger $\mathrm{d}I/\mathrm{d}V$ signal.

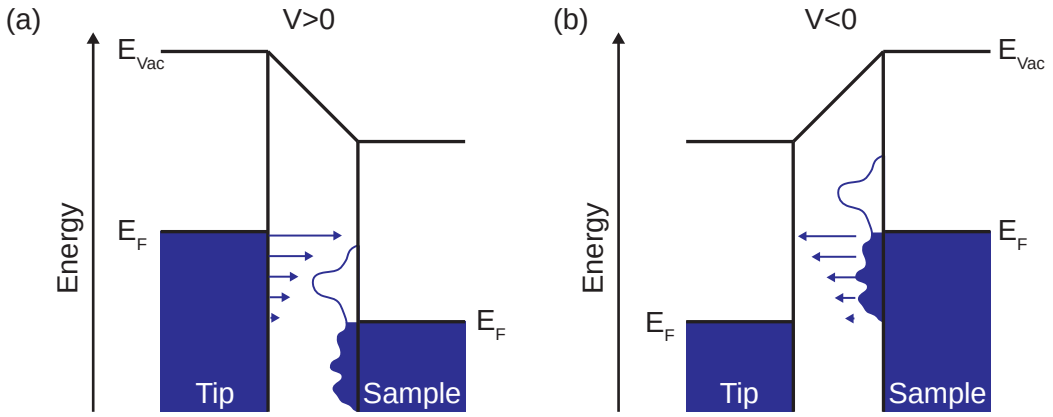

Figure 2.3: (a) DOS schemes for tunneling spectroscopy at positive sample bias. (b) Tunneling spectroscopy at negative sample bias

Another mode of STS is also used in this thesis: it is called constant-current mode, or shortly *(I-z)* mode. There, the $\mathrm{d}I/\mathrm{d}V$ spectrum is recorded while the feedback is still enabled. Upon changing the bias voltage, the tip-sample distance is adjusted in order to keep a constant tunneling current. This mode is especially well suited for spectroscopy at relatively large bias voltages, since it prevents a destruction of the probed adsorbates at high electric field strengths. The drawback of this mode is that molecular orbitals appear at energies shifted with respect to their original energies, which is an effect of changing tunnel matrix elements.

In measurements, the setup is subject to external noise, such as mechanical noise as well as electrical noise. This will influence the measurements and decrease the signal-to-noise ratio in spectroscopy. To obtain a good signal of the differential conductance, a lock-in amplifier is used, whose function is explained in the next section.

2.2.2 The Use of a Lock-in Amplifier

A lock-in amplifier is used in scanning tunneling spectroscopy to increase the signal-to-noise ratio and directly obtain the differential conductance. In general, a lock-in amplifier adds an AC voltage of the form $V(t) = V_\mathrm{m} \sin(\omega_\mathrm{m} t + \phi_\mathrm{m})$ to the DC bias voltage, where ϕ_m is the phase of the modulation. The frequency ω_m of this voltage modulation must be high compared to the time constant used for recording the spectrum. If it is comparatively low, the average bias voltage at one point of the spectrum does not correspond to the DC bias but is altered by the modulation. With the high-frequency bias modulation, the tunneling current acquires a time dependence and is given as:

$$I_\mathrm{t} \propto \int_0^{eV + eV_\mathrm{m} \sin(\omega_\mathrm{m} t + \phi_\mathrm{m})} dE \rho_\mathrm{s}(E). \tag{2.9}$$

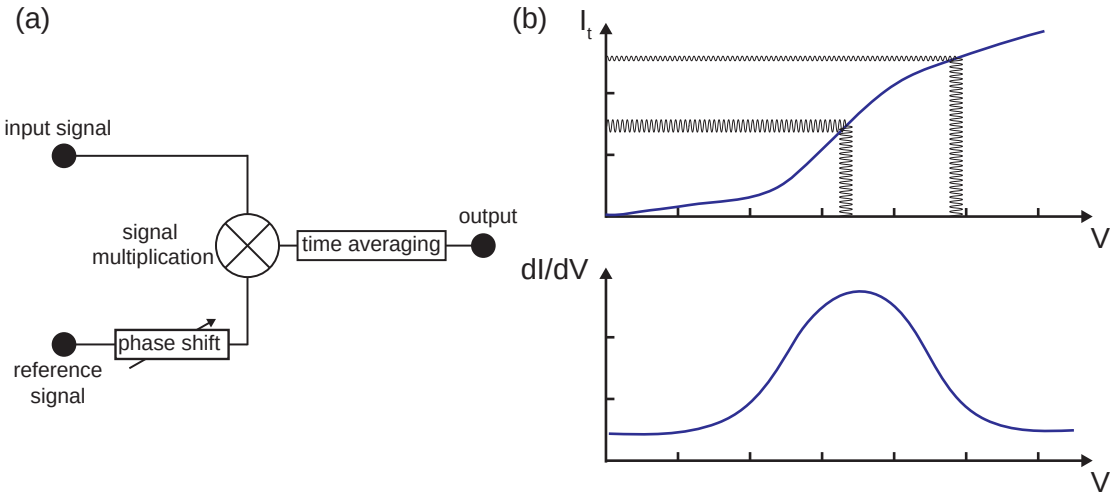

Figure 2.4: (a) Scheme of a lock-in amplifier. The input signal from the tunnel junction is multiplied with a reference signal from the lock-in amplifier, whose phase can be adjusted. After the signal multiplication, a low-pass filter cuts the high frequency component and the remaining output is proportional to the density of states. (b) I-V curve in a tunnel spectrum with the effect of a modulation voltage illustrated. (top) The larger the slope of the I-V curve, the stronger is the variation of the tunneling current, induced by the modulation voltage. This is detected via the lock-in amplifier which yields the density of states (bottom).

For small modulation voltages, a Taylor expansion can be performed, which yields

$$I_\mathrm{t} \propto \underbrace{\int_0^{eV} dE\rho_\mathrm{s}(E)}_{\text{tunnel current}} + \underbrace{\rho_\mathrm{s}(eV)eV_\mathrm{m}\sin(\omega_\mathrm{m}t+\phi_\mathrm{m})}_{1^{st}\text{ harmonic}} + \underbrace{\frac{\mathrm{d}\rho_\mathrm{s}(eV)}{\mathrm{d}V'}\frac{(eV_\mathrm{m})^2}{2}\sin^2(\omega_\mathrm{m}t+\phi_\mathrm{m})}_{2^{nd}\text{ harmonic}} + \mathcal{O}(V_\mathrm{m}^3). \tag{2.10}$$

The first term in this equation is proportional to the tunneling current and often called the zero-order component. Similarly, the second term is called the first harmonic and is proportional to the sample DOS, but still time dependent. For some purposes the second harmonic is relevant because of its proportionality to the second derivative of the tunneling current. For example, a step in the first derivative of the current will be a peak in the second derivative. This is especially useful to detect molecular vibrations and spin-flip excitations, which are visible as steps in the first derivative, but can be observed much easier as peaks in the second derivative.

The tunneling current from the junction is transformed into a voltage signal. Now, the lock-in amplifier is used to extract the time-independent signal. An additional reference signal (see Fig. 2.4(a)) of the form $V_\mathrm{ref}(t) = V_\mathrm{ref}\sin(\omega_\mathrm{ref}t+\phi_\mathrm{ref})$ is multiplied to the input signal and afterwards time-averaged by a low-pass filter. With regard to the multiplication, we focus on the first harmonic in Eq. (2.10), which will be the quantity of interest. Substituting $V_\mathrm{signal} = \rho_\mathrm{s}(eV)eV_\mathrm{m}$ does not change the underlying physics and simple trigonometric relations lead to [62]

$$\begin{aligned} V_{\text{mult}} &= V_{\text{signal}} \sin(\omega_{\text{m}} t + \phi_{\text{m}}) * V_{\text{ref}} \sin(\omega_{\text{ref}} t + \phi_{\text{ref}}) \\ &= \tfrac{1}{2} V_{\text{signal}} V_{\text{ref}} \cos[(\omega_{\text{ref}} - \omega_{\text{m}})t + \phi_{\text{m}} - \phi_{\text{ref}}] \\ &\quad -\tfrac{1}{2} V_{\text{signal}} V_{\text{ref}} \cos[(\omega_{\text{ref}} + \omega_{\text{m}})t + \phi_{\text{m}} + \phi_{\text{ref}}]. \end{aligned} \tag{2.11}$$

Both terms in the obtained equation depend on the frequencies and the phases of the input and reference signals. The way to obtain the first derivative is in choosing equal frequencies for the reference signal and the input signal, which removes the time dependence of the first term. As a result, the first derivative will not be cut off by the low pass filter, whereas the time-dependent part of the signal is filtered. After the low-pass filter, the signal is thus

$$V_{\text{output}} = \frac{1}{2} V_{\text{signal}} V_{\text{ref}} \cos(\phi_{\text{m}} - \phi_{\text{ref}}). \tag{2.12}$$

The reference signal as well as the phases are constant throughout the measurement, so the only variable is V_{signal}, which is proportional to the sample DOS, as substituted earlier. To further increase the output signal, the phase of the reference signal is adjusted to coincide with the input reference, $\phi_{\text{m}} = \phi_{\text{ref}}$. This method is called phase-sensitive detection (PSD) and is commonly used to enhance the signal output of a lock-in amplifier.

Fig. 2.4(b) illustrates the effect of the bias voltage modulation on the lock-in signal. When an AC component is added to the DC bias voltage (vertical wiggly lines in the current signal in top part), the tunneling current also oscillates. The magnitude of the tunneling current oscillation depends on the slope of the current itself. A lock-in amplifier visualizes this modulation, thus giving information about the slope of the current, hence the density of states. In this example, a peak is shown in the conductance signal obtained by the lock-in signal (lower graph) at the bias voltage where the current increase is steepest.

Other harmonics can also be accessed using the lock-in amplifier. To retrieve the original tunneling current signal, the reference signal has to be time independent. Then, higher orders in the Taylor expansion keep their time dependence and will be cut off by the low-pass filter. Only the zero-order component remains, which is proportional to the tunneling current. With a reference signal with twice the frequency of the input modulation, the second derivative of the current can be visualized, as commonly used to investigate molecular vibrations.

2.2.3 Spectral Broadening by the Lock-in Amplifier

In order to make sure that the added modulation of the bias does not corrupt the energy resolution, one needs to choose the amplitude of the AC voltage such that its influence is small compared to the width of the features. To this end, it is instructive to know how the modulation broadens spectral features. The origin of the broadening is the averaging process when the multiplied signal of the input and the reference pass the low pass filter. Mathematically, the averaging process corresponds to an integration over an oscillation period and subsequent division by its time span. This leads to time-independent current of [63]

$$I_{\mathrm{lock-in}}(V) \propto \frac{2}{\tau}\int_{-\tau/4}^{\tau/4} I(V + eV_\omega \sin(\omega t))V_{\mathrm{ref}} \sin(\omega t)\mathrm{d}t \tag{2.13}$$

for the multiplied input and reference signal (Eq. (2.10)). V_ω and V_{ref} are the time-independent modulation amplitudes of the input and reference signal, respectively. Substituting $E = eV_\omega \sin \omega t$, and choosing $\tau = 2\pi/\omega$, it transforms into

$$I_{\mathrm{lock-in}}(V) \propto \frac{V_{\mathrm{ref}}}{\pi V_\omega}\int_{-eV_\omega}^{eV_\omega} I(V+E)\frac{E}{\sqrt{(eV_\omega)^2 - E^2}}\mathrm{d}E. \tag{2.14}$$

Partial integration now gives as expression for the lock-in signal

$$I_{\mathrm{lock-in}}(V) \propto \frac{V_{\mathrm{ref}}}{\pi V_\omega}\int_{-eV_\omega}^{eV_\omega} \frac{\mathrm{d}I}{\mathrm{d}V}(V+E)\sqrt{(eV_\omega)^2 - E^2}\mathrm{d}E, \tag{2.15}$$

which is proportional to the density of states. From Eq. (2.11), we know that the phase-adjusted lock-in signal is

$$I_{\mathrm{lock-in}}(V) = V_{\mathrm{output}}(V) = \frac{V_{\mathrm{ref}}}{2}\left[\frac{\mathrm{d}I}{\mathrm{d}V}(V)\right]_{\mathrm{measured}}, \tag{2.16}$$

so we end up with the lock-in signal as

$$\left[\frac{\mathrm{d}I}{\mathrm{d}V}(V)\right]_{\mathrm{measured}} \propto \int_{-eV_\omega}^{eV_\omega} \frac{\mathrm{d}I}{\mathrm{d}V}(V+E)R(E)\mathrm{d}E, \tag{2.17}$$

which is a convolution of the real density of states obtained in Eq. (2.10) and a broadening function $R(E) = 2/(\pi V_\omega)\sqrt{(eV_\omega)^2 - E^2}$ due to the modulation of the lock-in amplifier. The shape of the broadening is a semicircle with a full width at half maximum (FWHM) of $1.7V_\omega$.

For practical purposes, if the modulation voltage is small compared to the natural line width of the investigated features, the broadening due to modulation can be neglected. This is the case when the FWHM of the feature is larger than $\sqrt{3}V_\omega$. In this thesis, we will denote the lock-in modulation as V_{rms}, which is the root-mean-square of the modulation amplitude.

2.2.4 Spectral Broadening at Finite Temperature

Spectral features in scanning tunneling spectroscopy will also be broadened by temperature effects. In general, the approximation of the Fermi-Dirac distributions as step functions in Eq. (2.5) holds only true for zero temperature. In order to get an expression for the density of states at finite temperatures, we take a simplification of Eq. (2.5),

$$I_{\mathrm{t}} \propto \int_{-\infty}^{+\infty} dE\rho_{\mathrm{s}}(E)f(E+eV)\left[1 - f(E)\right], \tag{2.18}$$

where the tunnel matrix element as well as the tip DOS have been omitted as they are constant. The $\mathrm{d}I/\mathrm{d}V$ signal follows as the derivative of the tunneling current

$$\frac{\mathrm{d}I}{\mathrm{d}V}(V) \propto \int_{-\infty}^{+\infty} dE \rho_{\mathrm{s}}(E) \frac{\mathrm{d}}{\mathrm{d}V} f(E+eV). \tag{2.19}$$

This relation delivers the final result for the $\mathrm{d}I/\mathrm{d}V$ signal at finite temperature. It is a convolution of the DOS at zero temperature with the derivative of a Fermi-Dirac distribution [64]. It is instructive to say that the derivative of the Fermi-Dirac distribution is a peak function of the mathematical form

$$\frac{\mathrm{d}}{\mathrm{d}V} f(E+eV) = \frac{e \exp\left((E+eV)/k_{\mathrm{B}}T\right)}{k_{\mathrm{B}}T(\exp\left((E+eV)/k_{\mathrm{B}}T\right)+1)^2} \quad , \tag{2.20}$$

with e being the electron charge. For measurements at higher temperature, a convolution of the thermal broadening function and the zero-temperature DOS will be fitted to account for thermal effects. At a temperature of 1 K, the width of a Fermi-Dirac distribution is already $3.5k_{\mathrm{B}}T$=0.3 meV which will lead to a broadening of spectral features.

2.2.5 Inelastic Electron Tunneling Spectroscopy

Up to now, only elastic tunneling processes were regarded, where the initial and final state are at the same energy. In this case, the resulting conductance signal was found to be proportional to the density of states of the sample, as illustrated in Fig. 2.5(a).

Besides elastic tunneling processes, electrons can exchange energy with the system, thereby inelastically tunneling across the junction. A necessary condition for it is the existence of accessible higher lying states of the system. Molecular vibrations [55, 65] and spin flip excitations [56] are the most common examples accessed by inelastic electron tunneling spectroscopy (IETS). A sketch describing inelastic tunneling is shown in Fig. 2.5(b). Here, the different energy levels of the system are represented by the orange lines. At positive bias, electrons tunnel from the tip into the system. A fraction of the tunneling electrons loses an energy E_{IETS} (green wiggled line) to the system, which is excited to a higher level. Note that elastic tunneling is still possible and not all electrons donate energy to the system. Inelastic processes only take place at bias voltages higher than the threshold energy of the excitation. The opening of the additional inelastic channel leads to an increase of the current slope (see I-V trace in Fig. 2.5(b)), which leads to steps in the $\mathrm{d}I/\mathrm{d}V$ spectrum. Because inelastic processes take place for both tunneling directions, these steps are symmetric around E_{F}. Quantitatively, inelastic tunneling is accounted for by an additional term for these processes in Eq. (2.4).

The step energy depends on the excitation energies of the probed system. It thus reveals information about the excitation energies of vibrational modes or spin projections at higher energy, which can be inelastically excited. Additionally, the step intensity depends on the coupling of the tunneling electrons to these degrees of freedom of the system. For vibrational modes, the intensity depends on the electron-phonon coupling, which is small. An increase in conductance for vibrational excitations usually in the range of a few % [66]. The width of the steps depends on the system temperature and the lifetime of the excited levels. Short-lived vibrations lead to

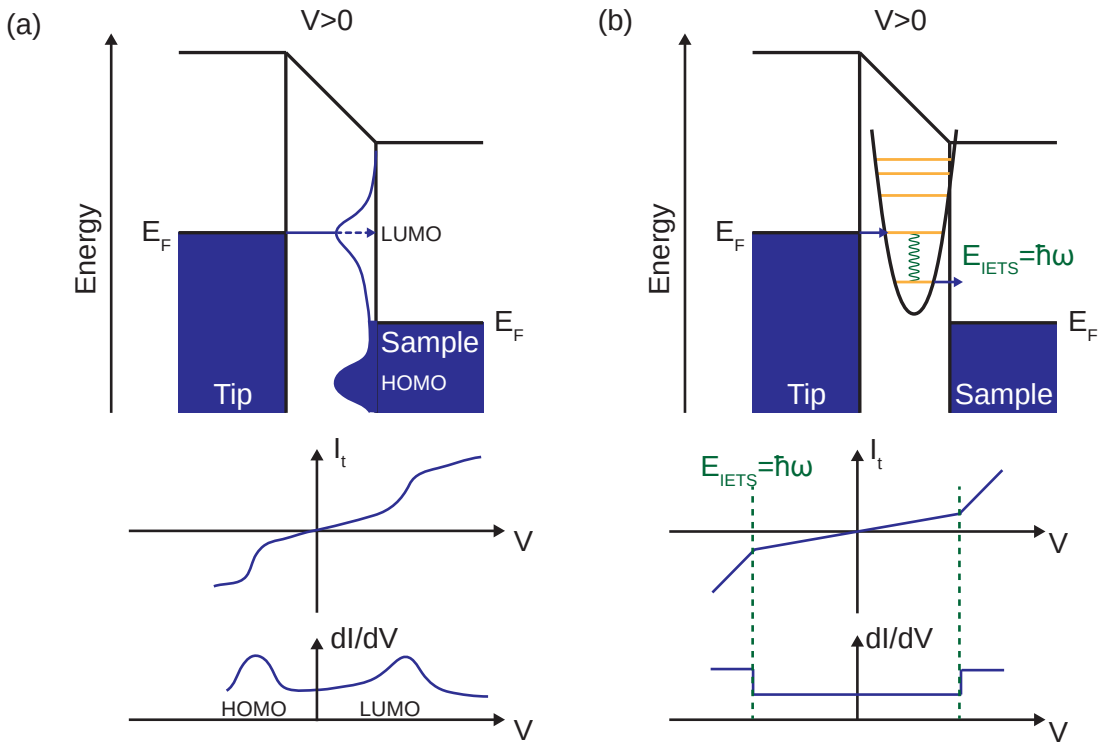

Figure 2.5: Comparison of elastic an inelastic tunneling processes. (a) Scheme of an elastic tunneling process. At positive sample bias, electrons tunnel into the LUMO state of the molecule-substrate system. A non-linear increase in the current is found and the dI/dV-trace (lower part) resembles this density of states. (b) Inelastic tunneling process, where a tunnel electron from the tip (left) donates energy to excite the system to another state (green wiggled line) and tunnels into unoccupied sample states. Consequently, a kink in the current and steps in the differential conductance signal indicate the inelastic process, where the step energy corresponds to the excitation energy of the system.

broad steps with a low intensity, which are difficult to observe. For such systems it is favorable to record the second derivative of the current (d^2I/dV^2), as described in section 2.2.2, where steps in the dI/dV signal become peaks or dips and are easier to detect.

Spin-flip excitations can arise for a paramagnetic atom or molecule in a magnetic field, where different spin projections are split due to the Zeeman effect [56]. For systems with spin states S$\geq$1 and a broken spherical symmetry, magnetic anisotropy can cause a splitting of different spin projection states. Excitations from the ground state to excited levels can be probed by IETS. A strong electron-spin coupling strength produces steps with an intensity increase of up to 100 %. The magnetic origin of such spin excitations can be verified by a shift of the step energies in a magnetic field.

2.3 Experimental Setup

The experiments presented in this thesis were performed using two different low-temperature scanning tunneling microscope setups. The basic components of both systems are similar. For the study of the switching behavior of diarylethenes on Ag(111), presented in chapter 4, a custom-built low temperature STM with a working temperature of 4.5 K was used. This STM has a scanning head with a design proposed by Besocke [67]. Paramagnetic molecules on the superconductor Pb were studied in a Specs Joule-Thomson (JT) STM. A technical scheme of the setup of the JT-STM is shown in Fig. 2.6(a). Like the custom built STM, it consists of two compartments, that can be separated from each other by a gate valve. On the left is the preparation chamber and on the right the STM chamber. In the preparation chamber, the samples are prepared for measurements by sputtering and annealing the surface and deposition of molecules. It is equipped with a mass spectrometer, an ion gun to sputter the surfaces and several ports where molecule or atom evaporators can be attached. To transfer the samples between the preparation chamber and the STM chamber, a manipulator is attached to the preparation chamber. It has an integrated resistive heater below the sample and thermocouples as well as diodes to measure the temperature. Additionally, a capillary for liquid-helium cooling is integrated and can be used to cool the samples. Vacuum pumps such as turbo pumps and ion getter pumps are connected to the preparation chamber as well as the STM chamber to reduce the pressure to 10×10^{-10} mbar inside the vacuum chambers. At such low pressures, a contamination of the samples by ambient gases is drastically reduced.

The STM chamber, in the right of Fig. 2.6(a), hosts the STM scanning head. A bath cryostat consisting of a liquid helium and a liquid nitrogen reservoir ensures low temperatures for the experiments. A scheme of the cryostat is shown in Fig. 2.6(b). The STM stage is thermally connected to a liquid helium vessel. Additionally, thermal shields connected to the helium vessel screen external thermal radiation. The helium cryostat is surrounded by a liquid nitrogen cryostat and shields, to minimize the consumption of liquid helium.

2.3.1 The Joule-Thomson Effect

In contrast to the custom-built STM, the Specs JT-STM is especially designed to reach temperatures of 1 K by making use of the Joule-Thomson effect. For that purpose, a Joule-Thomson cooler is integrated into the system, as shown in Fig. 2.6(b). A simplified schematics of the Joule-Thomson stage is shown in Fig. 2.6(c). It consists of an additional He cycle, which is suited for the use of He^4 or He^3. A bottle outside the cryostat contains helium at room temperature under high pressure. A system of capillaries runs through the system and ends in a pump on the other side, outside the system. The gradient in pressure produced by the pump leads to the gas flow through the JT system. First, the helium passes a cold trap outside the cryostat, which is filled with liquid nitrogen. In there, the gas is already pre-cooled and contaminations of the gas freeze out and do not enter the smaller capillary inside the cryostat, which could easily be clogged by contaminations. Inside the cryostat, the gas flows through a back streaming heat exchanger. Thermal contact to the cold exhaust gas from the JT stage cools the gas further in the heat exchanger.

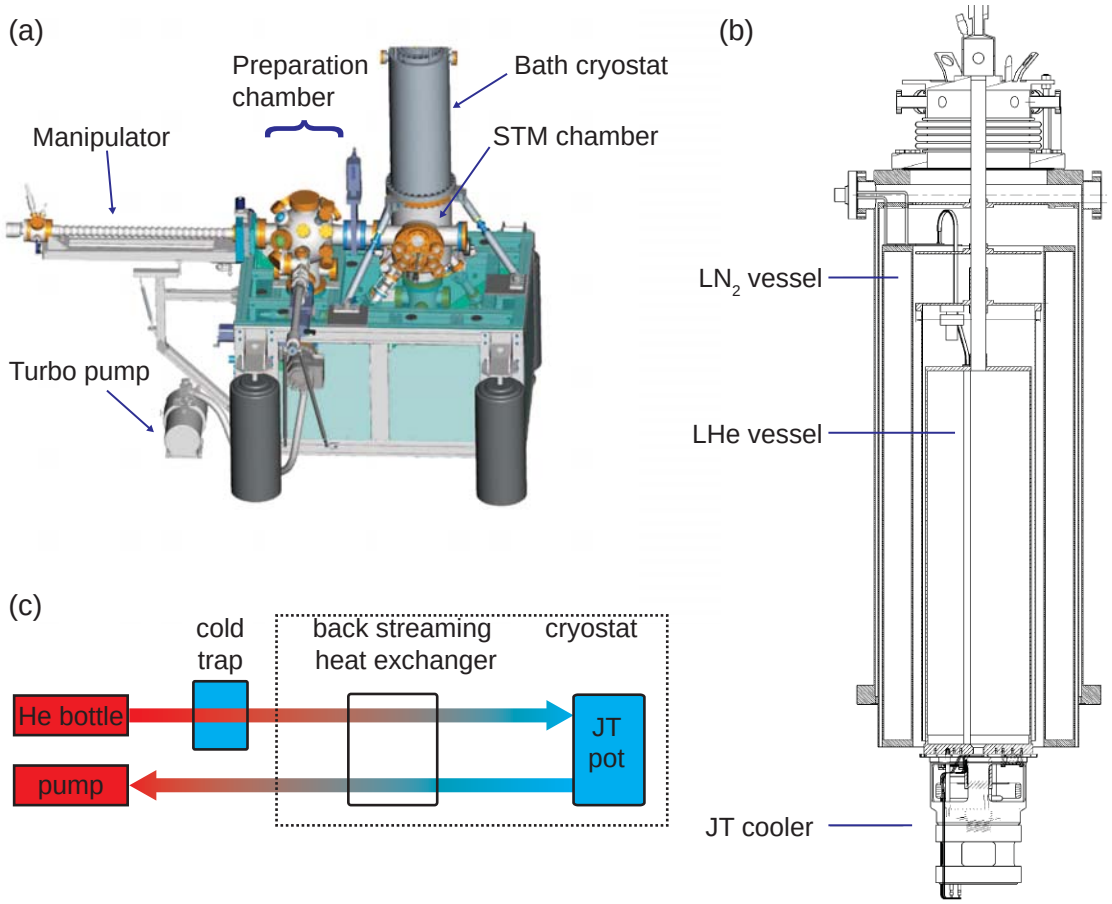

Figure 2.6: (a) Drawing of the vacuum chamber hosting the STM as well as a preparation chamber. Components are indicated in the sketch. (b) Design of the SPECS JT-STM bath cryostat with an inner vessel containing liquid helium surrounded by a vessel with liquid nitrogen. Special to this design is the JT cooler, reaching temperatures of 1.1 K. (c) Simplified scheme of the JT cycle. Red indicates high temperatures, whereas blue indicates low temperatures.

Upon entering the JT pot on the right of the schematics in Fig. 2.6(c), the cold gas expands adiabatically. As no energy is exchanged with an outer reservoir, the enthalpy H is conserved during this throttling process. However the pressure p and the volume V of the gas change. The enthalpy depends on these parameters in the way

$$H = \mathrm{U} + pV, \tag{2.21}$$

where U is the internal energy of the system. An ideal gas does not exhibit the Joule-Thomson effect, because there are no interactions between the gas molecules. For a real gas, pV describes

the work done on the system or gained from the system to bring the gas particles closer together or further apart, respectively. Therefore, pV is not zero. The sign of pV depends on the parameters of the system, such as the heat capacity C_p and the temperature T of the gas itself. The system can be characterized by the so-called Joule-Thomson coefficient, which is related to parameters of the system and describes the relative temperature change due to a pressure change:

$$\mu_\mathrm{JT} = \frac{\partial T}{\partial p} = \frac{V}{C_\mathrm{p}}(\alpha T - 1). \tag{2.22}$$

The parameter α thus indicates when a Joule-Thomson expansion leads to a cooling of the system. This is the case when $\alpha > 1/T$.

With this Joule-Thomson effect, the system can be cooled to 1.1 K when using He^4 and below 1 K when using He^3.

2.3.2 The Split-Coil Magnet

To measure the response of paramagnetic molecules on surfaces to an external magnetic field, a superconducting split-coil magnet is incorporated in the Specs JT-STM. Superconducting coils have a strong advantage compared to normal conducting coils, as they support large currents without resistance. The arrangement of the coils is according to the setup of a pair of Helmholtz coils, which consists of two coils separated by a distance d equal to their radius. In the center between the coils at which the sample is placed, an approximately homogeneous magnetic field is produced. The magnetic field can be calculated using the Biot-Savart law. At the central point between the two coils, it is given as

$$B(R/2) = \left(\frac{8}{5\sqrt{5}}\right)\frac{\mu_0 n I}{R} \tag{2.23}$$

with the vacuum permeability μ_0, n the number of windings of the coils and R the radius of the coils. These parameters are fixed, so the magnetic field is proportional to the current I,

$$B = cI. \tag{2.24}$$

For the given setup in the JT-STM, the current field conversion rate is c=0.1548 T/A, such that a current of I=19.4 A produces a field of maximally 3 T.

2.4 Used Surfaces and Sample Preparation

The studies in this thesis were performed on two different single crystal substrates. Molecular switching was investigated on the noble metal substrate Ag(111). It is a face-centered cubic crystal lattice with a lattice constant of 4.1 Å. The (111) surface shows a hexagonal symmetry, where the spacing between surface atoms is 2.89 Å. In the electronic structure, Ag(111) exhibits a surface state at an energy of −67 mV [68].

As superconducting substrate, we chose the (111) surface of Pb. As silver, Pb has a face-centered cubic lattice. Here the lattice constant is a =4.95 Å. On the (111) surface, the atom

spacing is 3.50 Å. Pb becomes superconducting below a critical temperature of 7.2 K. It is a type-I superconductor, which means that there is only one critical magnetic field, at which superconductivity is destroyed completely.

In order to obtain atomically flat surfaces without contaminations, the substrates were cleaned by repeated cycles of sputtering by Ne^+ ions and subsequent annealing. The Ag crystal was annealed up to temperatures of 800 K. Pb has a low melting point and was therefore annealed at a temperature of 430 K. Molecules were evaporated from a Knudsen cell. The evaporation temperatures of the molecules are given in chapters.

In the next chapter, we will introduce the basic concepts of magnetism of atoms and molecules as well as their interaction with surfaces. Interactions of magnetic molecules with superconductors is studied in chapter 5 and 6. Therefore, we will also give a short introduction to the theory of superconductivity and the effects, magnetic impurities have on them.

Chapter 3

Magnetism at the Nanoscale and Superconductivity

A focus of this thesis addresses the study of the interaction of paramagnetic metal-organic molecules with superconductors. In this section, we will introduce the principles of magnetism in single atoms and molecules as well as possible fingerprints of their interaction with the underlying substrate. Additionally, we will give a brief introduction into the theory of superconductivity. At the end of this chapter, the effects of magnetic impurities in superconductors are introduced.

3.1 Magnetism of Atoms and Molecules

Magnetism in atoms and molecules is a result of unpaired electrons. In an atom with n unpaired electrons, the total spin adds up to $S = n/2$ as the unpaired spins align parallel due to exchange interactions, commonly known as 1^{st} Hund rule. If this spin is in an isotropic environment, there is no preferred spin orientation in space. However, when the atom is placed in an anisotropic environment, *e.g.*, on a surface or surrounded by an organic ligand, certain orientations of the spin become energetically favored.

3.1.1 Crystal Field Theory

We illustrate the influence of the immediate environment on an atomic spin with the example of the 3d orbitals. Many 3d transition metal elements with partly filled 3d orbitals are paramagnetic. The five 3d orbitals are shown in Fig. 3.1(a), which are already linear combinations of the original orbitals with different angular momentum quantum numbers l. In the isotropic case, all five levels are degenerate (see Fig. 3.1(b)) and will be occupied by electrons according to Hund's rules, such that the spin is maximized.

A crystal field or a ligand around the atom can be modeled by atoms placed around the atom, as shown in Fig. 3.1(c). Here, the crystal field has an octahedral symmetry with six atoms placed along the Cartesian axes. Due to the Coulomb interaction of the electrons in the central atom with the electrons of the ligand atoms, the 3d levels split in energy. The two orbitals that point

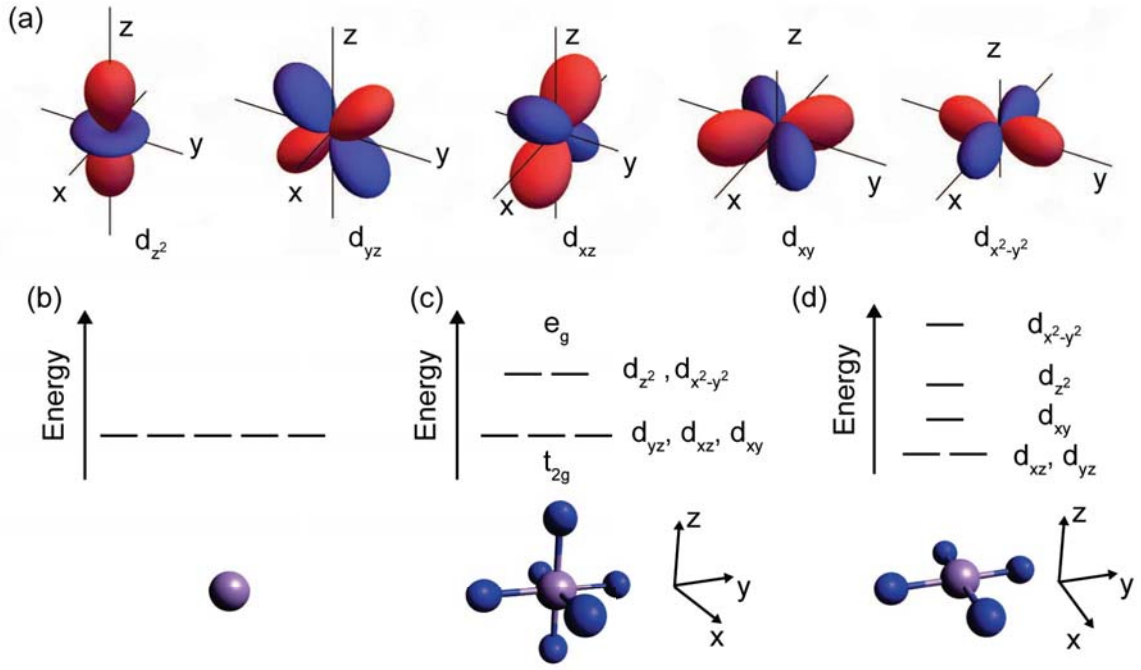

Figure 3.1: (a) Spatial distribution of the five 3d orbitals. Electrons are localized in the blue and red areas. (b) Level arrangement of the 3d orbitals in an isotropic environment. (c) Level splitting in an octahedral ligand field, where six atoms surround the central atom. Two subsets form, labeled e_g and t_{2g}. (d) Level splitting for an atom subject to a square-planar ligand field. The purple atom represents the central atom, surrounded by four atoms, representing the ligand.

directly towards the ligand atoms, $d_{x^2-y^2}$ and d_{z^2}, will be lifted in energy, as they experience the strongest Coulomb repulsion. The ones that extend in between the ligand atoms are lowered in energy. Two subsets are formed, which are called the t_{2g} subset and the e_g subset. This effect is called crystal field splitting and can lead to a different occupation of the levels by electrons, depending on the magnitude of the splitting. As a result, the total spin state of the magnetic atom can be changed.

A reduction of the crystal field symmetry causes further splitting of the 3*d* levels. In Fig. 3.1(d), a square planar ligand field is shown, which is obtained by removing the two ligand atoms along the z-axis. In this case, the d_{z^2} is lowered in energy with respect to the $d_{x^2-y^2}$ and the d_{xz} and d_{yz} levels can also be lowered in energy.

3.1.2 Magnetic Anisotropy and the Spin Hamiltonian Approach

The orbitals shown in Fig. 3.1(a) are linear combinations of the original 3*d* orbitals, such that the orbital angular moment of each of these orbitals is zero. Therefore, when the ground state of an atom in a crystal field is non-degenerate, the total orbital angular moment is usually quenched.

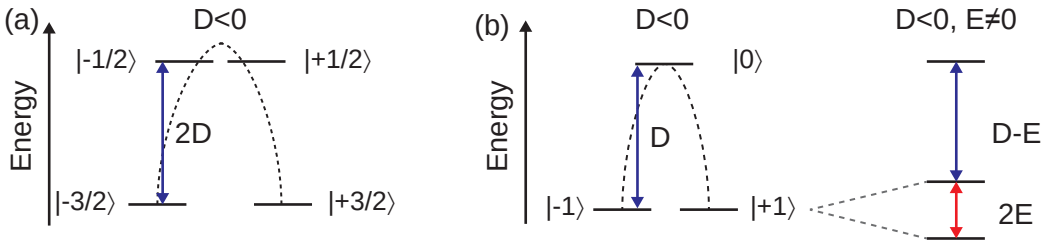

Figure 3.2: (a) Level energy alignment of a system with total spin $S = 3/2$ with easy-axis uniaxial anisotropy. (b) Level alignment of a system with $S = 1$ with easy axis anisotropy (left part). When transverse anisotropy is also present, the $|\pm 1\rangle$ levels also split (right part).

However, an admixture of different atomic orbitals that are split by the crystal field restores the orbital angular moment, as consequence of a second order perturbation. Spin-orbit coupling then leads to a preferred direction of the spin, known as magnetic anisotropy. A simple model to describe magnetic anisotropy is the so-called spin-Hamiltonian approach, which essentially treats the system in terms of the spin components. In the lowest approximation, the spin Hamiltonian is given as [69]:

$$\hat{H} = \mathrm{D}S_{\mathrm{z}}^2 + E\left(S_{\mathrm{x}}^2 - S_{\mathrm{y}}^2\right) - g\mu_{\mathrm{B}}\boldsymbol{B}\cdot\hat{\boldsymbol{S}}. \tag{3.1}$$

The last term describes the splitting of the spin levels in an external magnetic field $\boldsymbol{B}$ due to the Zeeman effect. Here, g is the gyromagnetic factor, μ_{B} the Bohr magneton and $\hat{\boldsymbol{S}}$ the spin operator. In the absence of a magnetic field, the system can be split by magnetic anisotropy, described by the first and second term in Eq. (3.1). This effect is often referred to as zero-field splitting (ZFS). The first term describes longitudinal magnetic anisotropy D, which leads to a splitting into $2S+1$ levels. Those correspond to the spin projections along the z-axis, which are eigenvalues of the spin operator along the z-direction S_{z}. The second term accounts for an anisotropy in the x-y plane and is called transversal anisotropy, with E being the transversal anisotropy parameter. It leads to a mixing of states with different z-projections. Usually, it is preferable to describe the system in a new basis different from the Cartesian coordinates. The new basis is chosen such that |D| is maximized and E is positive.

An example for a spin-3/2 system in the presence of longitudinal anisotropy (E=0) is shown in Fig. 3.2(a). In the example, D<0, and the states $|\pm 3/2\rangle$ form the ground state, whereas the states $|\pm 1/2\rangle$ are at an energy 2D higher than the ground state. This case is called easy-axis anisotropy because it favors higher spin projections. The opposite case, that is when D>0, is called easy-plane or hard-axis anisotropy and states with low spin projections are favored. Transverse anisotropy E causes a shift of the energy of these levels. However, the levels remain doubly degenerate with $|\pm m_{\mathrm{S}}\rangle$ due to the Kramer's degeneracy theorem.

An example for uniaxial anisotropy in an integer spin system is shown in Fig. 3.2(b). For D< 0, $|\pm 1\rangle$ forms the ground state and the excited state $|0\rangle$ is separated by an energy D. Here, transverse anisotropy leads to a splitting into three levels, where the initially degenerate states $|\pm 1\rangle$ start to mix and the system is described by new eigenvectors.

The magnetic anisotropy can be measured experimentally by IETS, where excitations from the ground state to excited states are seen as steps in the differential conductance. The number and energy of the spin excitations as well as their shift in a magnetic field are used to determine the spin state of a given system.

3.2 The Kondo Effect

The first evidence of what today is known as the Kondo effect appeared in 1936 as a resistance minimum at finite temperature in metals, which contain paramagnetic impurities [70]. In pure metals, a decrease in temperature leads to a lowering of the resistance, which levels off to a finite residual resistance depending on the element and its purity. However, if paramagnetic impurities are present in the metal, the resistance reaches a minimum at finite temperature T_{K} and starts to increase again upon further lowering the temperature. This phenomenon could only be explained nearly thirty years later by Jun Kondo. He treated the problem as a magnetic scattering process of the conduction electrons at the paramagnetic impurity, including the interaction of the spins of the substrate electrons and the impurity electron [38]. After the effect had been explained, research interest faded in subsequent years. With the detection of the Kondo effect in single adatoms on surfaces [71, 72] and in quantum dots [73, 74], the interest in this exciting quantum many body effect reemerged [75, 76]. Nowadays, research aims at understanding the Kondo effect and its role on the properties of single atoms and molecules on surfaces [77–81].

The Kondo effect can be explained within the so-called Anderson impurity model, which describes paramagnetic impurities in metals [82]. In the Anderson model, only the highest occupied orbital is considered. The model distinguishes between the orbital being unoccupied, singly or doubly occupied. The essential parameters used to characterize the impurity level are the energy of the singly occupied level, ε, as well as the Coulomb energy U, which has to be paid in order to doubly occupy the orbital. An illustration of the Anderson impurity model with its parameters is shown in Fig. 3.3(a). The Kondo effect arises when the impurity is singly occupied, *i.e.* the level ε is below E_{F} and $\varepsilon + U$ is above E_{F}. Because of a coupling of the impurity levels to the electron bath in the substrate, electrons can hop on and off the impurity site. Depending on the coupling strength, the impurity levels acquire a finite width Γ. If the width of the levels is larger than the Coulomb energy U, the singly occupied level at ε and the doubly occupied level at $\varepsilon + U$ overlap in energy and cross the Fermi level. Then, the impurity is not purely singly occupied but in a mixed-valence regime. In this case no Kondo effect is observed.

If Γ is smaller, the system is in the Kondo regime. Here, different exchange processes are possible, as shown in Fig. 3.3(b)-(d). As the energy of the electron in the singly occupied level is lower than E_{F}, an energy of $E_{\mathrm{F}} - \varepsilon$ is required to hop into the unoccupied states in the substrate. Classically, the electron can not leave the impurity site unless the necessary energy is transferred into the system. However, Heisenberg's uncertainty principle, $\Delta E \Delta t \geq \hbar$, applies in this situation. Here, $\hbar$ is the reduced Planck constant. The electron of the impurity thus can occupy empty states in the substrate for a short amount of time. This process is shown by the red arrow representing the electron, which hops into the continuum of the host metal [Fig. 3.3(b)]. For this short period of time, the impurity is unoccupied and an electron from the substrate can occupy the empty impurity level [Fig. 3.3(c)]. This electron can have either spin up or spin down. Other virtual

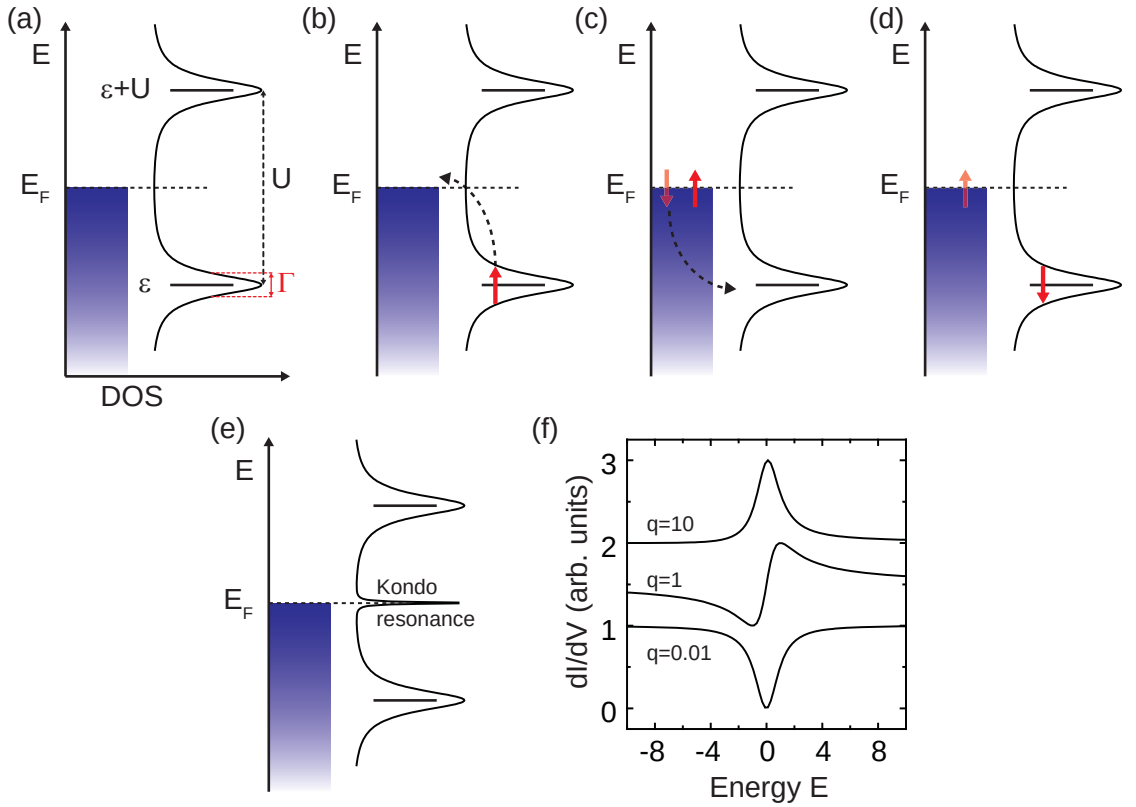

Figure 3.3: (a) The Anderson impurity model with its parameters characterizing the impurity levels. The singly occupied level is at energy ε and the doubly occupied level at $\varepsilon + U$, with U being the Coulomb energy. Due to hybridization with the metal, the levels acquire a finite width Γ. (b)-(d) Spin exchange processes leading to the Kondo effect. The impurity electron can leave the impurity (b) to (c) and the level will be occupied by a second electron from the substrate (c) to (d). Figure adapted from [80]. (e) Density of states with the Kondo resonance at E_{F}. (f) Fano resonance for different parameters q, indicated in the figure.

processes of this kind proceed via the doubly occupied level and a subsequent removal of one electron from the impurity. All these virtual processes create a new many-body ground state in which the spins of the conduction electrons are coupled to the impurity spin. This coupling is usually antiferromagnetic, *i.e.* , spins align antiparallel to each other. In this case, the ground state is a spin singlet. The involved scattering processes lead to a peak in the spectral function around the Fermi level. It can be seen as a zero bias resonance in tunneling spectra, generally known as the Kondo resonance.

Besides antiferromagnetic coupling, spins can also favor a parallel alignment. Then, the Kondo effect is of ferromagnetic nature and the many-body ground state is a triplet [83].

3.2.1 The Kondo Resonance

The Kondo resonance has a Lorentzian lineshape in the DOS, shown in Fig. 3.3(e). It is characterized by the Kondo temperature T_K, which is defined by the width of the resonance at zero temperature:

$$T_K = \frac{\Gamma}{k_B}. \tag{3.2}$$

The Kondo temperature is a measure of the coupling of the impurity to the substrate and can be related to the exchange coupling parameter J and the density of states at the Fermi level ρ_0 [76]

$$k_B T_K = w\sqrt{2J\rho_0}\exp\left(-1/(2J\rho_0)\right), \tag{3.3}$$

with w being the band width of electrons taking part in the screening process. T_K can also be related to the parameters of the Anderson impurity model [84, 85],

$$T_K = \frac{\sqrt{\Gamma U}}{2}\exp\left\{(\pi\varepsilon + U)/\Gamma U\right\}. \tag{3.4}$$

Often, the Coulomb peaks at ε and $\varepsilon + U$ are not detected in experiments. Hence, the nature of the resonance at E_F can not be reliably assigned to the Kondo effect. However, the Kondo resonance has a characteristic temperature dependence, which allows a distinction from molecular or atomic orbitals. The width of the Kondo resonance broadens with the temperature T according to [86]:

$$\Gamma = \sqrt{(\alpha k_B T)^2 + (2k_B T_K)^2}, \tag{3.5}$$

with the factor α=2π in the strong coupling regime. This is valid in case of an experimental temperature much lower than the Kondo temperature ($T \ll T_K$). A large Kondo temperature indicates a more efficient screening of the impurity spin by the conduction electrons. For magnetic impurities on noble metal surfaces, Kondo temperatures of a few K up to 300 K have been observed [29, 71, 72, 86–90]. Bulk impurities, on the other hand, can have even higher Kondo temperatures due to a larger number of nearest neighbors.

In tunneling spectroscopy, the spectral fingerprint of the Kondo effect can be a rather asymmetric lineshape instead of a Lorentzian lineshape. This spectral lineshape is a consequence of interference from different tunneling paths between the sample and the tip. Electron tunneling from the tip to the sample and vice versa can take two different paths: (i) direct tunneling into unoccupied states in the substrate and (ii) tunneling via the Kondo resonance. Interference between the direct tunneling from tip to sample and the path including the Kondo resonance results in a Fano lineshape [91],

$$\rho_{\mathrm{Fano}}(E) \propto \rho_{\mathrm{background}} + \frac{(q+\epsilon)^2}{1+\epsilon^2}. \tag{3.6}$$

The reduced energy ϵ is given as

$$\epsilon = \frac{E - E_K}{\Gamma/2}. \tag{3.7}$$

In Eq. (3.6), $\rho_{\mathrm{background}}$ is a constant background conductance, E_{K} the energy of the Kondo resonance and q a factor which determines the symmetry of the Fano resonance and varies between $0 \leq q \leq \infty$ although negative values of q have been observed [81]. In a physical sense, q is a measure of the interference between electrons in the two tunneling paths, through the Kondo resonance and directly into the sample, respectively. The Fano function is shown in Fig. 3.3(f) for three different values of q. For small q, nearly all tunneling electrons tunnel directly into the substrate continuum, and the resulting Fano lineshape is a dip. For values of q in the order of 1, both paths are equally likely and the lineshape is asymmetric, whereas for large q values, the favored tunneling path is through the Kondo resonance, thus the Fano lineshape resembles a Lorentzian.

In a different approach, Frota solved the Kondo problem using numerical renormalization group theory and found the zero bias peak to be of the form [92, 93]

$$\rho_{\mathrm{Frota}}(E) = \frac{2}{\pi\Gamma_{\mathrm{A}}}\mathrm{Re}\left(\sqrt{\frac{i\Gamma_{\mathrm{K}}}{E+i\Gamma_{\mathrm{K}}}}\right), \tag{3.8}$$

which is referred to as Frota function nowadays. In comparison to a Lorentzian, the Frota lineshape falls off slower towards larger energies.

Interference effects due to different tunneling paths can also be accounted for in the case of a Frota-like zero bias peak. The convolution with a Fano lineshape yields the transmission function, which is measured in STM experiments. This transmission function is given as [94]

$$T_{\mathrm{FF}}(E) = -A \cdot \mathrm{Re}\left[e^{i\phi_{\mathrm{q}}}\sqrt{\frac{i\Gamma_{\mathrm{F}}}{E-E_0+i\Gamma_{\mathrm{F}}}}\right] + T_0. \tag{3.9}$$

A is the amplitude of the resonance and Γ_{F} the Frota parameter, which is related to the half width of the Frota function as $\Gamma = 2.54\Gamma_{\mathrm{F}}$. A constant background conductance is also added here, denoted as T_0. The phase factor ϕ_0 accounts for the interference between the tunneling paths and leads to a dip-like feature for values ϕ_0=0, and to a peak for ϕ_0=π. We will use this Fano-Frota function to fit $\mathrm{d}I/\mathrm{d}V$ spectra that exhibit a Kondo resonance.

3.2.2 The Kondo Effect in a Magnetic Field

Although the Kondo effect involves spin-flip processes and creates a singlet ground state, an external magnetic field still affects the impurity levels. The Zeeman effect splits the levels $|\pm 1/2\rangle$, which are degenerate in the absence of the field. As a consequence, the zero-bias peak starts to split above a critical magnetic field [95, 96]

$$B_{\mathrm{c}} = 0.5 k_{\mathrm{B}} T_{\mathrm{K}}/(g_{\mathrm{S}}\mu_{\mathrm{B}}). \tag{3.10}$$

At magnetic fields large compared to the critical field, the energy splitting of the levels approaches the linear Zeeman splitting [96, 97].

3.2.3 Weak Coupling Kondo Regime

A special case is found in systems where the exchange coupling of the impurity with the substrate electrons is weak. It corresponds to the case when $T > T_K$. In this weak coupling regime, spin exchange processes can be treated as scattering events within a perturbative approach based on a model by Anderson and Appelbaum [98–102]. Processes of second and third order in the exchange interaction J are included. Second order contributions correspond to processes where tunneling electrons interact with the spin of the impurity. In systems with a spin $S > 1/2$ and magnetic anisotropy, these processes lead to inelastic spin excitations. Third order contributions include scattering processes of electrons emerging from and reentering in the sample during the tunneling process of another electron [102]. Steps in the differential conductance, due to second order processes, acquire a peak-like contribution to their shape.

For impurities with a spin 1/2, there is no magnetic anisotropy. In these systems, the weak exchange coupling is manifested by a logarithmic singularity, which is broadened by the temperature [101, 102]. This zero-bias resonance has no internal width, in contrast to the Kondo effect in the strong coupling regime. Additionally, the resonance starts to split at magnetic fields lower than the critical field obtained in Eq. (3.10) for a strongly Kondo screened impurity .

As the electronic states in the sample are only weakly influenced by a localized impurity in the weak coupling regime, no Kondo singlet is formed. In the presence of magnetic anisotropy in a system with $S \geq 1$, spin-flip excitations are taken into account in the model by the spin Hamiltonian, introduced in section 3.1. This leads to a splitting of the peak in the presence of magnetic anisotropy as well as magnetic fields in the order of the thermal energy. An example for a weak coupling Kondo effect will be shown in chapter 6.

3.3 Superconductivity

Superconductivity describes a physical state of matter which is characterized, among other properties, by electron transport with zero resistance. It was first observed by Heike Kammerlingh Onnes in 1911 in his laboratory in Leiden [103–105]. Three years earlier, he had succeeded in the liquefaction of Helium at a boiling point of 4.1 K. The newly established low-temperature record enabled the study of the resistance of metals at temperatures close to absolute zero. Investigating mercury, Kammerlingh Onnes observed an abrupt drop of the electrical resistance at a temperature of 4.15 K. Such a behavior was unexpected.

In a normal metal, the resistance gradually decreases with temperature until a finite resistance is reached, which depends on defects or impurities in the metal [106]. A completely new effect was suspected to cause zero resistivity in metals. After the discovery of superconductivity in mercury, other materials were found to show the same effect. Nevertheless, it took more than 40 years to develop a microscopic theory to explain superconductivity. In this chapter, we introduce the basic principles of conventional superconductivity.

3.3.1 Bardeen-Cooper-Schrieffer Theory of Superconductivity

Electrons in a normal metal are usually described with the model of a free electron gas. The Coulomb repulsion between the electrons is minimized due to screening effects by the ionic lattice.

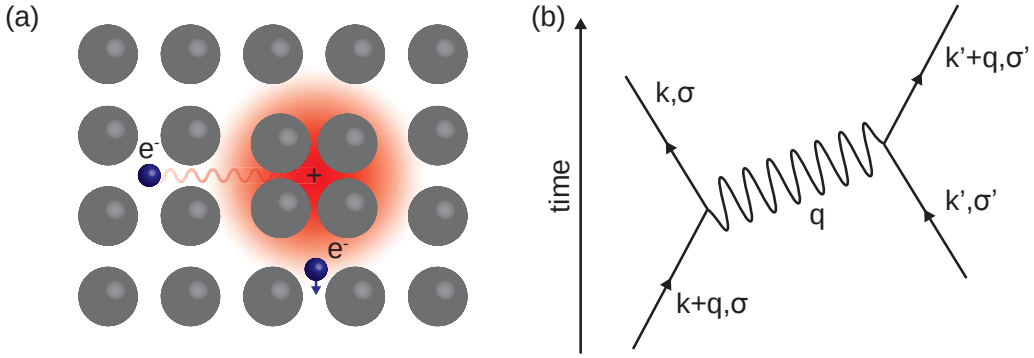

Figure 3.4: (a) Illustration of the phonon creation in a superconductor. Electrons are depicted as blue spheres, whereas the blue arrow shown the momentum. Lattice ions are gray spheres and the excited photon creates a positively charged region, depicted as red circular area. The attractive force to the second electron is shown as red sinusoidal line. (b) Feynman diagram of the Cooper pair formation. The arrows represent the interacting particles and the wiggled line is the phonon, which transmits the attractive interaction.

In a superconductor, bound pairs of electrons are formed. To form such bound pairs, an attractive interaction needs to be present, which is larger than the screened Coulomb repulsion. A purely electronic origin of the attractive interaction is excluded. The discovery of the isotope effect in superconductors suggested the ionic lattice to play a key role in the pair formation. According to the isotope effect, different isotopes of an element lead to different critical temperatures, at which the material becomes superconducting. In fact, it turns out that a phonon-mediated interaction yields the required attractive interaction between electrons. The mechanism is illustrated in Fig. 3.4(a). It can be understood as follows: An electron, depicted as blue sphere (right bottom) travels through the crystal lattice and causes a local attraction of the positive lattice ions, thus excites a phonon. The lifetime of a phonon is related to the Debye frequency as $\tau_\mathrm{i} \sim \omega_\mathrm{D}^{-1}$. The Debye frequency corresponds to the maximum of the excitation energy of phonons in a given lattice. This phonon lifetime exceeds the dwell time of an electron at the Fermi energy, *i.e.* $\tau_\mathrm{e} \sim E_\mathrm{F}^{-1}$. Therefore, the phonon is still excited when the initial electron has left its vicinity. A second electron is attracted by the positively charged area and absorbs the energy of the phonon (blue sphere in the left part). This process creates a small but sufficient attractive interaction and leads to the formation of electron pairs within a small energy range $\pm\omega_\mathrm{D}$ around E_F.

A Feynman diagram in Fig. 3.4(b) illustrates the process of this phonon-mediated electron-electron interaction. Straight arrows represent the electrons. An electron with momentum $\boldsymbol{k}+\boldsymbol{q}$ and spin σ (arrow in lower left part) creates a phonon of momentum $\boldsymbol{q}$, seen as wiggled line. The electron then has a momentum $\boldsymbol{k}$ (upper left arrow). The emitted phonon is absorbed by another electron with momentum $\boldsymbol{k'}$ and spin σ' so its final momentum becomes $\boldsymbol{k'}+\boldsymbol{q}$. The bound electron pairs are called Cooper pairs [107]. Cooper pairs consist of two electrons with opposite spin and momentum, thus are of bosonic nature. To break a Cooper pair, a minimal

energy Δ is required, which corresponds to the superconducting gap parameter.

We will give a short derivation of the Bardeen-Cooper-Schrieffer (BCS) theory of superconductivity and obtain an expression for the gap parameter as well as excitations of the superconductor. A more detailed description can be found in the literature [108, 109].

3.3.2 The BCS Hamiltonian

The BCS Hamiltonian for the system of interacting electrons is given as [110, 111],

$$H_{\mathrm{BCS}} = \sum_{\boldsymbol{k}\sigma} \chi_{\boldsymbol{k}} c^{\dagger}_{\boldsymbol{k}\sigma} c_{\boldsymbol{k}\sigma} + \frac{1}{N} \sum_{\boldsymbol{k},\boldsymbol{k}'} V_{\boldsymbol{k}\boldsymbol{k}'} c^{\dagger}_{\boldsymbol{k}\uparrow} c^{\dagger}_{-\boldsymbol{k}\downarrow} c_{-\boldsymbol{k}'\downarrow} c_{\boldsymbol{k}'\uparrow}. \tag{3.11}$$

The first term describes the electrons in the system, with $c^{\dagger}_{\boldsymbol{k}\sigma}$ and $c_{\boldsymbol{k}\sigma}$ being electron creation and annihilation operators, respectively. $\chi_{\boldsymbol{k}} = \epsilon_{\boldsymbol{k}} - \mu$ is the energy of the electrons $\epsilon_{\boldsymbol{k}}$ with respect to the chemical potential μ, which is equal to E_{F} in equilibrium. The second term accounts for the phonon-mediated interaction between the electrons, as described earlier in this section, and is attractive in a small energy window around E_{F},

$$V_{\boldsymbol{k}\boldsymbol{k}'} = \begin{cases} -V_0, & \text{if } |\chi_{\boldsymbol{k}}| < \hbar\omega_{\mathrm{D}} \text{ and } |\chi_{\boldsymbol{k}'}| < \hbar\omega_{\mathrm{D}} \\ 0, & \text{otherwise.} \end{cases} \tag{3.12}$$

This Hamiltonian can be treated in the mean field approximation, which says that the effect of a large ensemble of particles on an individual particle can be replaced by a mean field accounting for the ensemble. Operators thus are approximated by $A = \langle A \rangle + \delta A$ with the mean value $\langle A \rangle$ and a small fluctuation δA. Applying this approximation to the operators chosen as $A_1 = c^{\dagger}_{\boldsymbol{k}\uparrow} c^{\dagger}_{-\boldsymbol{k}\downarrow}$ and $A_2 = c_{-\boldsymbol{k}'\downarrow} c_{\boldsymbol{k}'\uparrow}$, the Hamiltonian takes the form:

$$\begin{aligned} H_{\mathrm{BCS}} &= \sum_{\boldsymbol{k}\sigma} \chi_{\boldsymbol{k}} c^{\dagger}_{\boldsymbol{k}\sigma} c_{\boldsymbol{k}\sigma} \\ &+ \frac{1}{N} \sum_{\boldsymbol{k},\boldsymbol{k}'} V_{\boldsymbol{k}\boldsymbol{k}'} \Big(\langle c^{\dagger}_{\boldsymbol{k}\uparrow} c^{\dagger}_{-\boldsymbol{k}\downarrow} \rangle c_{-\boldsymbol{k}'\downarrow} c_{\boldsymbol{k}'\uparrow} + c^{\dagger}_{\boldsymbol{k}\uparrow} c^{\dagger}_{-\boldsymbol{k}\downarrow} \langle c_{-\boldsymbol{k}'\downarrow} c_{\boldsymbol{k}'\uparrow} \rangle - \langle c^{\dagger}_{\boldsymbol{k}\uparrow} c^{\dagger}_{-\boldsymbol{k}\downarrow} \rangle \langle c_{-\boldsymbol{k}'\downarrow} c_{\boldsymbol{k}'\uparrow} \rangle \Big). \end{aligned} \tag{3.13}$$

The last term only depends on the mean value of the operators, which is constant. We substitute it with E_{BCS}. By introducing a so-called gap parameter in the way

$$\Delta_{\boldsymbol{k}} = -\frac{1}{N} \sum_{\boldsymbol{k}'} V_{\boldsymbol{k}\boldsymbol{k}'} \langle c^{\dagger}_{\boldsymbol{k}\uparrow} c^{\dagger}_{-\boldsymbol{k}\downarrow} \rangle \tag{3.14}$$

the Hamiltonian simplifies to

$$H_{\mathrm{BCS}} = \sum_{\boldsymbol{k}\sigma} \chi_{\boldsymbol{k}} c^{\dagger}_{\boldsymbol{k}\sigma} c_{\boldsymbol{k}\sigma} - \sum_{\boldsymbol{k}} \Delta^{*}_{\boldsymbol{k}}\, c_{-\boldsymbol{k}'\downarrow} c_{\boldsymbol{k}'\uparrow} - \sum_{\boldsymbol{k}} \Delta_{\boldsymbol{k}}\, c^{\dagger}_{\boldsymbol{k}\uparrow} c^{\dagger}_{-\boldsymbol{k}\downarrow} - E_{\mathrm{BCS}} \quad . \tag{3.15}$$

To find the eigenstates of the system and obtain the energies, this Hamiltonian needs to be diagonalized. In the original work by Bardeen, Cooper and Schrieffer, they made use of a Bogoliubov

transformation by introducing new fermionic operators $\gamma_{\boldsymbol{k}\sigma}$ and $\gamma^{\dagger}_{-\boldsymbol{k}\sigma}$. The new quasiparticle operators are related to the electron creation and annihilation operators as:

$$\begin{pmatrix} \gamma_{\boldsymbol{k}\uparrow} \\ \gamma^{\dagger}_{-\boldsymbol{k}\downarrow} \end{pmatrix} = \begin{pmatrix} u^{*}_{\boldsymbol{k}} & -v_{\boldsymbol{k}} \\ v^{*}_{\boldsymbol{k}} & u_{\boldsymbol{k}} \end{pmatrix} \begin{pmatrix} c_{\boldsymbol{k}\uparrow} \\ c^{\dagger}_{-\boldsymbol{k}\downarrow} \end{pmatrix}. \tag{3.16}$$

Physically, this Bogoliubov transformation introduces quasiparticles that are a linear combination of electron and hole states. As such, they still are of fermionic nature and fulfill the anticommutation relations. A unitary transformation satisfies the condition $|u_{\boldsymbol{k}}|^2 + |v_{\boldsymbol{k}}|^2 = 1$. Now, the Hamiltonian can be rewritten in terms of the new quasiparticle operators. In order to make the off-diagonal elements in the Hamiltonian vanish, the parameters for the transformation are found as

$$|u_{\boldsymbol{k}}|^2 = \frac{1}{2}\left(1 + \frac{\chi_{\boldsymbol{k}}}{\sqrt{\chi_{\boldsymbol{k}} + |\Delta_{\boldsymbol{k}}|^2}}\right), \tag{3.17}$$

$$|v_{\boldsymbol{k}}|^2 = \frac{1}{2}\left(1 - \frac{\chi_{\boldsymbol{k}}}{\sqrt{\chi_{\boldsymbol{k}} + |\Delta_{\boldsymbol{k}}|^2}}\right) \tag{3.18}$$

and

$$u_{\boldsymbol{k}} v_{\boldsymbol{k}} = \frac{\Delta_{\boldsymbol{k}}}{2\sqrt{\chi_{\boldsymbol{k}} + |\Delta_{\boldsymbol{k}}|^2}}. \tag{3.19}$$

The resulting Hamiltonian takes the diagonal form

$$H_{\mathrm{BCS}} = \sum_{\boldsymbol{k}\sigma} E_{\boldsymbol{k}} \gamma^{\dagger}_{\boldsymbol{k}\sigma} \gamma_{\boldsymbol{k}\sigma} - E_{\mathrm{BCS}} \tag{3.20}$$

with the energy dispersion

$$E_{\boldsymbol{k}} = \sqrt{\chi^2_{\boldsymbol{k}} + |\Delta_{\boldsymbol{k}}|^2}. \tag{3.21}$$

This result has some interesting physical consequences. In the absence of single quasiparticles, the energy of the superconductor is simply $-E_{\mathrm{BCS}}$, which is the energy of the condensate. Excitations of the superconductor correspond to an addition or removal of a single quasiparticle. This requires the breaking of a Cooper pair. Therefore, the excitation has a minimal energy of $\Delta_{\boldsymbol{k}}$. This parameter is called the superconducting gap parameter. According to Eq. (3.14), the gap parameter contains the interactions between quasiparticles inside the superconductor. In an s-wave superconductor, where the attractive interaction is constant, $V_{\boldsymbol{k}\boldsymbol{k}'} = -V_0$, and assuming weak coupling of quasiparticles, the gap parameter becomes

$$\Delta = 2\omega_0 \exp\left(-\frac{1}{V_0 D(E_{\mathrm{F}})}\right). \tag{3.22}$$

Here, $D(E_{\mathrm{F}})$ is the density of states at the Fermi level in the normal state. With increasing temperature, Δ_0 becomes smaller and vanishes at the critical temperature.

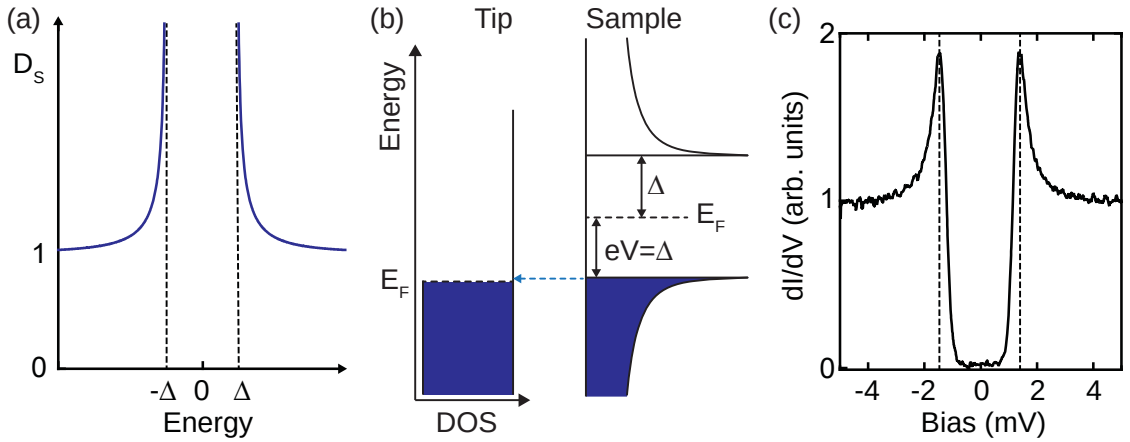

Figure 3.5: (a) Density of states of a BCS superconductor, in units of the normal state density of states. The dashed lines mark the energy of the superconducting gap, where singularities are found. (b) Schematic tunnel junction of a metal tip and a superconducting surface at a bias of $V_{bias}=-\Delta$. Blue areas correspond to occupied states while blank areas are unoccupied states. (c) dI/dV spectrum on Pb(111) at 1.2 K. The quasiparticles are broadened due to finite temperature effects. The feedback was opened at $V_{bias}=5$ mV and $I_{tunnel}=200$ pA.

3.3.3 Superconducting Density of States and Quasiparticle Tunneling

In tunneling spectroscopy, the density of states of a given system is measured. We can compare the density of states between the normal and superconducting state,

$$D_S(E)dE = D_N(\chi)d\chi. \tag{3.23}$$

When we assume a constant density of states around E_F in the normal state, then $D_N(E) = D_0$ and we arrive at an expression for the density of states in the superconductor:

$$\frac{1}{D_0}D_S(E) = \frac{d\chi}{dE} = \begin{cases} \frac{E}{\sqrt{E^2-\Delta^2}} & \text{for } |E| > \Delta \\ 0 & \text{for } |E| < \Delta \end{cases} . \tag{3.24}$$

The density of states of a superconductor is plotted in Fig. 3.5(a). At energies $|E| < \pm\Delta$, there are no states. This region is called the superconducting gap. At the minimal energy required to excite quasiparticles from the condensate, $\pm\Delta$, singularities appear in the density of states. STS on superconductors can be used to probe this density of states. In Fig. 3.5(b), a scheme of a tunnel junction between a metal tip and a superconducting sample are shown. At bias voltages smaller than the threshold $|eV| = \Delta$, no tunnel current flows because no states are present in the sample due to the superconducting gap. Only above a bias voltage of $|eV| = \Delta$, quasiparticles can tunnel from occupied states of the superconductor to unoccupied states in the metal tip (vice versa for opposite bias polarity).

A tunneling spectrum obtained with a metal tip on superconducting Pb is shown in Fig. 3.5(c). The gap around E_F is clearly visible. At a finite temperature of 1.2 K, the quasiparticle peaks acquire a finite width.

3.4 Magnetic Impurities on Superconductors

As we have seen in the previous section, the ground state of a superconductor is formed by Cooper pairs, *i.e.* , antiferromagnetically coupled pairs of electrons. The result is a singlet ground state. Real materials will inevitably contain a finite amount of impurities or defects. What is the influence of such impurities on the superconducting properties?

For s-wave superconductors that are well-described within the framework of the BCS theory, magnetic and non-magnetic impurities have to be discriminated. Non-magnetic impurities do not break time-reversal symmetry. Therefore, they have a minor influence on the critical temperature and on the superconducting gap Δ. This robustness of superconductivity in the presence of non-magnetic impurities is known as the Anderson theorem [112]. It holds for impurity concentrations at which the superconductor can still be treated homogeneous on a scale of the coherence length ξ_0 [109].

Magnetic impurities, on the other hand, have noticeable effects on the properties of a superconductor. In this case, the impurity carries an unpaired spin, which couples to the spins of the quasiparticles via exchange interaction. A weakening of the Cooper pair coupling strength is the consequence and localized states inside the superconducting gap form. For large concentrations of magnetic impurities, superconductivity breaks down. It is worth mentioning that unconventional superconductors are affected by magnetic as well as non-magnetic impurities. A profound understanding of the effects of impurities on superconductivity helps to understand the pairing mechanism in superconductors and could lead towards an explanation for the pairing in high-temperature superconductors.

In the following, we will give an introduction to the effects of magnetic impurities on superconductors. We start with the case of classical impurities and also cover quantum mechanical impurities, which have internal dynamics.

3.4.1 Classical Magnetic Moment on a Superconductor

The effects of magnetic impurities on superconductors are a consequence of the exchange coupling between the magnetic moment of the impurity and the paired quasiparticles of the substrate. The simplest approach to tackle this problem is by considering a classical spin interacting with a superconductor. A classical spin is represented by a magnetic moment localized at the impurity site. In the classical approximation, the magnetic impurity has no internal dynamics such as spin flip processes known from Kondo physics. Consequently, a real magnetic impurity can be considered as a classical spin only for very large spins ($S \gg 1$). An illustration of the situation when a magnetic impurity is present on a superconductor is shown in Fig. 3.6(a). In the substrate, quasiparticles of opposite spin are bound in Cooper pairs. When an impurity is placed on the superconductor, shown in red, its magnetic moment will also couple to the quasiparticle spins

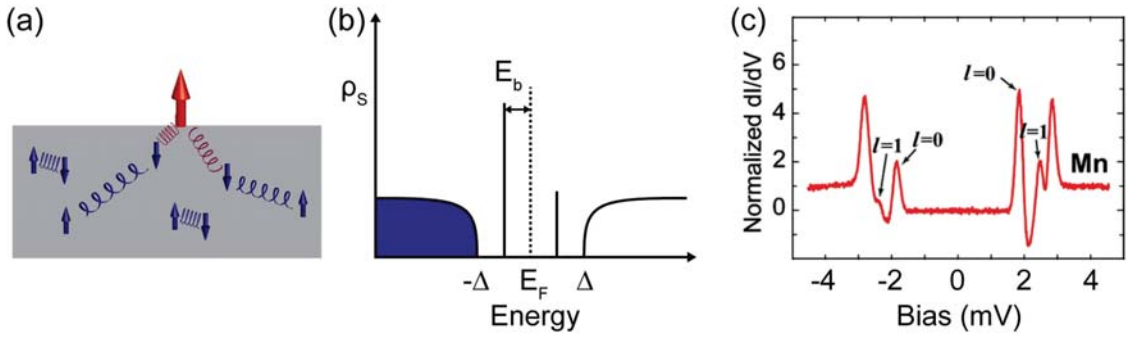

Figure 3.6: (a) Scheme of a magnetic impurity (red arrow) on a superconductor. The impurity spin couples to quasiparticles of the superconducting substrate (blue arrows). Springs represent the coupling strengths. (b) Scheme of the density of states at an impurity site. Inside the superconducting gap, Shiba states are shown at E_b. (c) A dI/dV spectrum recorded on Mn atoms on thin films of Pb on Si(111). Shiba states are present inside the superconducting gap. The spectrum was recorded with a superconducting tip. Figure reprinted from ref. [50].

via exchange coupling. Antiferromagnetic exchange coupling leads to an attractive interaction between the Cooper pair quasiparticle with spin opposite to the impurity spin. At the same time, the quasiparticle with parallel spin is repelled. This counteracts the Cooper pair formation and creates localized states inside the superconducting gap [44–46], which are known as Yu-Shiba-Rusinov (YSR) states. We will refer to these as Shiba states in the remainder of this thesis.

The scattering of superconducting quasiparticles at magnetic impurities was described by H. Shiba [45]. The Hamiltonian consists of the familiar BCS Hamiltonian introduced in section 3.3.1, and an additional term that accounts for the interaction of the superconducting quasiparticles with the magnetic impurity [45],

$$\hat{H} = \sum_{\mathbf{k}\sigma} \chi_{\mathbf{k}} c^{\dagger}_{\mathbf{k}\sigma} c_{\mathbf{k}\sigma} - \Delta \sum_{\mathbf{k}} \left(c^{\dagger}_{\mathbf{k}\uparrow} c^{\dagger}_{-\mathbf{k}\downarrow} + c_{-\mathbf{k}\downarrow} c_{\mathbf{k}\uparrow} \right) - \frac{J}{2N} \sum_{\mathbf{k}\ \mathbf{k'}} c^{\dagger}_{\mathbf{k}} \boldsymbol{\sigma} c_{\mathbf{k}} \cdot \mathbf{S}. \tag{3.25}$$

The impurity spin is described by $\boldsymbol{S}$ and the spin of the substrate quasiparticles by $\boldsymbol{\sigma}$, which are the Pauli spin matrices. J is the exchange coupling constant, which determines the preferred alignment of the spins. For $J < 0$, the exchange interaction is antiferromagnetic, whereas $J > 0$ indicates a ferromagnetic exchange. To this date only antiferromagnetic coupling to magnetic impurities has been observed in experiments. We will therefore focus the discussion on the case $J > 0$. The solution of the Hamiltonian in Eq. (3.25) predicts a pair of localized excitations inside the superconducting gap at energies

$$E_{\mathrm{b}} = \pm\Delta \frac{1 - ((J/2)S\pi D_{\mathrm{N}}(E_{\mathrm{F}}))^2}{1 + ((J/2)S\pi D_{\mathrm{N}}(E_{\mathrm{F}}))^2}, \tag{3.26}$$

with $D_{\mathrm{N}}(E_{\mathrm{F}})$ as the density of states at the Fermi level in the normal state. These localized excitations, the Shiba states, are symmetric around E_{F}. Their energy depends on the supercon-

ducting gap parameter Δ as well as on the impurity spin S and the exchange coupling parameter J. In a physical sense, Shiba states correspond to excitations of the superconductor lowered in energy by the exchange interaction with the magnetic impurity. With the appearance of Shiba states inside the gap, the BCS quasiparticle peaks at the gap edge decrease in intensity [113, 114]. For weak exchange coupling, the ground state of a superconductor with magnetic impurities is characterized by a singlet of the Cooper pairs in the superconductor and the impurity with spin S. An excitation of the system by adding/removing a single quasiparticle to/from the continuum yields an unpaired quasiparticle in the superconductor, with a spin antiparallel to the impurity spin.

If the exchange coupling strength $w = JS/2$ is increased, the bound state [Eq. (3.26)] crosses zero energy. At this point, the exchange coupling between the substrate quasiparticles is equal to the exchange coupling between the impurity spin and the substrate quasiparticles. A phase transition occurs and the new ground state is described by a broken Cooper pair in the superconductor and a quasiparticle spin antiferromagnetically coupled to the impurity [115–117]. The impurity spin is thus reduced to $S - 1/2$.

A scheme of the density of states of a superconductor with a magnetic impurity is shown in Fig. 3.6(b). The Shiba states are localized at $\pm E_\mathrm{b}$. Measurements on magnetic impurities on superconductors using STS confirmed the presence of Shiba states [49–51, 118]. One example is shown in Fig. 3.6(c), which shows the presence of Shiba states on Mn atoms on thin films of superconducting Pb [50]. There, the spectra were recorded using a superconducting tip, which leads to a convolution of the density of states of the tip and surface. This will be discussed in chapter 5.

Interestingly, the Shiba states at positive and negative bias exhibit different spectral intensities. In case of purely magnetic scattering, both components of the Shiba state are expected to have equal intensities. However, if potential scattering is present, the Coulomb interaction U leads to an asymmetry in the intensities. This simply means it becomes favorable to excite the system by either removing an electron (larger intensity in the electron-like component) or adding one (larger intensity in the hole-like component). Note that the energy of the excitation, E_b is not changed.

3.4.2 Quantum Mechanical Spin on a Superconductor

The model of a classical spin does not capture internal dynamics of the impurity, such as spin-flip processes in the impurity spin or the substrate. In order to include such effects, the impurity has to be treated as a quantum spin. As explained in the section 3.2 on the Kondo effect, the interaction of a localized spin with itinerant conduction electrons leads to a screening of the magnetic moment of an impurity. On a superconductor, the pairing of states around E_F reduces the number of free electrons that can participate in these screening processes. As a consequence, the Kondo screening of the impurity spin is incomplete. This coexistence of Kondo processes and superconductivity has been adressed by theory [52, 119–121] and experiment [51, 122, 123].

Matsuura [119] predicted a phase transition between the two ground states corresponding to a screened and unscreened spin (see Fig. 3.7). The point at which the phase transition takes place depends on the relation between the scale of the Kondo screening, characterized by the Kondo temperature, and the size of the superconducting gap. For the case when Kondo correlations

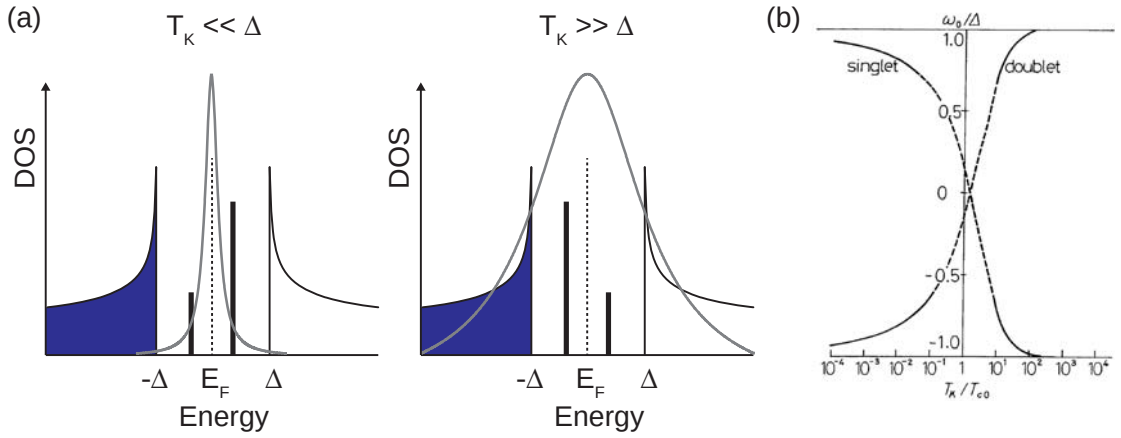

Figure 3.7: (a) Schemes to illustrate the quantum phase transition due to Kondo screening. The left part shows the density of states in the case $T_K \ll \Delta$. The comparably large superconducting gap depletes states involved in the Kondo screening process. The Shiba state has a higher intensity at positive energy. In the right, the case $T_K \gg \Delta$ is depicted. The width of the Kondo resonance exceeds the superconducting gap thus the Shiba state intensity is higher at negative energies. (b) Energy diagram of the quantum phase transition. The Shiba state energy, normalized to the superconducting gap parameter is plotted as a function of the Kondo temperature. At low T_K, the subgap state is an excitation to a singlet while for large Kondo temperatures the ground state is a singlet and the excitation happens to a doublet. Figure adapted from Ref. [119]

are less effective than the superconducting pairing, *i.e.* $T_K \ll \Delta$, impurity spin is unscreened. This case is illustrated in the left part of Fig. 3.7(a). Due to the large superconducting gap, no free electrons are available to participate in the Kondo screening process. In this ground state, the Shiba state spectrum is characterized by a larger intensity in the Shiba state component at positive energy. In the case when $T_K \gg \Delta$, a sufficient number of normal state electrons outside the superconducting gap contribute to the screening of the impurity spin. At a critical Kondo temperature T_K the ground state becomes a Kondo screened singlet and the bound state is the excitation to a doublet state. In this approach, the energy of the subgap bound state E_b has been calculated to be

$$E_b = \pm\Delta\left(\frac{1-\alpha^2}{1+\alpha^2}\right) \tag{3.27}$$

where α depends on the Kondo temperature and the superconducting gap parameter Δ as

$$\alpha \approx \frac{\pi\Delta}{4T_K}\ln\left(\frac{4eT_K}{\pi\Delta}\right). \tag{3.28}$$

Ref. [121] found the transition to take place at a ratio T_K/Δ=0.3 for spin 1/2. For T_K/Δ<0.3, the spin is unscreened and at T_K/Δ>0.3 it is screened. As a consequence, the bound state crosses the Fermi level at the point of the quantum phase transition.

The Kondo screening is governed by the exchange coupling to the substrate electrons, J. In section 3.4.1, the strength of the exchange coupling also determined the ground state of the system. Both processes are thus related to the exchange coupling and the Kondo effect as well as the Shiba states are a manifestation of the same processes. In chapter 5, we will investigate a system where this coexistence can be probed and the quantum phase transition between two ground states can be characterized by both the Kondo temperature as well as the Shiba state energy [51, 52, 124].

Chapter 4

Molecular Switching of Diarylethene with the Scanning Tunneling Microscope

This chapter is based upon the publication:

- *"Diarylethene Molecules on a Ag(111) Surface: Stability and Electron-Induced Switching"* by J. Wirth, N. Hatter, R. Drost, T. R. Umbach, S. Barja, M. Zastrow, K. Rück-Braun, J. I. Pascual, P. Saalfrank and K. J. Franke, *The Journal of Physical Chemistry C* **119**, 4874-4883 (2015)

4.1 Introduction

Electronic devices using single molecules as active electronic elements may replace conventional semiconductor technology in the future. Their advantage is not only in the small size but quantum effects may lead to new properties in molecular electronics. Since first proposal for a single molecule diode [3], other applications for individual molecules have been conceived. They include single molecule transistors [4, 125, 126], molecular motors [2, 127, 128] and molecular switches [16, 129, 130]. The latter received intense attention in the past decades, as many different molecules can be used as molecular switches. The switching process can be triggered by different external stimuli, such as light [17, 131], electric field [15, 132] and tunneling electrons [16, 133]. Switching the isomeric state allows the control of physical properties like electrical conductance or optical absorption bands [134]. In the following, we will introduce the basic concepts of molecular switches and give a short overview of different categories of molecular switches.

4.1.1 Molecular Switches

A molecular switch is a single molecule that can be switched between two stable configurations by external stimuli. Various classes of molecular switches have been identified in the last decades. Two widely investigated classes are: i) molecules, which can be switched between two different conformations and ii) molecules, where the switching process induces a bond formation or breaking.

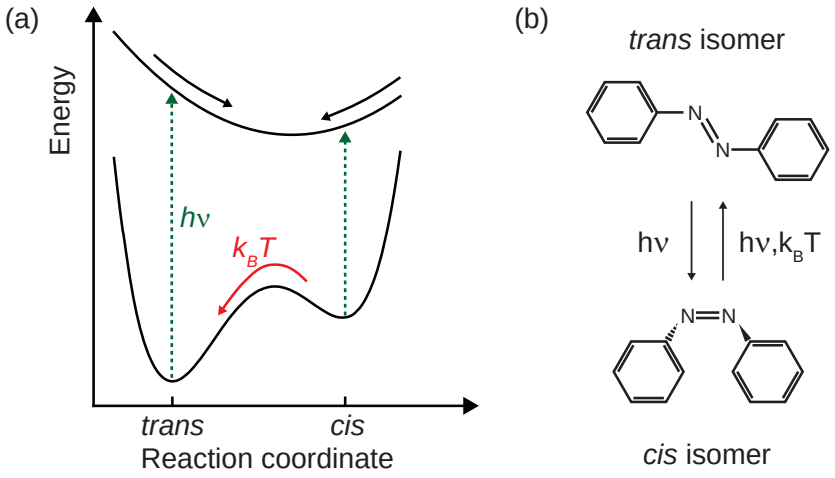

Figure 4.1: (a) Potential energy surface of ground state and excited state of a molecular switch. Photoexcited switching (green dashed line) takes place via the excited state. Thermal switching (red arrow) happens in the molecular ground state (adapted from [135]). (b) Two stable configurations of an azobenzene molecule. Switching from the *trans* to the *cis* configuration and vice versa can be triggered by light and the *cis*-*trans* isomerization by temperature.

The efficiency and reversibility of molecular switching has been demonstrated for molecules in solution and in molecular crystals [129, 130]. However, direct adsorption of the functional entity on a surface can drastically alter the electronic properties of the molecules [22, 135]. A consequence is the modification of the minimal potential energy surfaces for reaction pathways. For molecular switches on surfaces, inverted isomer stabilities with respect to the gas phase [23, 136, 137] or a suppression of the bistability have been observed [24, 135, 138–142]. Yet, a supporting substrate is essential to realize electric circuits.

Azobenzenes are a well-known class of molecular switches, investigated in solution as well as on surfaces. In addition, they were among the first molecular switches investigated by STM on metal surfaces. The reversibility of the switching of azobenzene is often inhibited on surfaces [24, 142]. However, attaching four *tert*-butyl groups to decouple the switching unit from the substrate has shown to restore the reversibility [15, 17]. Azobenzenes undergo an isomerization reaction, which is a change of the molecular geometry without a change of the chemical structure. A *trans*-*cis* isomerization can be induced by light [141], tunneling electrons [133] or an electric field [15]. A schematic model of the potential energy landscape of azobenzene is shown in Fig. 4.1(a), where the ground state potential energy surface has local minima in the *trans* and *cis* isomeric state, respectively. The *trans*-*cis* isomerization can take place in the excited state, which is accessed by absorption of a photon, whereas the back reaction can be driven by photons or temperature. The thermal switching reaction takes place in the molecular ground state. Lewis structures of the *trans* and *cis* isomer are shown in Fig. 4.1(b). The *trans* configuration is planar, whereas the *cis* configuration is three-dimensional, caused by a steric repulsion of the two phenyl rings.

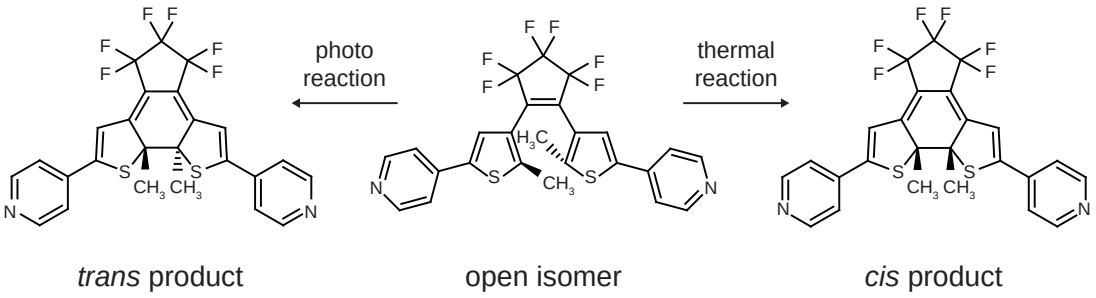

Figure 4.2: Lewis structures of PDTE in the open form (center) and both electrocyclic products according to the photochemical reaction (left) and the thermal reaction (right).

In technical applications, a molecular switch often needs to be contacted by electric leads on two sides, thus a large structural change during molecular switching is not desired. Diarylethenes are photochromic switches that undergo a ring-opening/-closing reaction, which has a small influence on the molecular geometry. A conjugated π-electron system in the ring-closed (closed) is transformed into a non-conjugated system in the ring-open form and vice versa. Therefore, both isomers feature a largely differing electrical conductance, due to the conjugated π-electron system. The conductance on/off-ratios amount to values of 30 [143–145]. The conductance G in the closed form of diarylethene was determined in break junction experiments as $(3.3 \pm 0.5)\text{x}10^{-5}$ G_0 with G_0 as the quantum of conductance. This makes diarylethenes valuable candidates as switches in nanoscale electronic circuits. Furthermore, the directionality of the switching is provided by different absorption wavelengths to induce the ring-opening reaction (UV-light) and the ring-closing reaction (visible light).

Many STM studies were performed on diarylethenes in self-assembled monolayers (SAMs) on surfaces. Specific methyl groups acted as spacer to decouple the electronic states from the substrate [14, 146, 147]. In these systems, reversible light-induced switching was observed and the effect of the end groups characterized. When directly connected to a metallic substrate, the switching unit itself can hybridize with the states in the substrate, which affects the switching properties.

In this chapter, we study the switching behavior of *4,4'-(4,4'-(perfluorocyclopent-1-ene-1,2-diyl)bis(5-methylthiophene-4,2-diyl)dipyridine* (PDTE) on the Ag(111) surface. In contrast to recent studies, here the PDTE molecule is directly adsorbed on a Ag(111) surface, thus the switching unit interacts with the electronic states of the substrate. As substrate we chose Ag(111), because the bond strength of the sulfur in the thienyl groups to Ag is weak compared to Cu or Au [148]. A strong bond to the surface likely inhibits a successful switching of the molecule. STM experiments are complemented by density functional theory (DFT) calculations performed in the group of Peter Saalfrank at the university of Potsdam. The PDTE molecules in the ring-open form were synthesized in the group of Karola Rück-Braun at the department of chemistry at Technische Universität Berlin.

Fig. 4.2 displays the Lewis structures of PDTE in the open form (middle) and two closed forms (left and right). The hexatriene switching unit in the open form is clearly visible in the center of the molecule. The switching process leads to the formation of a bond between the two carbon atoms, at which the methyl groups are attached. This reaction can proceed in two different ways, depending on the reaction pathway. The reaction products and their stereochemistry in solution are determined by the Woodward-Hoffman rules [149]. We will shortly introduce them in the following.

4.1.2 Woodward-Hoffmann Rules

The product of a chemical reaction is determined by the reaction mechanism. In this sense, a thermally induced reaction may lead to a different product than a photochemical reaction. For certain chemical reactions, rules have been found to easily identify reaction products based on the properties of the system.

In 1965, Woodward and Hoffmann published a set of rules to predict reaction barrier heights for electrocyclic ring-closing/-opening reactions [149], nowadays known as Woodward-Hoffmann rules. They are based on the conservation of the symmetry of the orbitals involved in the bond formation/breaking. Two reaction mechanisms have to be distinguished: a thermal reaction and a photochemical reaction. In a thermal reaction, heat provides the energy necessary to activate the electrocyclic reaction, which takes place in the electronic ground state of the system. On the other hand, in a photochemical reaction, the system is excited into an electronically excited state by a photon. Then, the reaction takes place in the excited state. The Woodward-Hoffmann rules can be stated as follows [150]:

1. A thermal reaction involving $4n$ π electrons proceeds in a conrotatory manner.
2. A thermal reaction involving $(4n+2)$ π electrons proceeds in a disrotatory manner.
3. A photochemical reaction involving $4n$ π electrons proceeds in a disrotatory manner.
4. A photochemical reaction involving $(4n+2)$ π electrons proceeds in a conrotatory manner.

A conrotatory manner in this respect indicates a rotation of the atomic orbitals in the same rotational sense. In a disrotatory reaction, they rotate in opposite directions. As an example to illustrate the Woodward-Hoffman rules, we apply them to the electrocyclic ring-closure of PDTE. We consider the $1,3,5$-hexatriene unit, as depicted in Fig. 4.3(a). It consists of six carbon atoms. In the open form, there is no bond between the two C atoms in the front. Remember that these are the C atoms, where the methyl groups in PDTE are attached. The molecular orbitals of the hexatriene unit are formed by the p_z atomic orbitals of the carbon atoms. Therefore, the number of involved electrons corresponds to the case of $4n+2$ electrons, where n=1. All six combinations of the atomic orbitals to molecular orbitals are shown in Fig. 4.3(a) and orbitals with an increasing number of nodal planes are higher in energy. Fig. 4.3(b) shows the occupation of the orbitals by electrons of the carbon atoms. The three lowest orbitals in Fig. 4.3(a) are each doubly occupied. A thermal reaction is driven by heat and takes place in the molecular ground state, thus the bond formation is determined by the symmetry of the highest occupied molecular orbital (HOMO). A

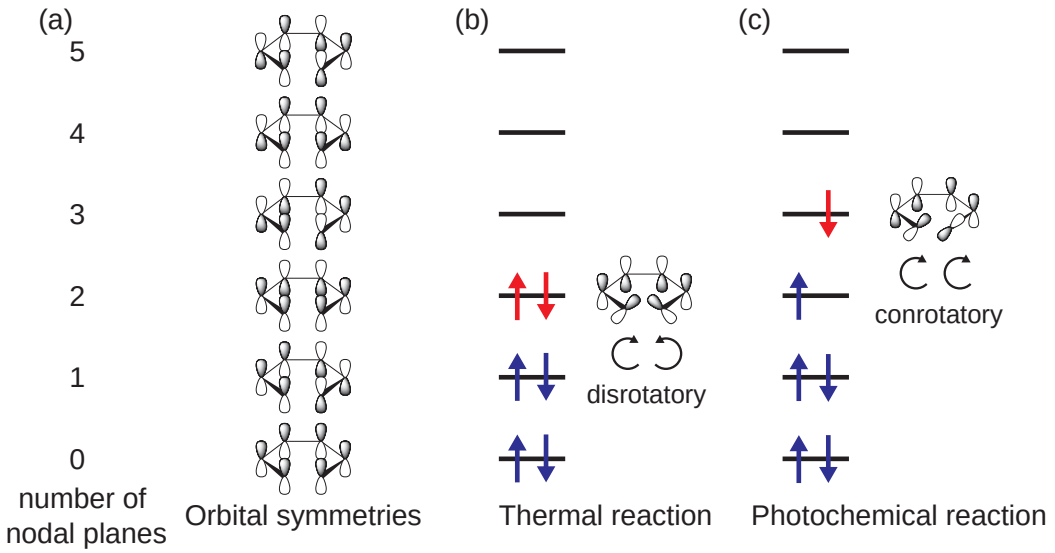

Figure 4.3: Illustration of the Woodward-Hoffmann rules: (a) Orbital symmetries of the molecular orbitals of a $1,3,5$-hexatriene unit. The orbital energies increase from the bottom to the top. (b) Occupation of the orbitals by the carbon p_z-electrons and the bond formation for a thermal reaction, which involves the HOMO. (c) Occupation of molecular orbitals after photochemical excitation leading to a conrotatory rotation.

chemical bond requires a constructive overlap of atomic orbitals, so the orbitals of the two carbon atoms have to undergo a disrotatory rotation, as shown in Fig. 4.3(b). This is in agreement with the third Woodward-Hoffman rule. For the case of PDTE, a disrotatory rotation of the carbon orbitals also involves a disrotatory rotation of the methyl groups and leads to the *cis*-product shown in the right of Fig. 4.2.

On the other hand, in the photochemical reaction, a photon excites an electron into the lowest unoccupied molecular orbital (LUMO). Now, the ring-closing reaction takes place in the LUMO, as shown in Fig. 4.3(c). Due to the different symmetry of this orbital, the reaction follows a conrotatory rotation, in agreement with the fourth Woodward-Hoffman rule. The conrotatory reaction results in a conrotatory rotation of the methyl groups attached to the carbon atoms and the *trans*-product in the left of Fig. 4.2 is the result of this reaction pathway.

When molecules are adsorbed on a surface, the reaction may not happen according to the Woodward-Hoffman rules. The potential energy surfaces of the ground and excited states can be changed by a steric hindrance or induced dipole moments due to the presence of the surface. We will now turn to the experiments performed on PDTE adsorbed on the Ag(111) surface and investigate its switching ability.

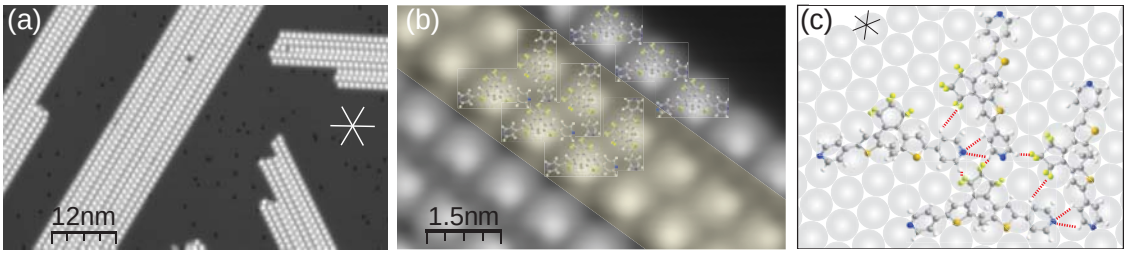

Figure 4.4: Adsorption of PDTE on Ag(111): (a) Large-scale STM image of PDTE molecular islands, oriented along the high-symmetry axes of Ag(111). Small white lines indicate the growth directions of PDTE islands (Scanning parameters: V_{bias}=1 V, I_{tunnel}=170 pA). (b) Detailed image of the molecular arrangement within the islands. Structural models of the open isomer of PDTE are superimposed to emphasize the orientation of PDTE (Scanning parameters: V_{bias}=−1 V and I_{tunnel}=80 pA). (c) Model of PDTE arranged as in the yellow shaded part in (b) with red dashed lines indicating hydrogen bonds. Figure adapted from [151].

4.2 Adsorption of PDTE on Ag(111)

PDTE was evaporated from a Knudsen cell held at a temperature of 375 K. During the evaporation, the clean Ag(111) surface was at room temperature. Directly after, the sample was transferred into the pre-cooled STM. All measurements were performed at a temperature of 4.8 K and a base pressure below 10^{-10} mbar.

We find PDTE molecules self-assembled in chain-like molecular islands, which are oriented along the three high-symmetry axes of the hexagonal Ag substrate. A typical STM topography is shown in Fig. 4.4(a), where the threefold symmetry of the arrangement of islands on the surface can be clearly seen. The black dots on the Ag substrate correspond to residual CO molecules that are present in the vacuum chamber during the preparation. Their presence on Ag does not influence the formation of PDTE islands. The internal structure of the PDTE islands reveals rows of single molecules. In a magnified view on a typical PDTE island, depicted in Fig. 4.4(b), the orientation of individual PDTE molecules can be understood. Each molecule consists of a bright protrusion in the center, attributed to the hexatriene switching unit. This is surrounded by a sickle shaped lower part, corresponding to the hexafluoro-cyclopentene and the pyridine end groups. The association of the central protrusion with the switching unit is supported by the symmetric appearance of the molecules. All molecules have the same topographic appearance, so we assume only one isomer is present on the surface. Molecular models of the open isomer of PDTE are superimposed in Fig. 4.4(b) and illustrate the arrangement within the islands.

Molecules within a row are oriented in the same direction, whereas molecules in neighboring rows are rotated by an angle of (90±1)°. The yellow shaded area in Fig. 4.4(b) highlights two rows of PDTE, where the molecules are oriented such that the hexafluoro-cyclopentene groups point towards the respective other molecular row. In this arrangement, the rows seem to be closer to each other as compared to the other neighboring rows in the island. This configuration can be explained by stabilizing intermolecular interactions, as illustrated in the schematic

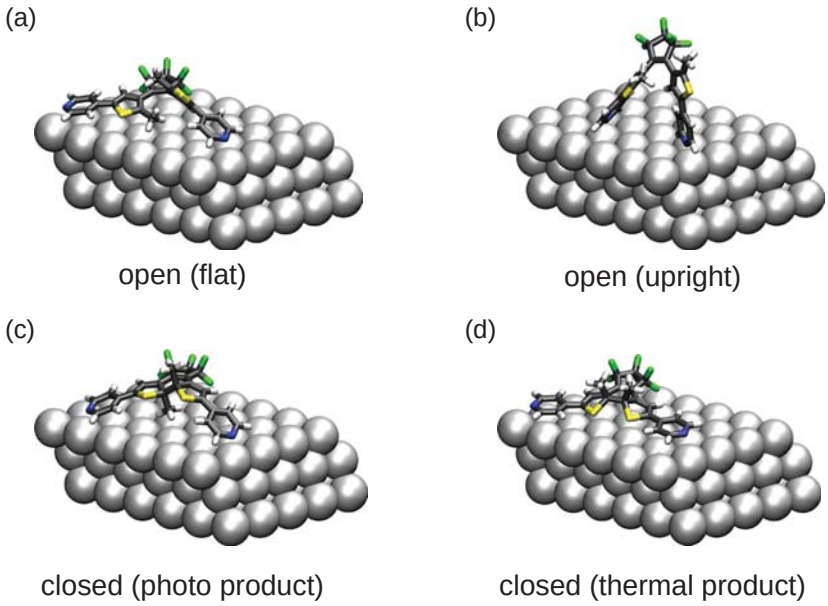

Figure 4.5: Geometric models of the four considered structures. (a) Open outstretched flat (o-flat) configuration. (b) Open upright (o-upright) configuration with only pyridine groups bonding to the substrate and the methyl groups aligned parallel. (c) Closed form after the photochemical reaction (c-*trans*) with the methyl groups in a *trans* configuration. (d) Ring-closed product after the thermal reaction with the methyl groups in a *cis* configuration (c-*cis*). Figure adapted from [151].

model in Fig. 4.4(c). Hydrogen bonds are formed between the fluorine atoms in the perfluorocyclopentene groups of one molecule and hydrogen atoms in the pyridine groups of the molecule in the neighboring row.

Larger islands of PDTE do not only consist of such double row structures. Single rows are present within islands and form at the edges of molecular islands as well. We believe this is a result of the interplay between intermolecular interactions and the interaction of PDTE with the Ag surface.

In order to get a clear picture of the isomeric state present on the surface, theoretical calculations of the thermodynamic stability and adsorption energy were performed in the group of Peter Saalfrank at the University of Potsdam. The calculations are based on density functional theory (DFT), using the plane-wave (PW) 91 functional. Four different isomers are considered, which might form on the substrate. The molecules and the substrate were modeled as slabs. Each slab includes one PDTE molecule and three Ag layers, as shown in Fig. 4.5. The lowest Ag layer was restricted to the bulk lattice constant of 4.157 Å and the surface layer was a (6 x 5) supercell with variable lattice constant. The PDTE isomers were oriented on the substrate in agreement with the symmetry axes similar to Fig. 4.4. Under these conditions, the geometries

Table 4.1: Theoretical adsorption energies E_{ads} of the four PDTE species on Ag(111).

	E_{ads}/eV (without dispersion)	E_{ads}/eV (with dispersion)
o-flat	−0.11	−2.32
o-upright	−0.53	−1.39
c-*trans*	+0.01	−1.99
c-*cis*	−0.32	−2.97

were optimized, allowing for bond formations of the nitrogen atoms of the pyridine end groups to the surface. To facilitate the interpretation of the results, the optimal geometries in gas phase were also calculated.

Two open isomers and two closed isomers are considered. The open isomer shown in Fig. 4.5(a) adsorbs flat on the surface in an outstretched configuration. It is called open flat isomer (*o-flat*). The second open isomer, shown in Fig. 4.5(b) assumes an upright adsorption configuration on Ag(111). In this configuration, only the nitrogen atoms of the pyridine end groups form bonds to the substrate. This structure is called open upright structure (*o-upright*). Both isomers with a closed ring form adsorb flat on the surface. They are the reaction products according to the Woodward-Hoffmann rules. The photo product, which results from a conrotatory ring closure, has its methyl groups aligned in a *trans* configuration, depicted in Fig. 4.5(c). Therefore, it will be referred to as c-*trans* isomer in the remainder of this chapter. The second ring-closed isomer is the thermal product, which follows from a disrotatory reaction. Both methyl groups point in the same direction, in this case away from the substrate, shown in Fig. 4.5(d). This structure is called c-*cis*.

The resulting adsorption energies are presented in Table 4.1. Negative values indicate a lowering of the system energy upon adsorption on the surface. For supermolecular arrangements on metal surfaces, dispersion interactions have a large influence on the adsorption structure as well as the dynamics [152]. To get an idea about the contribution of dispersion interactions in the present system, calculations with and without dispersion interactions were performed. If no dispersion interactions are included, the adsorption energies of the four isomers range from −0.5 eV for the o-upright configuration to 0.01 eV for the c-*trans* configuration. The o-upright isomer seems to be the preferred configuration on the surface. This result arises from the fact that in the absence of dispersion interactions, the main contribution to the adsorption energy originates from the bonds between the nitrogen atoms in the pyridine groups with the Ag surface atoms. Due to the steep angle of the pyridine rings with respect to the surface, the nitrogen atoms are relatively close to the substrate in this configuration. In the c-*trans* configuration, on the other hand, the methyl group that points towards the surface lifts the molecular backbone and the end groups off the surface and therefore weakens the bond. This steric hindrance is enforced by the additional higher stiffness of the closed form with respect to the open isomer. Therefore, it renders this configuration less favorable than the open flat configuration.

The situation changes considerably when dispersion interactions are included. In general, the absolute values of the binding energies for all considered isomers increase due to the high contribution of the dispersion interaction. Now, the most favorable configuration is the c-*cis* form with

Table 4.2: Relative stabilities of potential PDTE species in the gas phase and on the Ag(111) surface, taking the o-flat isomer as a reference point. All energies are given in eV.

	open upright ΔE	closed *trans* ΔE	closed *cis* ΔE
gas phase	0.03	0.57	1.17
gas phase layer	0.23	0.50	1.24
surface layer	0.93	0.84	0.59

a binding energy of −2.97 eV, followed by the o-flat configuration. The large changes can be explained by the adsorbate's flexibility to move closer to the substrate. This effect is largest for the c-*cis* form, where the complete molecular backbone can move close to the substrate and the sulfur atoms in the thienyl groups form weak covalent bonds to Ag. The same reasons are accountable for the relatively low contribution to the adsorption energy in the o-upright configuration. Since only the pyridine groups are directly connected to the substrate, no additional interactions contribute to its stabilization on the surface. We find that this configuration is the least favorable. The o-flat isomer has the second largest adsorption energy and is therefore another candidate for the adsorbate present on the surface, especially because the evaporated molecules were in the open form.

In the results for the adsorption energies, no intermolecular interactions within the adlayer are included. Additionally, the internal energy of a molecule can be different in the open and closed isomers. Therefore, the relative thermodynamic stabilities with respect to the open flat isomer were calculated and are given in Table 4.2. In general, a system is thermodynamically stable when its energy can not be lowered by undergoing a chemical reaction. A chemical reaction will take place, if the system energy can be lowered by the process, provided the activation barrier can be overcome. In Table 4.2, positive values of the relative thermodynamic stability indicate a destabilization of the respective isomer. In these cases, energy has to be provided to the system in order to induce the reaction. Such reactions are endothermic.

Three situations are considered: i) molecules in gas phase, ii) a molecular adlayer in gas phase (without substrate) and iii) a molecular layer adsorbed on the Ag surface. The results for the three cases enable an estimation of the contributions of intermolecular interactions in the adlayer and interactions of the molecules with the substrate. In the gas phase, the o-flat isomer is most stable, followed by the o-upright isomer with a slightly higher energy. Less stable are the closed isomers with energies 0.57 eV above the o-flat isomer for c-*trans* and 1.17 eV for c-*cis*. In a pure molecular layer, the open flat configuration is still the most stable configuration. When the adlayer is supported on the silver substrate, the order of stabilities changes. The o-flat isomer is still the most stable configuration. However, the o-upright isomer is least stable with an energy of 0.93 eV higher with respect to the o-flat isomer. The closed isomers are more stable than the o-upright isomer, owing to the proximity of the molecular backbone to the surface. This effect is strongest for the c-*cis* isomer being the second most stable with a difference of 0.57 eV, followed by the c-*trans* form at sightly higher energy.

From these results of the calculations combined with the fact that we evaporated the open form of PDTE, we suggest that the o-flat isomer is present on the surface. To support these findings and check for a possible tip-induced switching of the isomeric state, $\mathrm{d}I/\mathrm{d}V$ spectra were recorded on PDTE and compared to calculations of the projected density of states (PDOS), which will be discussed in the following section.

4.3 Tip-induced Switching of PDTE

Fig. 4.6(a) shows the topography of a molecular island with all molecules in the initial configuration. We can induce a transformation of individual molecules by applying a voltage pulse $\geq$1.5 V. For this, the STM tip is positioned above one molecule, marked by the black arrow. Then, the feedback loop is disabled and the bias voltage continuously increased, as depicted in Fig. 4.6(b). At a certain bias voltage of $\mathrm{V_{bias}}$=2.2 V in the example, an abrupt drop of the tunneling current is observed, reminiscent of a change of the adsorbate. After the current drop, the current remains low on the backward sweep, shown by the red curve in Fig. 4.6(b). This indicates the stability of the change. An STM image recorded after the voltage pulse, shown in Fig. 4.6(c), reveals a change of the addressed molecule (indicated by a red arrow). Imaged at a bias of -1 V, it appears higher in topography and its structure has changed. However, the limited intramolecular resolution inhibits an assignment of the final state.

Information of the electronic structure of both isomers can be used to assign the isomers on the surface. $\mathrm{d}I/\mathrm{d}V$ spectra are recorded on PDTE before and after the tip-induced transformation. For the spectroscopy, a lock-in amplifier was used with a bias modulation of V_{rms} =10 mV to 15 mV and a frequency of 833 Hz. In Fig. 4.6(d), a $\mathrm{d}I/\mathrm{d}V$ spectrum on a PDTE molecule before the transformation is shown. At positive bias voltage, *i.e.* , when probing unoccupied states, a large resonance is resolved at approximately 2 V, which we attribute to the LUMO of PDTE. At negative bias, no resonance is observed within the spectroscopically accessible range to -2.3 V. The band gap of the initial isomer is thus determined to be larger than 3 eV. Spectra recorded after the voltage pulse [Fig. 4.6(e)] reveal states at energies below -1 V. At positive energies, the LUMO resonance shifts to slightly higher values. Overall, the molecular band gap decreases, typical for a ring-closing reaction induced by the tip [153]. The upward shift of the LUMO explains the current drop during the tip-induced change. At the same time, the molecule appears brighter in STM images at -1 V, because the additional states at that energy contribute to the conductance.

The site-projected density of states (PDOS) was calculated using DFT in order to correlate it with the $\mathrm{d}I/\mathrm{d}V$ spectra of the two isomers before and after the tip-induced transformation. The calculated PDOS of the four considered configurations is presented in Fig. 4.7. Both open isomers display band gaps larger than 2 eV, resulting from the non-conjugated electron system. The LUMO resides close to E_{F} while there are no states at low negative energies. In contrast, the closed isomers exhibit states around the Fermi level as a consequence of the ring-closed form with a conjugated π system.

By comparing the calculated PDOS with the experimental spectra in Fig. 4.6(d) and (e), the large energy gap of the open isomers scales with the measured gap of the initial PDTE isomer. Additionally, the usual underestimation of band gaps in DFT calculations [154] suggests

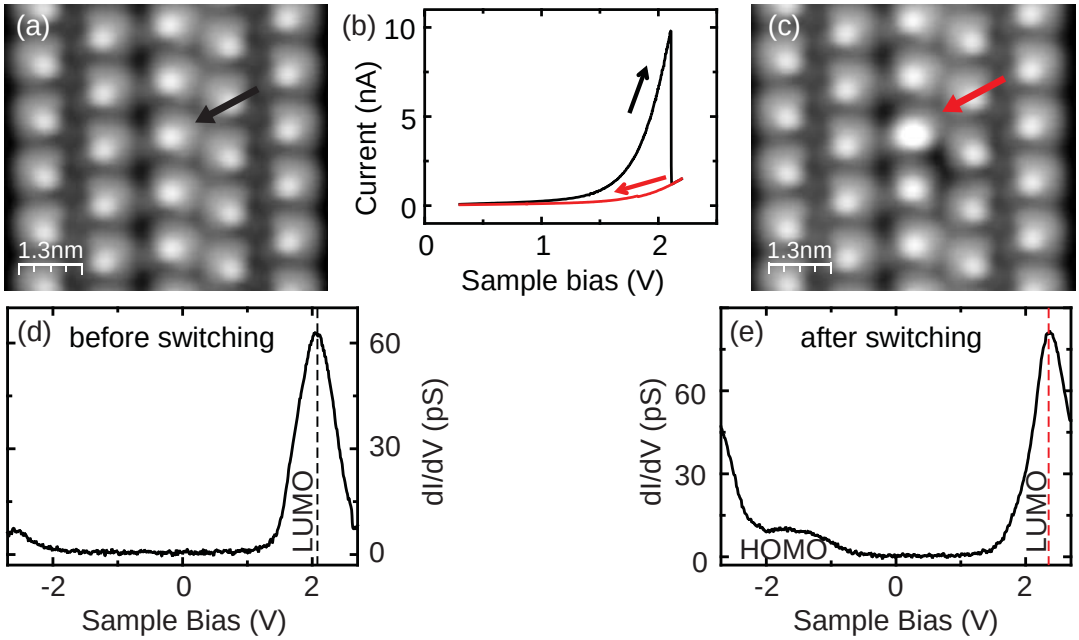

Figure 4.6: Switching of PDTE: (a) STM image of a part of a molecular island (Scanning parameters: V_{bias}=−1 V, I_{tunnel}=100 pA). (b) Voltage pulse on the PDTE marked by a black arrow in (a). Feedback opened at V_{bias}=300 mV and I_{tunnel}=75 pA. (c) Same area as in (a) scanned after tip-induced voltage pulse. The red arrow marks the PDTE, to which the voltage pulse was applied. The molecule appears brighter. Scanning parameters are: V_{bias}=−1 V and I_{tunnel}=100 pA. (d) dI/dV spectrum on PDTE before tip induced transformation. The LUMO resonance is marked by the black dashed line. (e) dI/dV spectrum on PDTE after transformation. The shifted LUMO is marked by the red dashed line. Feedback opened at: V_{bias}=2.7 V, I_{tunnel}=50 pA. Figure adapted from [151].

an even larger band gap for the open isomers, further supporting the similarity. Including the thermodynamic stabilities, which basically rule out the o-upright isomer due to its low stability, we conclude that the initial isomer after deposition of PDTE is the open isomer in a flat adsorption configuration.

The smaller band gap in the calculations for the closed isomers is similar to the reduction of the HOMO-LUMO gap observed in the dI/dV spectra. It is likely that PDTE after the transformation is in the ring-closed configuration. The calculated PDOS of the c-*trans* isomer exhibits a large weight directly at E_F while the c-*cis* isomer only exhibits low density of states at the Fermi level and a well-resolved highest occupied molecular orbital (HOMO) resonance at ≈−0.8 eV. Physically, this difference between the c-*trans* and c-*cis* isomer has its origin in a larger charge transfer from the substrate to the c-*cis* molecule. PDOS calculations of the c-*cis* isomer in the gas phase layer exhibit a similar PDOS as for the c-*trans* isomer adsorbed on the surface, with two peaks corresponding to the HOMO and LUMO. Concluding from the densities of states

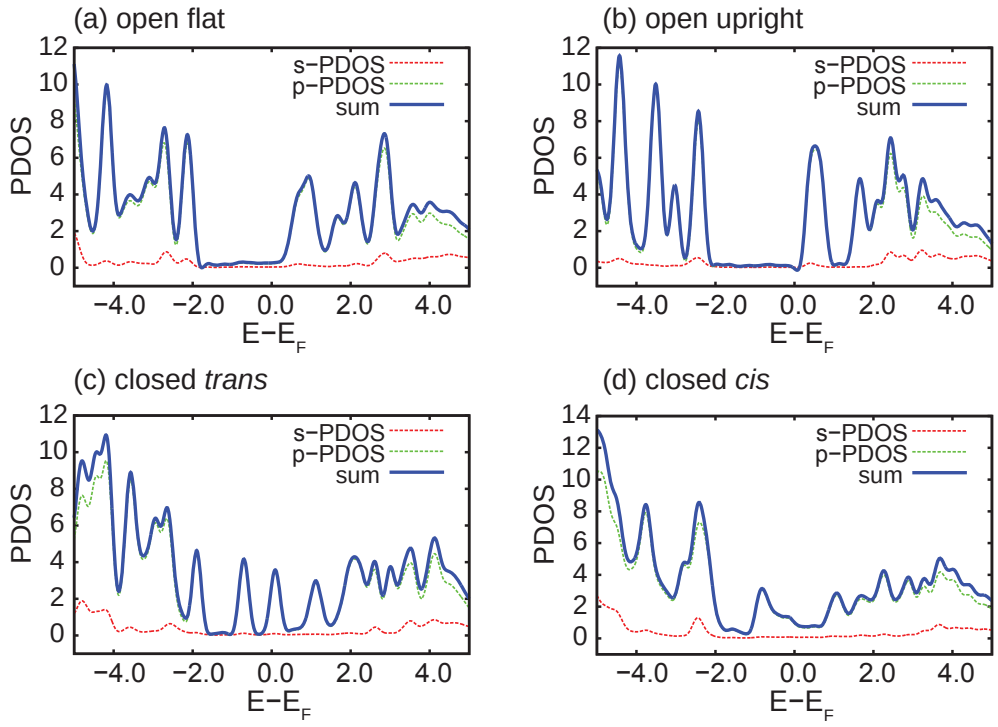

Figure 4.7: Calculated PDOS of the four isomer models adsorbed on the surface. (a) open flat isomer, (b) open upright, (c) closed *trans* configuration and (d) closed *cis* configuration. Figure adapted from [151].

for the closed isomers, the result for the c-*cis* isomer agrees better with the experimental data recorded on the isomer after the transformation in Fig. 4.6(e). Furthermore, taking into account the higher thermodynamic stability of the c-*cis* form, it can be identified with the isomer obtained by the tip-induced transformation.

A picture can now be established in which the open flat isomer is switched to the closed *cis* isomer by the STM tip. Therefore, we believe to induce a ring-closing reaction with the STM tip. According to the Woodward-Hoffmann rules, the reaction leading to the c-*cis* product proceeds in a disrotatory rotation of the carbon orbitals. A thermal reaction mechanism is thus suspected, which takes place on the ground state potential energy surface. A tunneling-electron induced reaction is not expected to proceed in a conrotatory manner. We will therefore investigate the reaction mechanism and possible reaction pathways for the ring-closure reaction.

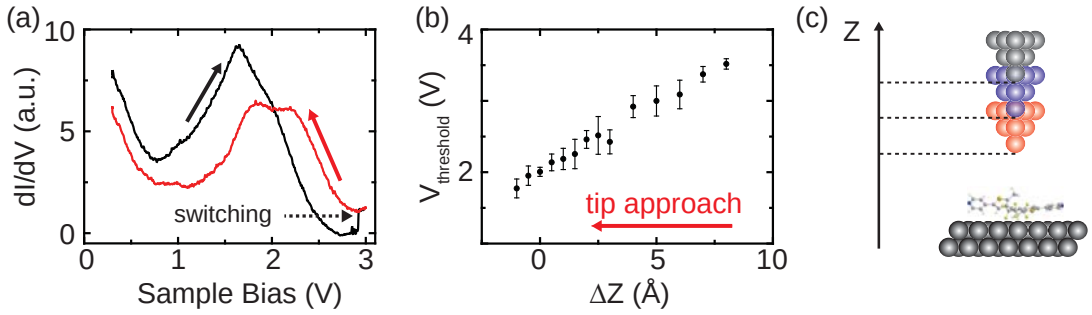

Figure 4.8: (a) Constant-current spectra at positive bias on a typical PDTE molecule. The black curve is the spectral signal when the bias voltage is increased. The switching event happens at almost 3 V, indicated by the black dashed arrow. The red curve corresponds to the spectrum after the switching of PDTE. (b) Threshold voltage for the switching as a function of the tip-sample distance relative to the point where the feedback is switched off. Feedback was disabled at V_{bias}=300 mV and I_{tunnel}=50 pA. (c) Illustration of the measurement at different sample-tip distances, shown by the differently colored tips. Figure adapted from [151].

4.4 Identification of the Switching Mechanism

Information about the involved processes and the manner in which the ring-closure reaction takes place can be provided by the threshold voltage of the switching process. We investigated the switching threshold for many PDTE molecules at the edges of molecular islands and in single as well as double rows. A typical constant-current $\mathrm{d}I/\mathrm{d}V$ spectrum at positive bias [Fig. 4.8(a)] shows the LUMO resonance before (black curve) the transformation. After the transformation, indicated by the black dashed arrow, the LUMO (red curve) is shifted. By means of this spectroscopic fingerprint and an increase in the apparent height in STM images at −1 V, we can identify the switched isomers. In some instances, not only the molecule directly below the tip is switched, but also other molecules in the vicinity. We focus our analysis on events when only the molecule below the tip is switched. Voltage ramps, equivalent to the one shown in Fig. 4.6(b), are applied to various molecules at different tip sample distances. The threshold voltages of the switching events are plotted as a function of the relative tip sample distance in Fig. 4.8(b). Here, zero relative distance corresponds to V_{bias}=300 mV and I_{tunnel}=50 pA, where the feedback loop was disabled. Negative relative distances indicate a tip approach. The error bars are obtained from the variation of the threshold voltages measured on different molecules.

In the data plot in Fig. 4.8(b), a linear increase of the threshold voltage with larger tip-sample distance is found. This behavior is an indication of an electric-field induced switching mechanism driving the reaction, which can be explained using the model of a parallel plate capacitor. The electric field $\boldsymbol{E}$ between the plates depends on their separation d and the applied voltage V as $\boldsymbol{E} = (V/d)\boldsymbol{e}_\mathrm{d}$. The vector $\boldsymbol{e}_\mathrm{d}$ is the unit vector along the direction of the electric field. When the distance d between the capacitor plates is reduced, a smaller voltage is required to produce the same electric field. However, we find a minimal threshold voltage of ≈1.5 eV to induce a reaction

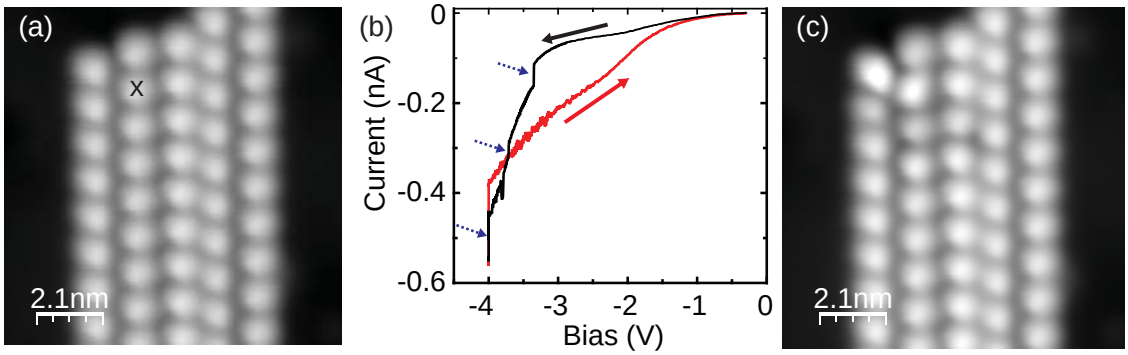

Figure 4.9: (a) Island of PDTE in the initial isomeric state. Scanning parameters are V_{bias}=−0.7 V and I_{tunnel}=100 pA. (b) Negative voltage pulse on the molecule marked by **x** in (a). Feedback opened at V_{bias}=−0.3 V and I_{tunnel}=50 pA with tip retracted by ΔZ=2 Å. (c) STM image of the PDTE island after the voltage pulse. Scanning parameters are V_{bias}=−0.7 V and I_{tunnel}=50 pA.

even at small tip-sample distances. This threshold is at the onset of the LUMO resonance. We therefore assume that the switching mechanism is a combination of an electric-field induced process and a tunneling-electron induced process.

Additionally, we checked for switching of PDTE at negative bias. In this case, no systematic behavior of the threshold voltage was observed. A change of the molecular structure is induced at negative bias at larger threshold voltages compared to positive bias. One example of a pulse at negative bias is given in Fig. 4.9, where the STM topography of a molecular island with all molecules in the initial state is shown in Fig. 4.9(a). A negative voltage pulse is applied to the molecule marked by an ×. The recorded tunneling current is shown in Fig. 4.9(b) and multiple abrupt changes are observed on the forward path (black curve), indicated by blue arrows. An STM topography recorded after the voltage pulse (Fig. 4.9(c)) reveals a change of the appearance of the target molecule as well as the surrounding molecules. In most cases, when a negative voltage pulse was applied, this simultaneous change of multiple molecules was observed. In addition to this, the LDOS of the switched isomer did not always exhibit the features observed when switched at positive bias. Voltage pulses at negative bias lead to a sudden increase in the tunneling current. This increase in the current could be explained by the presence of additional occupied states after the induced change. The steep increase of the tunneling current might trigger additional changes of the molecule. Therefore, a characterization of processes induced by negative voltage pulses is difficult.

Up to now we have identified the isomeric state of PDTE before and after the switching process. Distance-dependent measurements revealed a strong electric-field contribution to the switching mechanism at positive bias voltages, above the LUMO resonance. At this point, we note that a tip-induced back reaction of already switched PDTE could not be observed.

To understand the switching mechanism, the involved physical processes, and why a tip-induced back-reaction is inhibited, we turn to theoretical calculations. Some basic assumptions whether

the reaction takes places on the potential energy surface of the ground state or an excited state can be made by considering the magnitude of the tunneling current. The time scale between two tunneling events at a current of 200 pA is approximately 0.8 ns. Lifetimes of excited vibrational states are in the range of a few ps. The considerably shorter lifetime of the excited state ensures a thermal relaxation to the ground state between two tunneling events. Electronic excitations are equally short-lived, so we can assume that the switching takes place on the ground state potential energy surface. In terms of the Woodward-Hoffmann rules, the reaction in the ground state of the molecule corresponds to the thermal reaction pathway. However, according to the Menzel-Gomer-Redhead model [155, 156] and the Antoniewicz model [157], the molecule can gain kinetic energy from the excitation to a transient excited state, for example an ionic resonance. In that case, the potential energy surface of an excited state is such that the molecule starts to gains momentum. Since the lifetime is to short to complete the switching reaction, it relaxes back to the ground state. However, the molecule gained sufficient momentum in the excited state to overcome the reaction barrier in the ground state.

Based on the four different molecular models, three reactions are considered here. The ground state potential energy surfaces of the system have been calculated for these three reactions. Fig. 4.10(a) to (c) show the transition state geometries before the actual ring closure. The calculations of the reactions are based on the nudged elastic band (NEB) method. This method is used to find the minimum energy path (MEP) of a reaction for which the initial and final states are known. A set of transition state geometries is interpolated between the initial and final state. Then, the energy of these "assumed" transition states is minimized, which finally converges to the MEP. For PDTE, all considered reactions start from the initial o-flat isomer. They are as follows:

(a) erection of the molecule into the o-upright configuration,

(b) conrotatory ring closure into the c-*trans* isomer,

(c) disrotatory ring closure into the c-*cis* isomer.

An erection of the PDTE into the o-upright configuration does not involve a ring-closing reaction. The conrotatory and disrotatory reactions, on the other hand, involve the ring-closing reaction and result in the c-*trans* and c-*cis* configurations, respectively. The activation energies for these three processes are shown in Fig. 4.10(d)-(f). The green data points correspond to the case of no external electric field. The values of the forward and backward reaction barriers in the absence of an electric field are also displayed in Table 4.3. The lowest reaction barrier for the forward reaction is found for the erection into the o-upright isomer. However, due to the instability of the final state, the back reaction has an even lower activation energy, thus driving the thermal back reaction. The calculated reaction rate k=3.5 $\times$ $10^6\,s^{-1}$ (Table 4.3) indicates that the o-upright isomer instantaneously switches back.

In comparison to the erection of PDTE, the electrocyclic ring-closing reactions into the c-*trans* and c-*cis* isomers have a higher activation barrier. In the transition state geometry of the conrotatory reaction, one methyl group points towards the surface and thus poses a strong steric hindrance. On the other hand, the transition state geometry for the disrotatory reaction

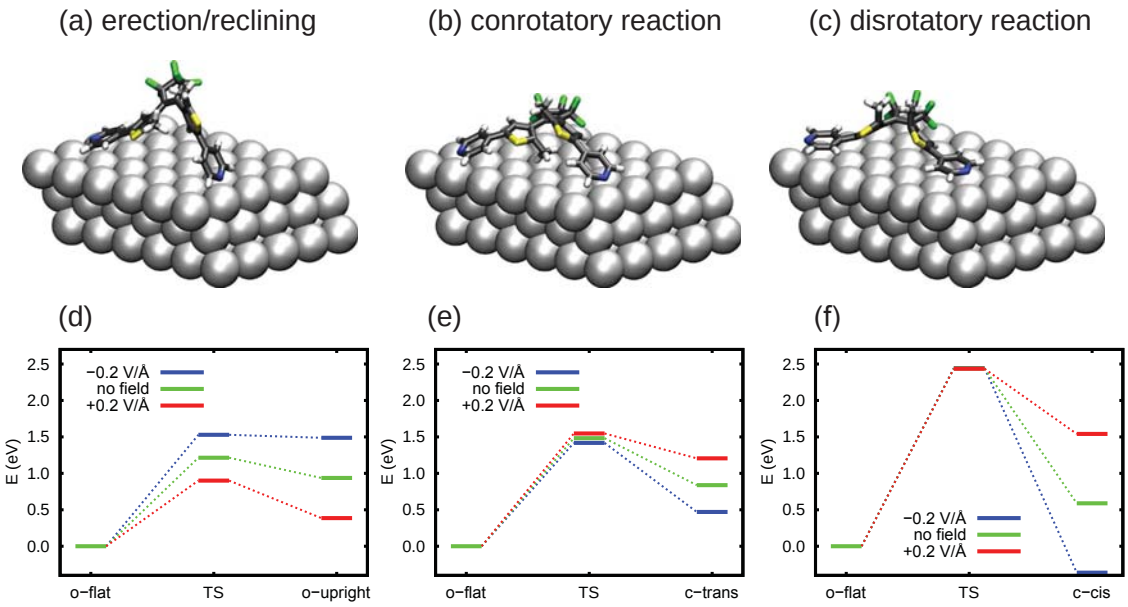

Figure 4.10: (a)-(c) Models of the three considered reaction mechanisms. (a) Erection of the molecule without ring-closure. (b) Conrotatory ring-closure reaction (thermal reaction product). (c) Disrotatory reaction (photo product). (d)-(f) Calculated energy barriers of the reactions in (a)-(c) with the transition state (TS). Three different electric fields are considered, positive electric field (red) corresponding to positive bias polarity and negative electric field (blue) corresponding to negative bias polarity. Figure adapted from [151].

requires a lifting of the molecular backbone away from the surface. Therefore a larger reaction barrier is obtained for the disrotatory reaction via the *cis* transition state. However, the final c-*cis* product is stabilized on the surface because of the close proximity of the molecular backbone to the surface. Therefore, the back reaction has an even larger barrier compared to the conrotatory reaction. The need to lift the molecular backbone away from the surface requires more energy for the c-*cis* isomer than for the c-*trans* isomer. As a result, the reaction rate for the thermal back reaction from the c-*cis* isomer at a temperature of 300 K is $1.1 \times 10^{-19}\,\mathrm{s}^{-1}$. With this rate, we do not expect a back reaction to take place within the time scale of the experiment. A suppression of the back reaction concurs with the irreversibility of the tip-induced switching and supports the assignment of the c-*cis* product as final result of the switching reaction.

On the Ag(111) surface, the lower activation barrier for the conrotatory reaction in comparison to the barrier for the disrotatory reaction contradicts the behavior expected from the Woodward-Hoffmann rules. They predict the thermal reaction (on the ground state potential energy surface) to proceed in a disrotatory manner. It is not unrealistic that the Woodward-Hoffmann rules do not fully apply to reactions of molecules on surfaces due to steric restrictions and the substrate-induced change of the potential energy landscape and the thermodynamic stabilities.

Table 4.3: Activation energies $\Delta E^{\ddagger}$ and rate constants k (at 300 K) for possible thermal forward/back reactions from/to the open flat form.

process	direction	$\Delta E^{\ddagger}$/eV	k/s^{-1}
erection/reclining	forward	1.21	3.5×10^{-9}
	back	0.28	3.5×10^{6}
conrotatory reaction	forward	1.48	2.1×10^{-13}
	back	0.64	6.2×10^{1}
disrotatory reaction	forward	2.44	3.5×10^{-31}
	back	1.85	1.1×10^{-19}

The distance dependence of the threshold voltage found in Fig. 4.8(b) can be understood by considering the effect of an external electric field on the ground state potential energy surface. A simple point charge approach was used to model the electrostatic interaction. The model consists of a parallel-plate capacitor, which is constituted by the tip and the surface. The situation is depicted in Fig. 4.11 with the electric field between positive and negative charges (red and blue). The energy correction due to the electrostatic interaction between the electric field and the permanent dipole moment produced by a charged adsorbate (charge Q, distance d_z) and its image charge in the substrate (with charge -Q and distance d_z) amounts to

$$V_{el} = -2 d_z Q E_z \quad . \tag{4.1}$$

Here, the electric field strength is E_z. Table 4.4 compiles the electric charge Q accumulated on the adsorbate, the adsorbate-substrate distance as well as the absolute and relative (to the o-flat isomer) energy shifts of the transition state and final state structures for an electric field of E_z=0.2 V/Å. The accumulated charge on the adsorbate is relatively small. The o-upright conformation is positively charged due to a weak covalent bond of the pyridine nitrogen atoms to Ag, which has an electron donating character. The electrocyclic products, on the other hand, accept negative charge from the substrate. The absolute charge accumulation is related to the distance of the adsorbate from the surface and is higher for adsorbates closer to the surface. In the c-*cis* isomer, the molecular backbone nestles up against the surface, hence it has the largest negative charge.

The energy change of the stationary states is also visualized in Fig. 4.10(d)-(f), where red data points represent results in a positive electric field and blue points in a negative electric field. One key observation is the insignificant shift of the ground state potential energies of the transition states for the electrocyclic reactions. Nevertheless, the final states are stabilized in a negative electric field and destabilized in a positive electric field, opposed to the experimental observations for the switching behavior. This effect is strongest for the disrotatory product, probably because the c-*cis* isomer is subject to strong dispersion interaction and has a large dipole moment, which is counteracted by the electric field.

A significant dependence of the activation barrier is only found for the erection into the o-upright isomer, which is lower in a positive electric field compared to negative fields. This behavior is

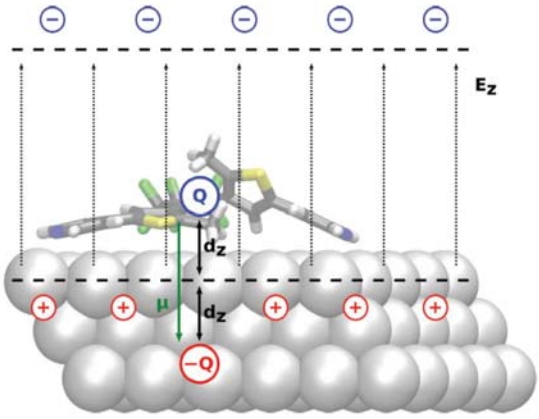

Figure 4.11: Model of the electric field imposed by a plane-parallel capacitor represented by the tip (blue charges) and the surface (red charges). The correction of the electric field changes the charge in the molecule Q and the induced image charge in the substrate -Q. Figure reprinted from [158].

Table 4.4: Total molecular charges Q and vertical positions d_z of the respective center of charge entering (Eq. (4.1)); absolute level shifts V_{el} and level shifts with respect to the shifted energy of the o-flat isomer $\Delta V_{\mathrm{el}} = V_{\mathrm{el}} - V_{\mathrm{el,o-flat}}$ (see also Figure 4.10) under the influence of a homogenous electric field with $E = +0.2$ V/Å.

	o-flat	erection TS	o-upright	conrotatory TS	c-*trans*	disrotatory TS	c-*cis*
Q/e	−0.16	+0.03	+0.11	−0.20	−0.40	−0.16	−0.88
d_z/Å	3.59	6.11	7.29	3.76	3.77	3.55	3.37
V_{el}/eV	+0.24	−0.08	−0.31	+0.30	+0.60	+0.23	+1.19
ΔV_{el}/eV	0.00	−0.31	−0.55	+0.06	+0.37	±0.00	+0.95

in agreement with the experimental observations of a higher energy required at larger tip-sample distances, *i.e.* , weaker electric fields (compare also to Fig. 4.8(c)). The strong field dependence originates from a large dipole moment of the o-upright transition state, due to a larger distance from the substrate, combined with a positive charge on the adsorbate.

Combining the findings for the electric field-dependence of the ground state potential energies in the different stages of the switching process with the thermodynamic stabilities and the assignments of the initial and final isomers, we can draw a picture for the reaction mechanism. In fact, the erection of the open isomer from the flat lying configuration into the upright position can be imagined as a first step of the switching reaction. The ring-closing reaction might happen in this configuration, whereafter the adsorbate reapproaches the substrate in a conjugated cyclic configuration with high adsorption energy. In that case, the activation of the reaction does not require the transition state geometry for the disrotatory cyclization, which solves the discrepancy of the high activation barrier for this pathway.

4.5 Summary and Conclusions

In this chapter we studied the adsorption behavior and tip-induced switching of diarylethene compounds on a Ag(111) substrate. The results of scanning tunneling microscopy and spectroscopy experiments were complemented by DFT calculations. We found that the open isomer of PDTE adsorbed on a Ag sample forms ordered molecular islands. Combining measurements of the electronic structure and calculations of the PDOS showed that the molecule retains its open form upon adsorption.

Tip-induced voltage pulses were used to transform individual PDTE molecules in a controlled way. The transformation could be assigned to the ring closure of single PDTE into the *cis* configuration, which has both methyl groups at the central hexatriene units pointing in the same direction. A combination of a tunneling-electron and electric-field induced mechanism was found to be involved in the switching. Interestingly, this form was not expected according to the Woodward-Hoffmann rules. These observations suggest a step-wise switching process consisting of an electric-field assisted erection of the open flat-lying PDTE into an upright position, where the disrotatory electrocyclic ring closure takes place. The entire reaction is assumed to take place on the ground state potential energy surface of the molecule. Our findings emphasize the influence of the coupling of the adsorbate to an underlying metallic substrate on the switching behavior as well as adsorption configurations. Cyclization of these photochromic switches with the STM tip is the first step to a local control of the switching and thus for the integration into electronic devices. Different molecular end groups may lead to a decoupling of the switching unit from the substrate, which could restore the reversibility of the switching. If the control of these systems is enhanced, these molecules might have several technical applications in nano fuses or current bypasses, where the molecule is switched into the closed state with a considerably larger conductance and thus drains excess currents from sensitive components.

Further experiments can be performed, combined with atomic force microscopy (AFM) measurements to resolve the internal structure of the adsorbates in both isomeric states. To get a more detailed idea on the exact steps of the switching event, theoretical calculations for the electrocyclization in the upright configuration may elucidate the true nature of the process.

Chapter 5

Magnetic Anisotropy in Shiba Bound States

The results presented in this chapter have been published as:

- *"Magnetic anisotropy in Shiba bound states across a quantum phase transition"* by N. Hatter, B. W. Heinrich, M. Ruby, J. I. Pascual and K. J. Franke, *Nature Communications* **6:8988** (2015)

5.1 Introduction

On the atomic scale, the presence of a magnetic moment on a superconductor induces localized states inside the superconducting energy gap, so-called Yu-Shiba-Rusinov (Shiba) states [44–46] that were introduced in section 3.4. Shiba states open a precise way to characterize the interaction of magnetic adsorbates with superconductors. The immediate environment of the spin influences this interaction. Therefore, Shiba states can be used to understand the role of the local environment on the exchange interaction J of an impurity spin with a superconductor.

A single unpaired spin ($S = 1/2$) can give rise to one pair of Shiba states [49], which is spatially localized in the vicinity of the magnetic impurity [113, 116]. If many impurities are brought close to each other, Shiba states may hybridize and form Shiba bands, which are delocalized across the entire array of impurities. Furthermore, in systems with individual magnetic adsorbates on superconductors, multiple Shiba states are present [50, 159]. Hybridization of multiple states will lead to a more complex band structure. Current research aims at understanding the nature of multiple Shiba states and how to control their properties. Different origins of multiple Shiba states are under discussion. They range from different angular momentum scattering channels [113, 160, 161] over individual d orbitals, acting as separate scattering potentials [162], to low-energy excitations due to magnetic anisotropy or vibrations [163–165]. Experimentally, the origin of multiple Shiba states is often difficult to determine [50, 118].

Another effect that arises from exchange coupling between the magnetic adsorbate and the substrate is the formation of a Kondo singlet [38]. In a superconductor, Kondo screening can be observed along with the presence of Shiba states [51, 52, 119, 164]. As explained in chapter 3.4, the Kondo energy scale $k_\mathrm{B}T_\mathrm{K}$, which characterizes the exchange coupling strength in the normal state,

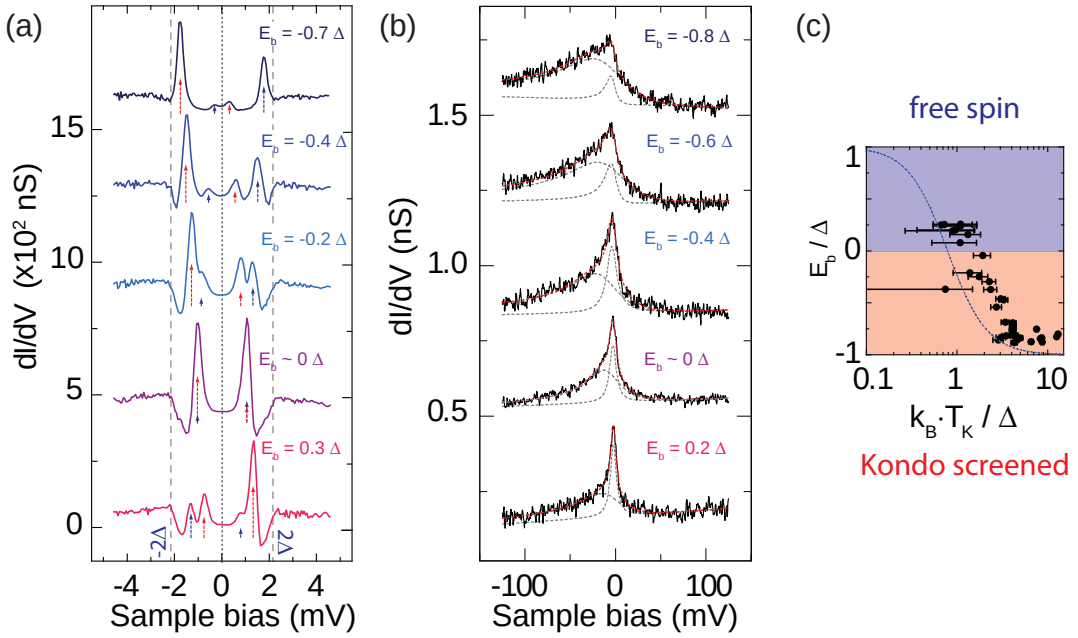

Figure 5.1: (a) Subgap spectra on different MnPc molecules within an island. One pair of Shiba states is found with binding energies varying for each molecule. Shiba state energies are denoted E_b. (b) Kondo resonances measured at 8.8 K on MnPc. Two Fano lineshapes are fitted. The narrow Fano lineshape width decreases for MnPc with increasing Shiba state energy. (c) Correlation of Shiba state energy with the Kondo temperature of the narrow resonance. Experimental data confirm the theoretical predictions of [119], shown as blue dashed line. Figure adapted from [51].

competes with the energy scale of the superconducting pairing, Δ. In the "Kondo screened" case, $k_\mathrm{B}T_\mathrm{K} \gg \Delta$, the spin of the impurity is completely screened due to processes involving normal state electrons. For a weaker exchange coupling, the Kondo screening is reduced. When the superconducting gap exceeds the Kondo screening, $k_\mathrm{B}T_\mathrm{K} \ll \Delta$, the impurity spin is not screened. A Shiba state deep inside the superconducting gap is the fingerprint of an exchange interaction in the regime $k_\mathrm{B}T_\mathrm{K} \sim \Delta$ [119]. A quantum phase transition from the "Kondo screened" state with $S = 0$ to the "free spin" state on the superconductor with $S > 0$ occurs when the Shiba state crosses the Fermi level. This transition occurs at $k_\mathrm{B}T_\mathrm{K} \sim 0.3\Delta$ and has been described theoretically [52, 117, 119] and detected experimentally [51, 122, 123].

In an earlier work, Franke and coworkers investigated manganese phthalocyanine (MnPc) on the type I superconductor Pb(111) [51]. The incommensurability of the square-like MnPc islands with the hexagonal substrate creates a Moiré-like pattern which provides many different adsorption sites on the substrate. This leads to a variation in the adsorbate-substrate interaction and enables the study of a large range of magnetic exchange coupling strengths. At 4.8 K, one pair of Shiba states is present whose binding energy varies with the adsorption site of MnPc. Subgap spectra from [51] are shown in Fig. 5.1(a). The same molecules were measured at 8.8 K, when the

superconductivity is suppressed. The spectra exhibit a Kondo resonance on a larger energy scale [Fig. 5.1(b)]. Fits of two Fano lineshapes to the experimental data revealed a decrease of the Kondo temperature of the narrow resonance with increasing Shiba state energies. By correlating the Shiba state energy with the Kondo temperature, shown in Fig. 5.1(c), the theoretically predicted quantum phase transition between the "Kondo screened" and "free spin" ground state [119] (blue dashed line) was verified.

MnPc in gas phase has a spin state of $S = 3/2$ and retains a finite magnetic moment on metal substrates [166–168]. In systems with a spin $S \geq 1$, such as MnPc, one might expect the presence of multiple Shiba states inside the gap. Žitko and co-workers [164] argue that such systems may involve multiple Kondo screening channels with different coupling strengths J_k. Each Kondo screening channel induces Shiba states. Furthermore, a splitting of the Shiba states due to magnetic anisotropy induced by the organic phthalocyanine ligand is a likely consequence.

In this chapter, we turn our attention again to MnPc on Pb(111) and probe the subgap peak structure at lower temperature to obtain a better spectral resolution. Potentially, a splitting of Shiba states due to magnetic anisotropy could have been hidden by a broadening of the Shiba states at 4.8 K. A detection of multiple Shiba states can help to gain further insight into the role of the organic ligand on the spin state and the magnetic anisotropy introduced in the system.

5.2 Tunneling Spectroscopy with a Superconducting Tip

Pb becomes superconducting below a critical temperature of 7.2 K. We investigate the MnPc on Pb(111) at 1.2 K. The superconducting gap parameter at this temperature is Δ_{Pb}=1.35 meV. When probing the superconducting gap with a normal metal tip, spectral features are broadened according to Fermi-Dirac statistics, resulting in a width of $\Gamma_{\mathrm{FD}} \approx 3.5 k_{\mathrm{B}}\mathrm{T}$. Thus at 1.2 K, the lower limit of the spectral resolution is ≈330 μeV. Multiple localized states inside the superconducting gap are difficult to resolve with a metal tip.

To improve the energy resolution in STS, we used tips covered with a thick layer of Pb, such that they become superconducting as well. To obtain a Pb layer on the tip, we indented the chemically-etched tungsten tip into the clean superconducting surface while applying 100 V tip bias until a Pb covered, superconducting tip was obtained. Due to this procedure, the tip exhibits the known density of states of a BCS superconductor with the sharp quasiparticle peaks at the edges of the superconducting gap. Tunneling spectroscopy results in a convolution of the DOS of the tip and the sample.

An illustration of the sample and tip DOS is shown in Fig. 5.2. At a finite bias voltage of -(Δ_{tip} + Δ_{sample}), as depicted in Fig. 5.2(a), electron-like quasiparticles from the sample can tunnel into hole-like quasiparticle states in the tip. Due to the large peak-like density of states in both electrodes, an intense narrow peak appears in the tunnel spectrum in Fig. 5.2(c). With increasing bias, no tunneling is possible because of the absence of states in the superconducting gap. The tunneling current quickly drops to zero, which leads to very steep decrease of the signal in the differential conductance. This region of zero conductance marks the superconducting gap. At zero sample bias, electron-like (hole-like) quasiparticle states are aligned in both electrodes [Fig. 5.2(b)]. The spectral signal increases only at eV=($\Delta_{\mathrm{tip}} + \Delta_{\mathrm{sample}}$) when the DOS alignment in both electrodes is opposite to the initial situation in Fig. 5.2(a). This convolution results in a

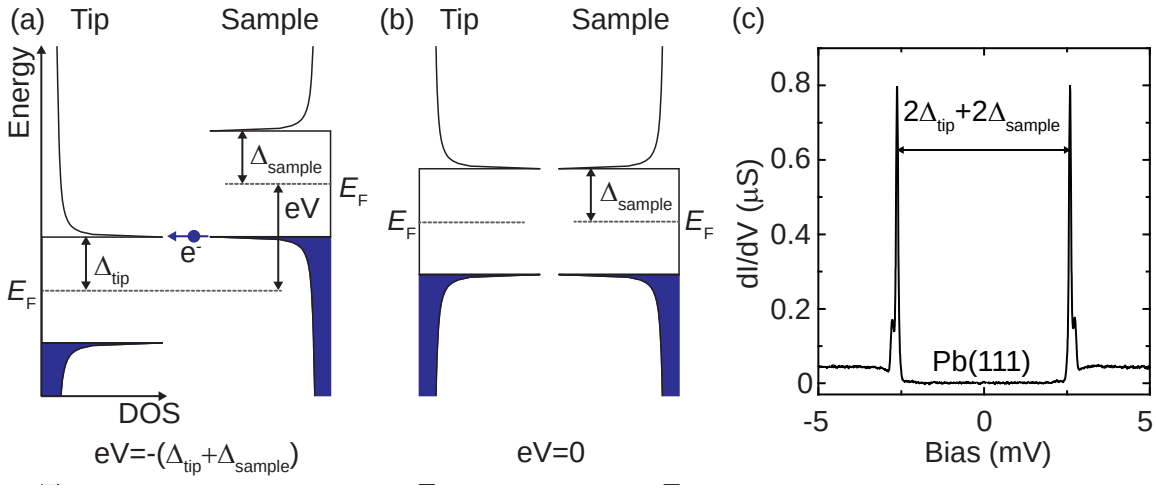

Figure 5.2: Illustration of the tunneling mechanism in a superconductor-insulator-superconductor (SIS) junction. (a) At a bias voltage eV=$\Delta_{\mathrm{tip}} + \Delta_{\mathrm{sample}}$ electron-like quasiparticles (blue colored area) from the continuum of the sample can tunnel (blue dashed arrow and solid circle) to the hole-like quasiparticle states (blank area) in the tip. Due to the sharp peaks in the DOS, the spectrum exhibits narrow peaks at |eV|=$\Delta_{\mathrm{tip}} + \Delta_{\mathrm{sample}}$. (b) At eV=0, no tunneling is allowed as electron-like states and hole-like states in the sample and tip are aligned to each other.

dI/dV spectrum of the form shown in Fig. 5.2(c), which was measured on the pristine Pb surface.

In the same way, Shiba states inside the superconducting gap can be resolved. Fig. 5.3(a) depicts the situation at a sample bias of -($\Delta + E_{\mathrm{b}}$). The hole-like BCS quasiparticle resonance of the tip (white area) is aligned with the electron component of the Shiba state in the sample (blue area). Electrons can tunnel from the Shiba state in the sample to the tip, and a sharp Shiba state appears in the dI/dV-signal. Thus, the Shiba states in the dI/dV spectrum do not appear at their respective bound energies but at energies shifted by the superconducting gap parameter of the tip.

Thermal effects still play a role, as the quasiparticles can be excited into the hole-like component of a Shiba state. This effect is illustrated by the blue (white) parts in the hole-like (electron-like) part of the Shiba states in Fig. 5.3. Then, even at a bias voltage -($\Delta - E_{\mathrm{b}}$), quasiparticles can tunnel from the sample into the tip [Fig. 5.3(b)] and lead to a small resonance in the dI/dV spectrum. At temperatures as low as 1.2 K, thermal excitations only play a role when Shiba states are close to E_{F}. The energy range in which thermal excitations are significant is determined by the width of the Fermi-Dirac distribution, which describes the thermal energy of the system. If the Shiba state is far away from E_{F}, as in Fig. 5.3(c), thermal excitations are negligible, thus no thermally excited Shiba states are observed.

By using a superconducting tip, we obtain an energy resolution better than 45 μeV [169], which is well below the Fermi-Dirac broadening. dI/dV spectra obtained with a superconducting tip are a convolution of the sample DOS and the tip DOS. Therefore, the superconducting gap in

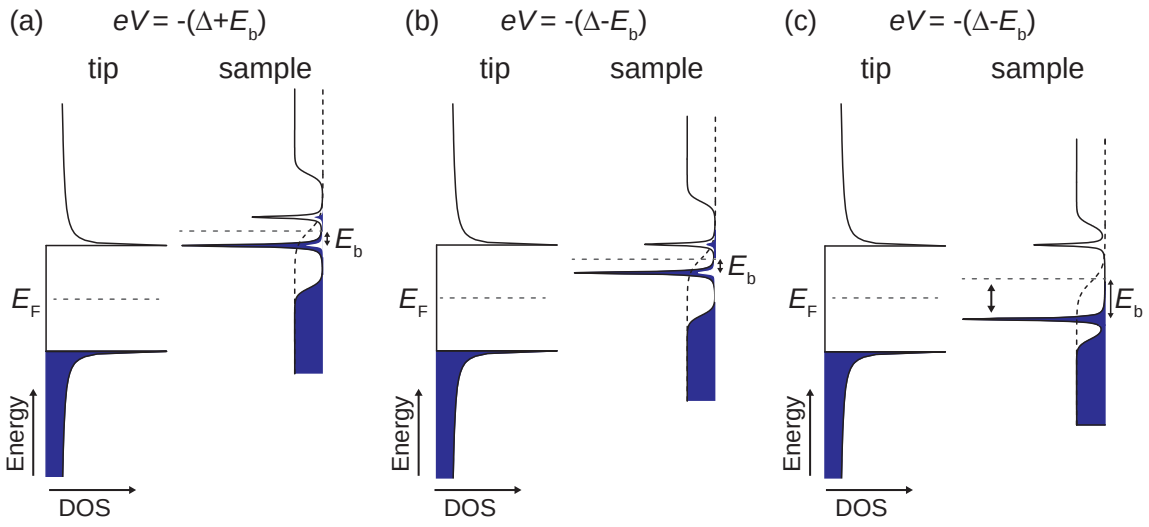

Figure 5.3: Tunneling processes at negative bias voltage: (a) At $eV = -(\Delta + E_\mathrm{b})$ the alignment between the electron-like Shiba state and the hole-like BCS peak marks the onset of tunneling. (b) A thermally occupied Shiba state leads to tunneling at $eV = -(\Delta - E_\mathrm{b})$. (c) If the Shiba state is located far away from E_F, thermally assisted tunneling at $eV = -(\Delta - E_\mathrm{b})$ is strongly minimized and not observed at 1.2 K.

the spectrum in Fig. 5.2(c) has a size of 4Δ instead of 2Δ and Shiba states at energies shifted by the tip gap. In order to extract the spectroscopic signal of the sample, we employ a numerical deconvolution routine as described in appendix I.

5.3 Observation of Multiple Shiba States on MnPc on Pb(111)

The Pb(111) single crystal surface was cleaned by repeated cycles of Ne^+ sputtering and annealing to 430 K. We evaporated manganese phthalocyanine (MnPc) molecules from a Knudsen cell held at 673 K onto the clean surface kept at room temperature. Subsequently, the sample was transferred into the precooled STM. For all measurements on MnPc on Pb(111) the temperature inside the STM was at 1.2 K.

After deposition of MnPc, the molecules arrange in self-assembled, densely-packed monolayer islands. A part of a molecular island with MnPc molecules is shown in Fig. 5.4(a). The molecules appear clover-shaped with four lobes around a central protrusion, which corresponds to the Mn ion. This appearance indicates a flat adsorption configuration of MnPc, in agreement with previous measurements [51, 166]. The molecular adlayer assumes a nearly square lattice with a nearest-neighbor distance of approximately 1.32 nm [170]. Due to the lattice mismatch with the underlying hexagonal substrate, it accommodates many different adsorption sites of the Mn core on the hexagonal Pb lattice. Consequently, a Moiré-like pattern evolves, which involves variations in the electronic and magnetic coupling strength between adsorbate and substrate [51, 166].

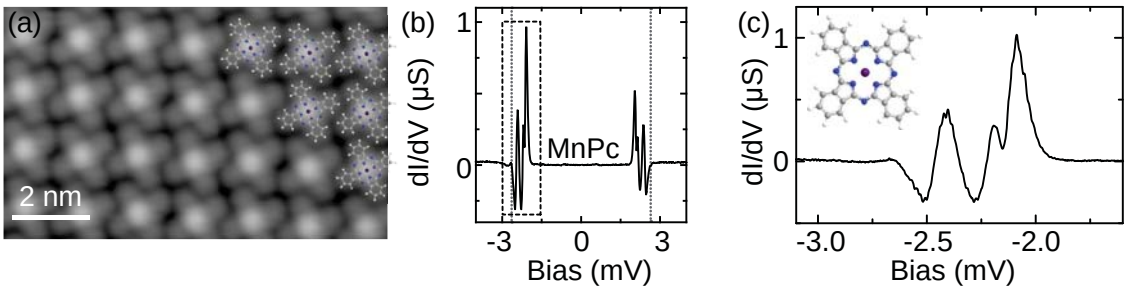

Figure 5.4: (a) STM topography of a MnPc monolayer island on Pb(111). Scanning parameters are V_{bias}=50 mV and I_{tunnel}=200 pA. (b) dI/dV spectrum recorded in the center of a representative MnPc molecule inside a molecular island (Feedback opened at: V_{bias}=5 mV, I_{tunnel}=200 pA). (c) Zoom on the subgap excitations below E_F in the MnPc spectrum shown in (b). The inset shows a structural model of MnPc. Figure adapted from [124].

To reveal fingerprints of magnetic interaction of MnPc with the superconducting substrate, we probe the density of states in a small energy range around E_F. dI/dV spectra were recorded under open-feedback conditions using the introduced lock-in technique with a bias modulation of 15μV_{rms} at an oscillation frequency of 912 Hz.

As shown in the exemplary spectrum in Fig. 5.4(b), MnPc molecules exhibit Shiba states inside the superconducting gap. In contrast to the measurements at 4.5 K, we observe two pairs of Shiba triplets inside the superconducting energy gap at 1.2 K. Similar to single Shiba states, they are symmetric in energy around E_F, but asymmetric in intensity. In the limit of small tunneling rates, as fulfilled in the present experiment, the dI/dV signal is an expression of the different electron and hole components of the Shiba wave functions [118]. The different weights arise from the particle-hole asymmetry in the normal state and an on-site Coulomb potential at the scattering site [52, 113, 116]. Fig. 5.4(b) depicts the spectrum of a MnPc molecule exhibiting Shiba states with higher intensity at negative energy, thus the electron-like components.

Along with the formation of Shiba states inside the superconducting gap, the BCS coherence peaks disappear. In Fig. 5.4(b), the gray dotted lines indicate the edges of the superconducting gap where the BCS quasiparticle peaks occur on pristine Pb(111). The intensity of the Shiba states decreases at larger distances from the Mn centers and the normal BCS quasiparticle resonances are recovered. Far away from any molecules, the well-known Pb spectrum, as shown in Fig. 5.2(c), is obtained.

A magnified view on the Shiba triplet at negative energies is provided in Fig. 5.4(c). The triplets can be clearly resolved and consist of very sharp peaks with full widths at half maximum ranging from 50 to 100 μeV. They are separated by up to 400 μeV. Even though the spectral resolution is better than the Fermi-Dirac broadening, lifetime effects play a role at finite temperatures. These cause a broadening of the superconducting coherence peaks and subgap states. At 4.8 K, the triplet peaks are greatly broadened and overlap with each other, thus only a single peak is detected in measurements by Franke *et al.* [51].

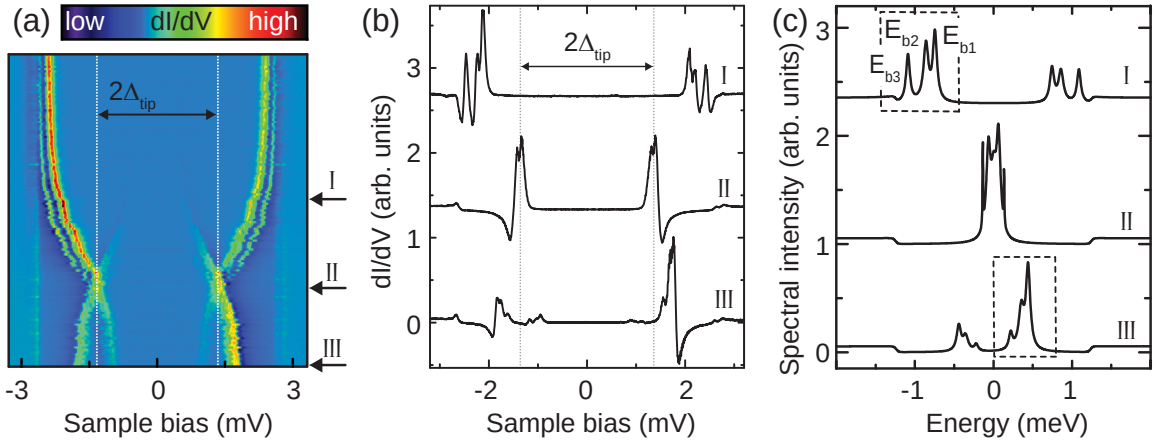

Figure 5.5: (a) 2D color plot of dI/dV spectra of 137 different MnPc molecules inside a molecular island. The spectra are ordered by the energy of the most intense Shiba resonance, increasing from top to bottom (feedback opened at: V_{bias}=5 mV, I_{tunnel}=200 pA). (b) dI/dV spectra of three respective MnPc molecules with bound state energies in three different coupling regimes. (c) Spectral intensity obtained by deconvolution of the spectra shown in (b). The bound state resonances are labeled E_{b1}, E_{b2}, and E_{b3}, respectively. Figure adapted from [124].

5.4 Evolution of Shiba States throughout the Quantum Phase Transition

To study the evolution of the Shiba triplet for varying exchange coupling strength, we make use of the different adsorption sites of MnPc on Pb(111) inside molecular islands. Fig. 5.5(a) provides a false color map of dI/dV spectra obtained on more than 130 MnPc molecules. To better understand this map, three exemplary dI/dV spectra are shown in Fig. 5.5(b), taken from characteristic points in the map. The color scale in Fig. 5.5(a) represents the spectral intensity: red corresponds to high intensity and blue to low intensity, respectively. Each horizontal line in the plot corresponds to one dI/dV spectrum. All spectra are ordered with increasing Shiba state energy from top to bottom. In the topmost spectrum, the Shiba state energy is at negative energies and almost merges with the superconducting gap edge while it is positive in the lowest spectrum. This ordering emphasizes the previously detected quantum phase transition in which the Shiba state crosses the Fermi level at the point of the quantum phase transition [51]. It is worthy to note again that due to the convolution of sample DOS and tip DOS, the position of the Shiba states in the spectra is shifted by the superconducting gap parameter of the tip (Δ_{tip}). Thus, the point of the phase transition corresponds to Shiba states at $\pm\Delta_{tip}$ in the color plot.

Spectrum I in Fig. 5.5(b) is an example of a MnPc molecule with a larger intensity at negative energy, when tunneling occurs into occupied states. The energetic position of the triplet with higher intensity corresponds to the binding energy E_b of the Shiba states [51, 52, 119]. This implies that spectrum I belongs to a MnPc, which is in the “Kondo screened“ ground state. On

the other hand, spectrum III has a higher intensity for the Shiba triplet above E_{F}. It is an example of a molecule in the "free spin" ground state. The order of the spectra from top to bottom thus indicates a transition from the "Kondo screened" to the "free spin" ground state, which goes hand in hand with a decreasing exchange coupling strength J. One key observation is the collective shift of the triplet of Shiba states through the superconducting gap. As will be discussed later, in the case of independent scattering of spins in different d orbitals, a similar shift of all $E_{\mathrm{b}i}$ is not expected, because d orbitals have different spatial distributions and hence hybridize differently with the substrate. Due to this reason, one would not expect the Shiba states to have similar energies. Taking into account these arguments, scattering at different d orbitals can be excluded as origin of these multiple Shiba states.

While Shiba states in the $\mathrm{d}I/\mathrm{d}V$ spectra are located at energies in the intervals $-2\Delta/e < V_{\mathrm{bias}} < -\Delta/e$ and $\Delta/e < V_{\mathrm{bias}} < 2\Delta/e$, MnPc molecules with Shiba states close to the Fermi level exhibit additional resonances at energies in the interval $[-\Delta_{\mathrm{tip}}/e, \Delta_{\mathrm{tip}}/e]$ (spectrum II and vicinity in Fig. 5.5(a)). These states result from tunneling into thermally excited Shiba states, as explained in section 5.2. In spectrum II in Fig. 5.5(b), Shiba states overlap with their thermal Shiba states.

A quantitative analysis of the Shiba state intensities can provide information about the origin of the observed splitting into multiple resonances. To this end, we numerically deconvolve the $\mathrm{d}I/\mathrm{d}V$ spectra. The deconvolution is done by a fit of a convolved tip DOS and sample DOS to the experimental data. The details are explained in appendix I. In the following, we will retrieve the spectral intensity related to the sample DOS and investigate the intensities of the Shiba states.

5.5 Shiba Intensities as a Fingerprint of the Quantum Phase Transition

Fig. 5.5(c) shows the deconvolved signal of the three exemplary spectra shown in Fig. 5.5(b). From the numerical deconvolution, we directly obtain the Shiba state intensities within the triplets. Fig. 5.6(a) features a close-up view on the deconvolved signal of a molecule with Shiba states at negative binding energy. The three Shiba states are modeled as Lorentzians and colored black, red and blue, from the outermost to the innermost peak, respectively. Analogously, Fig. 5.6(c) shows the deconvolved spectral signal of spectrum III in Fig. 5.5(b). The Shiba state intensity corresponds to the area of the Lorentzians. The relative Shiba intensities of all MnPc molecules are plotted as a function of the Shiba state energy in Fig. 5.6(b). We find a distinct change in the relative peak intensities within the triplets at the point of the quantum phase transition. In the "Kondo screened" regime (negative energies), the relative peak areas $A_i/\Sigma_{j=1}^{3} A_j$ of the Shiba states within the triplets are close to 1/3. For molecules with Shiba states close to the gap edge (points at the far left), the relative intensities seem to deviate slightly from 1/3. It is probably an artifact in the deconvolution routing, which arises due to the proximity of the outermost Shiba state to the step-like superconducting gap edge. In the deconvolution procedure, the overlap of the Shiba state with the gap yields lower relative intensities. We exclude a physical effect of this deviation. In contrast to the relative Shiba state intensities in the "Kondo screened" ground state, in the "free spin" ground state (positive energies) the relative areas are considerably

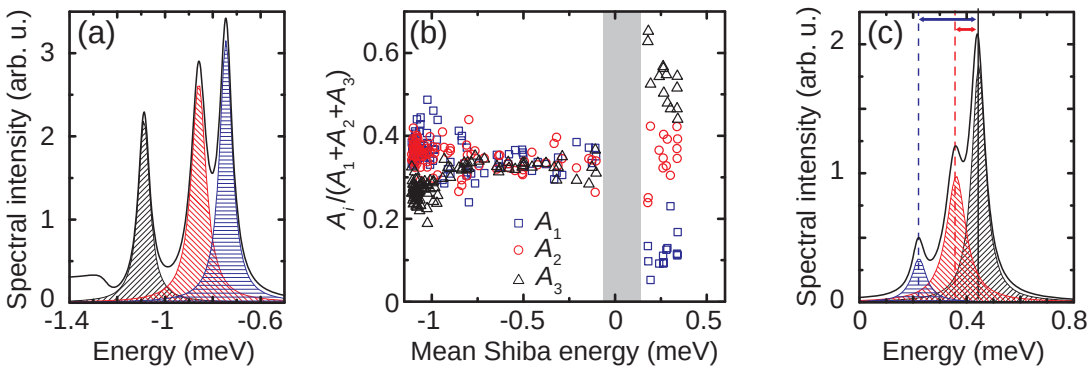

Figure 5.6: Shiba state analysis: (a) Zoom on the framed part of the deconvolved spectrum I in Fig. 5.5 (c). We model the spectrum with three Lorentzian peaks of different width (shaded in blue, red, and gray) and a broadened step function at the gap edge (see appendix I). (b) Peak areas relative to the sum of all three subgap peaks ($A_i/\sum_{i=1}^{3} A_i$) plotted vs. the mean energy ($E_{\mathrm{b}i}/\sum_{i=1}^{3} E_{\mathrm{b}i}$) of the respective set of subgap peaks. (c) As (a), but on spectrum III in Fig. 5.5(c). Figure adapted from [124].

different [Fig. 5.6(b) and (c)]. Here, the relative area of the subgap excitations decreases from the outermost peak, $E_{\mathrm{b}3}$, to the innermost peak, $E_{\mathrm{b}1}$. Spectra close to the Fermi level (gray shaded area) are omitted in the data plot due to the overlap with their thermal Shiba states, which makes it impossible to disentangle the different contributions.

One approach to explain the occurrence of multiple Shiba states and their different intensities is based on the theory about different angular momentum scattering channels [50, 113, 160, 161, 165]. The wave function of the scattering quasiparticles can be separated into partial waves with different angular momentum numbers. Each angular momentum channel causes one Shiba state. Bound states, which originate from higher angular momentum scattering channels ($l = 1, 2, etc.$), always reside close to the superconducting gap edge. At the same time, the $l = 0$ channel may shift through the superconducting energy gap, depending on J [113, 165]. Moreover, the intensity of higher angular momentum channels is larger compared to low indexes. This possibility is in contrast to the collective shift of the Shiba triplet and also the behavior of the Shiba state intensities. We therefore exclude this possibility as explanation for multiple Shiba states in MnPc on Pb(111).

Bound state excitations coupled to other low-energy excitations, such as spin excitations or vibrations [163, 164] are more suited to explain a collective shift of Shiba triplets. In this scenario, additional resonances would appear as satellite peaks at higher absolute energy for both ground states. Their spectral weight should scale with the electron-phonon coupling strength. Hence, their intensities are expected to be substantially lower than the weight of the main resonance at $\pm E_{\mathrm{b}}$, which is the innermost Shiba state [163]. This is clearly not the case in our data.

Supported by the characteristic change in the relative peak areas at the point of the quantum phase transition, a magnetocrystalline origin of the Shiba state splitting as predicted by Žitko and co-workers [164] for $S \geq 1$ systems rather explains our findings.

5.6 Magnetic Anisotropy as Origin of the Shiba State Splitting

To conclude on the physical model for the description of multiple subgap resonances and the different relative intensities in the two regimes, we have a closer look at the spin state of the MnPc molecule on the Pb surface. The MnPc molecule carries a spin $S = 3/2$ in gas phase [171]. Including the organic ligand in calculations, strong hybridization of the spin in the $d_{\mathrm{xz,yz}}$ with ligand orbitals drives the formation of a singlet. This reduces the effective spin interacting with the substrate's quasiparticles to $S = 1$ [172]. Due to the spatial distribution, the unpaired spin in the d_{z^2} orbital is subject to strong coupling with the electronic states of the substrate, leading to sizable Kondo screening. Knowing these facts, we attribute the d_{z^2} orbital to be the exclusive scattering channel responsible for the occurrence of the Shiba states. We label this scattering channel as $k = 1$. The diversity of adsorption sites explains the different coupling strengths and therefore the different energies of the Shiba states.

In contrast, the spin in the d_{xy} orbital is not expected to show a significant coupling to the substrate [168, 172, 173]. The unpaired spin in the d_{xy} orbital should then not give rise to an observable Shiba state, due to the lack of interaction with the substrate [172]. It therefore does not provide a direct scattering channel for tunnel electrons. However, this channel $k = 2$ can couple to the spin in the d_{z^2} orbital, thus forming the total spin state of $S = 1$. A breaking of spherical symmetry of the Mn orbitals by the organic ligand and the adsorption on a substrate leads to a splitting of the former degenerate m_{S} levels due to magnetic anisotropy [69, 174]. For a system with spin 1 in the presence of axial and transverse anisotropy, the spin Hamiltonian approach (see section 3.1.2) splits the former degenerate spin projections. The new set of eigenstates consists of three states, $|0\rangle$, $|+\rangle$, and $|-\rangle$, where the latter two are linear combinations of the former eigenstates with $m_{\mathrm{S}} = 1$ and $m_{\mathrm{S}} = -1$ [174].

Shiba states are an excitation of the superconductor-impurity system by attachment or removal of a quasiparticle. This induces a change of the total spin by 1/2. We can describe the whole set of spectra in both ground states by these spin states and their interactions: The coupling strength J_1 of channel $k = 1$ is influenced by the adsorption site of MnPc on the Pb(111) surface.

Strong coupling leads to the reduction of the impurity spin by 1/2 due to Kondo screening (left data points in Fig. 5.6 (b)). An illustration of the spin levels is shown in the left of Fig. 5.7 (a), where the spins are represented by arrows. Kondo screening of the spin in channel $k = 1$ is indicated by the white arrow surrounded by the Kondo screening cloud, depicted as gray arrows. At the same time, the spin in $k = 2$ remains unscreened (red arrow) due to the weak interaction with the substrate. Consequently, the effective total spin of the system is reduced to $S = 1/2$ by Kondo screening. Tunneling into the Shiba state drives the excitation to a spin state $S^* = 1$. Here, the asterisk denotes the excited state. In the presence of magnetic anisotropy, this excited state is split into three states, whose energy splitting reflects the magnetic anisotropy parameters D and E. The Shiba states are excitations from the "Kondo screened" ground state into the anisotropy-split excited state levels. The excitation scheme for this process is given in Fig. 5.7(a) on the right. All three excitations have equal probabilities, which leads to equal relative peak intensities of the Shiba states. Due to the coupling with the quasiparticles in the substrate, the anisotropies in the system can be renormalized, which leads to smaller values of the anisotropies [164]. As the splitting $E_{\mathrm{b2}} - E_{\mathrm{b1}}$ is smaller than $E_{\mathrm{b3}} - E_{\mathrm{b2}}$, the system has an easy-axis anisotropy ($D < 0$).

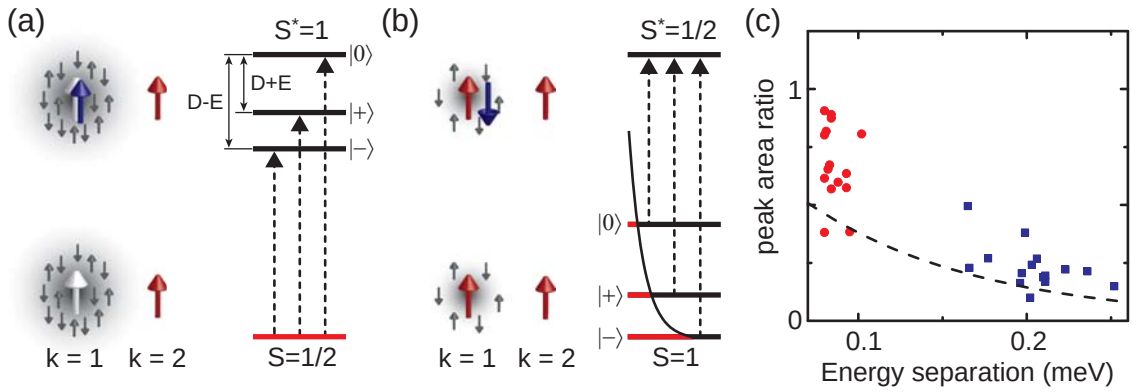

Figure 5.7: (a) Scheme of the many-body ground state in the "Kondo screened" regime. The spin (*white*) in scattering channel $k = 1$ is screened and the tunneling electron (*blue*) can enter with its spin parallel to the spin in $k = 2$, increasing the total spin of the excited state to $S^* = 1$. The excitation scheme including the anisotropy-split excited state is shown on the right. (b) Scheme of the "free spin" ground state and the respective excited state. The spin in $k = 1$ (*red*) is only partially screened. The tunneling electron has to enter this state in an anti-parallel alignment, thus reduces the spin to $S^* = 1/2$. Red lines in the excitation scheme symbolize the thermal occupation of the anisotropy-split ground state. (c) Peak area ratios plotted vs. their respective energy splitting from all spectra in the "free spin" ground state. A Boltzmann distribution for $T = 1.2\,\mathrm{K}$ is sketched as dashed line. Figure adapted from [124].

In the case of weak coupling, the spin in $k = 1$ is not screened (data points on the right in Fig. 5.6(b)). The total spin of the system in the ground state is $S = 1$. In Fig. 5.7(b), two red arrows represent both channels, which are unscreened. The excited state probed by the Shiba resonance has a spin $S^* = 1/2$, because the electron attached to $k = 1$ (blue arrow, upper part) obeys Pauli's exclusion principle and aligns anti-parallel. In this case, the ground state with $S = 1$ is split by magnetic anisotropy while the excited state is not [Fig. 5.7(b)]. Anisotropy-split ground state levels will be occupied according to a Boltzmann distribution. Therefore, the excitation probabilities are proportional to the level occupation and should thus directly reflect a Boltzmann distribution. This behavior is observed in Fig. 5.7(c), where the peak intensity ratios are plotted as a function of the energy separation of the Shiba states. With increasing energy separation, the relative peak area ratios decrease. This is in agreement with a Boltzmann distribution at 1.2 K (black dashed line) or slightly higher and reflects a temperature-induced occupation of the anisotropy-split ground state. In the zero temperature limit discussed in Ref. [164], only one excitation can be detected in the "free spin" regime. Higher levels are not occupied.

This model provides an explanation for the splitting of the Shiba states in MnPc on Pb(111) in the entire range of observed exchange couplings. Most notably, the many body ground state of the molecule-surface system can be unambiguously determined only by the number of Shiba states and their relative intensities in the two ground states.

5.7 Summary and Conclusion

In this chapter, we investigated manganese phthalocyanine on superconducting Pb(111). At 1.2 K, we observed multiple Shiba states inside the superconducting energy gap. Depending on the adsorption site of MnPc, the energy as well as the splitting of the Shiba states vary throughout the superconducting gap. Their collective behavior could be explained in terms of magnetic anisotropy in the system, introduced by the immediate environment of the Mn ion, *i.e.*, the organic ligand and the substrate. Magnetic anisotropy splits either the ground state or the exited state into three levels. Along with this, the previously seen quantum phase transition from the "Kondo screened" state to the unscreened "free spin" state could be confirmed [51]. For the assignment of the many body ground states in both regimes, the intensities of the Shiba states were analyzed. They showed equal intensities in the case of the "Kondo screened" ground state, where the Shiba state corresponds to an excitation of a spin $S = 1/2$ into an anisotropy-split spin 1 system. In the "free spin" ground state, a thermal occupation of the anisotropy-split ground state was found, which led to an intensity distribution of the Shiba states, reminiscent of a Boltzmann distribution.

In general, the present study provides insights into the mechanisms that lead to the formation of multiple Shiba states. In addition, it shows the importance of anisotropy effects on the subgap excitations, which determine the electron transport properties. These results can be compared to other systems that exhibit multiple Shiba states and help to clarify their origin as well as determine the spin state by the number and relative intensities of the Shiba states. Tuning the magnetic anisotropy with a different organic ligand will also affect the exchange coupling strength to the surface.

Arrangements of individually engineered magnetic molecules into coupled structures with a tunable number of Shiba states and their energies can be used to design systems with peculiar properties. For example, subgap bands play an important role in the search of topological phases and Majorana states in ferromagnetic chains coupled to an s-wave superconductor [175].

A controlled change of the local environment around the central metal ion can be used to tune the splitting of Shiba states as well as their energy inside the superconducting gap. Additional ligands possibly change the coordination of the metal ion in the phthalocyanine, thus will have an influence on the coupling to the substrate as well as on the anisotropies. We will explore this possibility in the next chapter.

Chapter 6

Modifying the Coupling between MnPc and Pb(111) by Ammonia Adsorption

6.1 Introduction

The precise control of the properties of magnetic impurities on surfaces, such as the spin state and magnetic anisotropy, is one of the ultimate goals in order to fabricate single atom or molecule devices used for data storage purposes. The study of MnPc adsorbed on Pb(111), presented in chapter 5, showed the sensitive interplay between the molecule-substrate interaction and the organic ligand, which greatly affects the magnetic anisotropy as well as the ground state spin of the system. Small changes in the adsorption site of the molecule led to different exchange coupling strengths. They induced a quantum phase transition of the system between two distinct ground states.

A deliberate change of the spin state requires means to manipulate the close environment of a single molecule. This can be accomplished by a chemical reaction of the organic ligand around the metal center [37, 77, 176]. However, in most cases, such reactions are irreversible. Another approach addresses an electronic decoupling of the impurity spin from the substrate by an insulating layer like copper nitride or boron nitride [36, 177, 178].

Recently, the influence of axial ligands attached to molecules has been studied in order to tune the molecule-substrate interaction and the spin state [167, 179–184]. The advantage of axial ligands is the reversibility of the ligand adsorption as well as the addressability of individual molecules.

Adsorption of axial ligands has shown to electronically decouple the metal center of a metal-organic molecule from the substrate [37, 185, 186], which counteracts the reduction of the total spin by Kondo screening. Small diatomic molecules such as nitrogen monoxide (NO) and carbon monoxide (CO) have shown to change the spin state of metal-organic molecule [181, 187]. For NO coordination, a partial change of the oxidation state of the central metal ion was observed [183]. Another ligand that has shown to change the spin state of metal-organic molecules on surfaces is ammonia (NH_3), which is diamagnetic ($S = 0$).

In this chapter, we will investigate the influence of ammonia on the system of MnPc on Pb(111). We will characterize the influence of ammonia on the exchange coupling to the substrate quasiparticles by the Shiba states. Furthermore, magnetic fingerprints in the normal conducting state are investigated to support measurements in the superconducting regime.

6.2 MnPc-NH_3 on Pb(111)

Deposition of a submonolayer of MnPc on Pb(111) is done as described in chapter 5. Additionally, ammonia is dosed through a leak valve attached to the preparation chamber. Similar to other small gaseous molecules, we expect ammonia to adsorb on the surface only at low temperatures. For this reason, the prepared system of MnPc on Pb(111) is cooled to 15 K during ammonia dosage. NH_3 on the bare Pb(111) surface is highly mobile when imaged at 1 K and can be easily dragged across the surface by the tip. It is thus desirable to remove any excess ammonia. To this end, we place the sample in a parking slot attached to the liquid nitrogen cryostat at 77 K. After some time, NH_3 is found only on MnPc molecules and not on Pb, probably because the adsorption energy on MnPc is larger compared to Pb.

6.2.1 Structure of MnPc-NH_3

A typical STM topographic image of MnPc-NH_3 on Pb(111) is shown in Fig. 6.1(a). It displays a large molecular island with a square arrangement. Molecules with two different apparent heights are found. Fig. 6.1(b) shows a zoom on the area highlighted by a box in Fig. 6.1(a). Lower molecules clearly show the familiar clover shape of MnPc. In contrast, molecules with a larger apparent height exhibit a central protrusion and a faint four-fold symmetry around the center. We associate these molecules with MnPc-NH_3. A height profile along the molecular row indicated by the blue dashed line in Fig. 6.1(b) is shown in Fig. 6.1(c). The apparent height of MnPc is 2.2 Å. MnPc-NH_3 have different apparent heights of 3.3 Å and 3.9 Å. The analysis of various MnPc-NH_3 molecules shows a continuous height distribution in the range between 2.9 Å and 3.9 Å. The main contribution to the increased apparent height of MnPc-NH_3 can be accounted to a change of the molecular structure. Minor influences on the height may be due to slight differences in the conductance of MnPc-NH_3. The inset of Fig. 6.1(a) shows a molecular model of MnPc-NH_3 with the expected adsorption geometry of NH_3 [188].

6.2.2 Tip-induced Desorption of Ammonia

In order to prove our assumption that the higher molecules correspond to MnPc-NH_3, we can try to remove the ligand. Recent studies on CO, NO and NH_3 coordinated to porphyrines have shown the reversibility of the ligand adsorption. Thermal desorption of the ligands restored the initial properties in these systems [179, 183, 185]. Ligands can be removed individually by a tip-induced voltage pulse [167, 186, 189, 190]. The tip was placed directly on top of one molecule and the bias was continuously increased with a disabled feedback loop. An example of the tunneling current during a voltage ramp is shown in Fig. 6.1(d). While increasing the bias voltage (black curve), a sudden drop in the tunnel current indicates the ammonia desorption. No additional

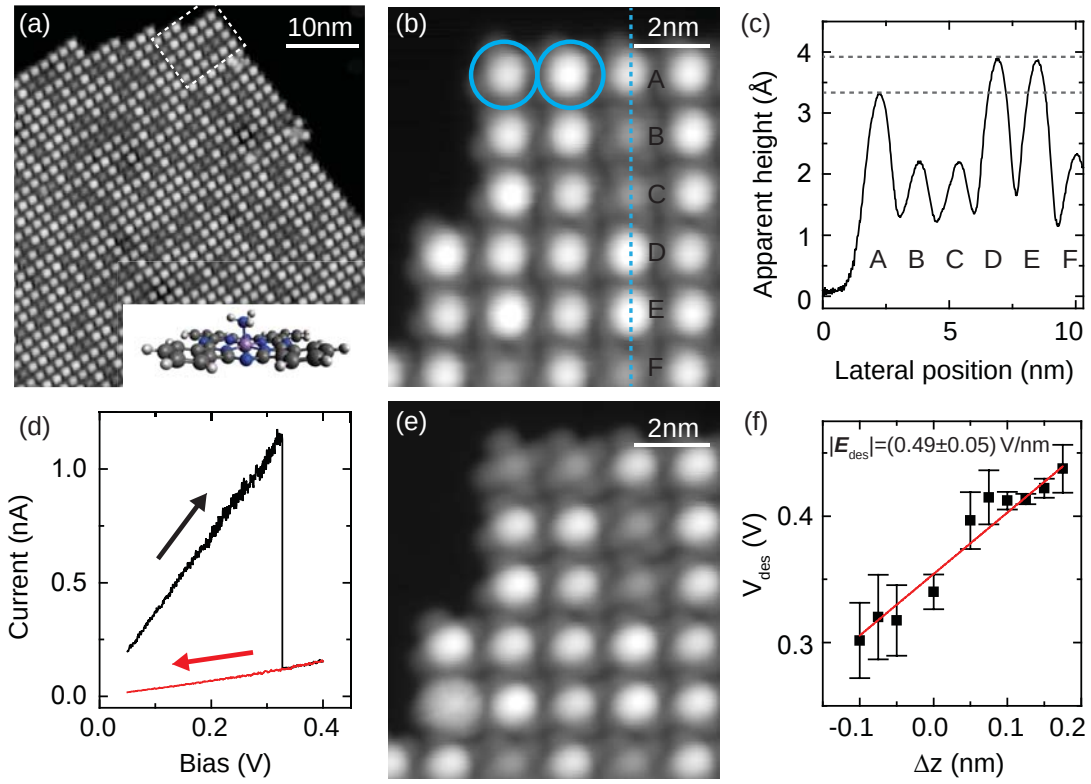

Figure 6.1: (a) Large scale topography of an MnPc molecular island partially covered with ammonia. The inset shows a structural model of MnPc-NH_3. (b) Zoom-in on a smaller region of the island (white dashed box) in (a). (c) Height profile across the blue dashed line in (b). MnPc appears lower than MnPc-NH_3. The variation of the height of MnPc-NH_3 is captured by the two horizontal dashed lines as the extreme values. (d) Tunneling current of a typical voltage ramp to desorb ammonia. The forward ramp is shown in black, the backward ramp in red. (e) Topographic image after desorption of two ammonia ligands from different MnPc molecules in (b). (f) Threshold voltage for ammonia desorption as a function of the relative tip approach. The error bars result from the variation of V_{des} for different MnPc-NH_3 molecules. A linear fit to the data to obtain the electric field is shown in red. Feedback opened at: V_{bias}=50 mV, I_{tunnel}=200 pA, Δz=0. Scanning parameters for all images: V_{bias}=50 mV, I_{tunnel}=100 pA.

change is observed when decreasing the sample bias. On two molecules, marked by blue circles in Fig. 6.1(b), voltage ramps were used to desorb ammonia. An image recorded after the voltage pulses, shown in Fig. 6.1(e), reveals the successful desorption of NH_3. Both molecules exhibit the known shape of MnPc.

Distance-dependent measurements help to identify the desorption mechanism of NH_3. Fig. 6.1(f) shows the threshold voltage of the desorption as a function of relative tip approach. Zero tip approach corresponds to the tip-sample distance at which the feedback is opened (parameters are: V_{bias}=50 mV and I_{tunnel}=200 pA). Negative values indicate a reduction of the tip-sample distance. A linear increase of the threshold voltage with increasing tip-sample separation is found. Such a linear dependence can be explained by an electric field-induced desorption mechanism [167]. The tunneling junction can be modeled by a parallel plate capacitor, where the electric field depends on the voltage V_{des} and the plate distance d as in section 4.4:

$$|\boldsymbol{E}_{\mathrm{des}}| = \frac{V_{\mathrm{des}}}{d}. \tag{6.1}$$

A fit to the data in Fig. 6.1(f) yields a critical electric field of 0.49 ± 0.05 V/nm. For the desorption of CO from MnPc on Bi(111), a critical field of 1 V/nm was extracted [167], which is more than twice as large for the present system, probably owing to the different ligand.

When a tunneling current is still flowing, *i.e.*, at small tip-sample distances, a contribution of tunneling electrons can not be excluded [16]. Studies of ammonia on bare Cu(100) found molecular vibrations excited by tunneling electrons to drive the desorption from the surface [190, 191]. In order to verify other influences on the desorption of NH_3 from MnPc, a more detailed analysis is necessary. Here, we focus on the influence of ammonia on the electronic properties of the MnPc on Pb(111) and leave the study of the exact desorption mechanism to other investigations.

6.3 Shiba States in the Superconducting State

Spectroscopy on MnPc-NH_3 in the superconducting state can reveal the influence of ammonia on the exchange coupling J to the superconducting quasiparticles and on the spin state. We expect a modification of the electronic structure and the coupling strength of MnPc to Pb(111) by ammonia adsorption. On metal substrates, a change of the spin state of a metal-organic molecules was observed [188, 192, 193]. These changes can manifest in the subgap structure, *i.e.*, the Shiba states for MnPc-NH_3.

6.3.1 Modification of the Exchange Coupling to the Surface

To probe the subgap structure of MnPc-NH_3 on Pb(111), we acquire $\mathrm{d}I/\mathrm{d}V$ spectra using a superconducting tip, as done in chapter 5. The upper graph of Fig. 6.2(a) shows a spectrum of a typical MnPc-NH_3 inside a molecular island (black line) at 1.1 K. A reference spectrum on pristine Pb is displayed in gray. On MnPc-NH_3, Shiba states are present inside the superconducting gap. In contrast to pure MnPc on Pb(111), only one pair of Shiba states is observed with higher spectral intensity at positive bias. After desorbing the ammonia ligand, the $\mathrm{d}I/\mathrm{d}V$ spectrum exhibits the known triplet of MnPc, shown in the lower graph in Fig. 6.2(a). The change of the high-intensity component of the Shiba state from positive to negative energies with ammonia desorption is noteworthy.

This change in intensity can have different origins: A) a significant contribution of resonant Andreev processes, as observed for Mn atoms on Pb(111) [118]; B) a strong modification of the

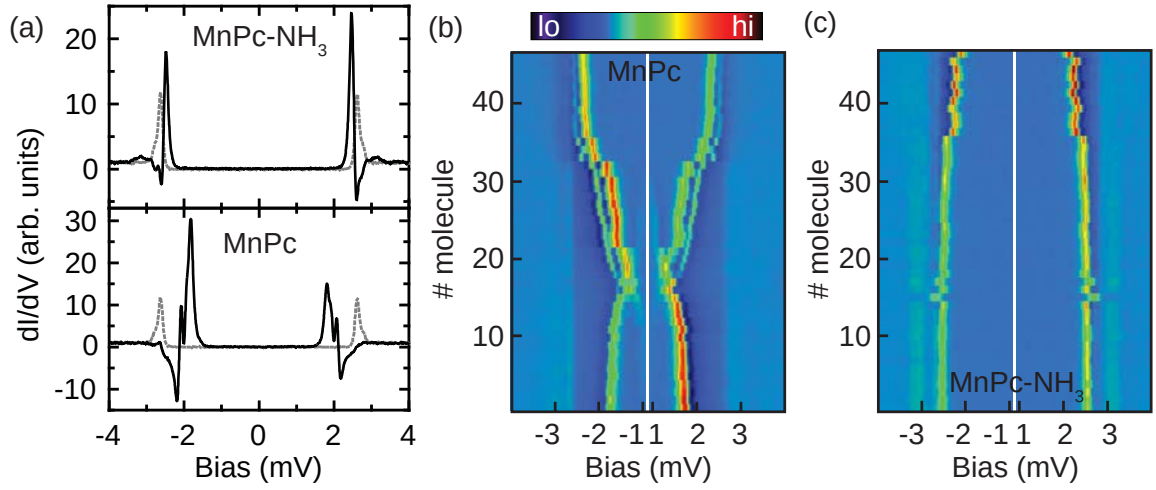

Figure 6.2: Comparison of Shiba states with and without ammonia. (a) dI/dV spectra of MnPc with attached NH_3 (upper panel) and after tip-induced NH_3-desorption (lower panel). Gray dotted lines are spectra on the pristine Pb surface. (b) 2D color map of dI/dV spectra (horizontal lines) on MnPc after NH_3-desorption, ordered according to their Shiba state energies, increasing from top to bottom. Energies in the interval $E \leq \pm 1\,\mathrm{meV}$ are omitted. The color denotes the spectral intensity. (c) 2D color map of dI/dV spectra on the same molecules as in (b), but with NH_3 still attached. The order from top to bottom is according to the spectra in (b). Feedback opened for all spectra at: V_{bias}=5 mV, I_{tunnel}=0.2 nA.

Coulomb repulsion U; C) a change of the exchange coupling strength between the Mn ion and the superconducting quasiparticles.

Tunneling currents of I_{tunnel}=200 pA at a bias of V_{bias}=5 mV during spectroscopy correspond to a normal state conductance of $5 \cdot 10^{-5} G_0$, where G_0 is the quantum of conductance. Such a low conductance should ensure single-particle tunneling [118]. To support this assumption, we have a look at the relative intensities of the Shiba state components at positive and negative energies. Fig. 6.3 shows dI/dV spectra on a MnPc-NH_3 molecule at different distances. The ratio of the Shiba state components, given as α_+/α_-, decreases from 1.42 at 0 pm to 1.11 at 300 pm. We interpret the decrease of the ratio with the tip approach as a sign of a rising contribution of Andreev processes. Mn atoms on Pb(111) showed an inversion of the Shiba state intensities small tip-sample distances. It was assigned to the crossover between single-particle and Andreev contributions [118]. With these observations, we can discard possibility A). Therefore, the intensity of the Shiba states reflects the density of states of the sample (convoluted with the tip DOS).

At this point, we can not exclude possibility B). However, in the following we will investigate the Shiba states and are able to show that the change in the Shiba state intensities corresponds to a change of the molecule-substrate interaction, which drives the system across a phase transition into a different many-body ground state [51, 52, 124].

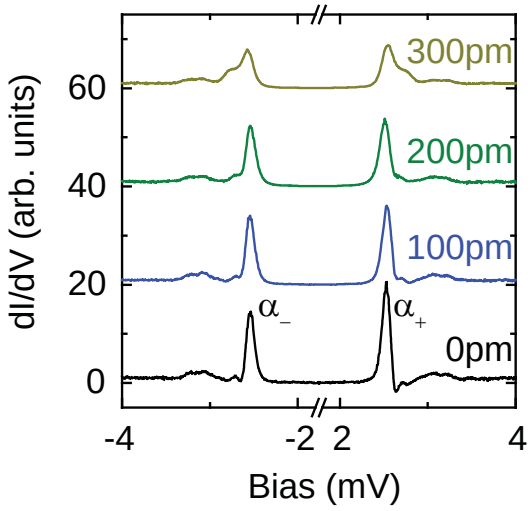

Figure 6.3: $\mathrm{d}I/\mathrm{d}V$ spectra on a MnPc-NH_3 molecule at different relative tip-sample distances as indicated in the graph. Positive values for the relative distance refer to an approach of the tip. Spectra offset for clarity. Feedback was opened at V_{bias}=5 mV and I_{tunnel}=200 pA. Bias voltages in the interval $|V_{bias}|$=1.8 mV are omitted.

For MnPc, different adsorption sites of MnPc led to different exchange couplings. We recorded $\mathrm{d}I/\mathrm{d}V$ spectra on various MnPc-NH_3 molecules within a molecular island. Afterwards, the ammonia molecules were removed by voltage pulses and $\mathrm{d}I/\mathrm{d}V$ spectra were recorded on the resulting MnPc molecules. In Fig. 6.2(b) and (c) the conductance traces of all probed molecules are plotted in a 2D color plot. Each horizontal line corresponds to a spectrum of one molecule. The spectral intensity is transformed into a color scheme which allows the identification of the Shiba states. Spectra within the plots are sorted according to the mean energy of the Shiba triplet in MnPc [Fig. 6.2(b)] with increasing energies from top to bottom. Fig. 6.2(c) shows the corresponding $\mathrm{d}I/\mathrm{d}V$ spectra of the molecules before ammonia desorption. This one-to-one correspondence between MnPc and MnPc-NH_3 allows a direct comparison and consequently allows to investigate the role of ammonia.

The energy of the Shiba triplet varies substantially for MnPc and the crossing of the Fermi level is observed. In contrast, all MnPc-NH_3 molecules exhibit Shiba states at positive energies and the Shiba state energy varies less strongly. A property common to both molecular species is the direction of the Shiba state shift with the adsorption site. In the top spectrum of Fig. 6.2(b), energy of the Shiba state indicates the strongest exchange coupling [51, 52]. The same molecule with NH_3 adsorbed also has the Shiba state with the lowest energy for all presented spectra [Fig. 6.2(c)]. A similar shift of the Shiba state energy to higher values is seen in the spectra of MnPc and MnPc-NH_3. However, the total extent of the energy shift is smaller in MnPc-NH_3. The similar shift of the Shiba state energies for both molecular species suggests a systematic influence of ammonia on MnPc.

In MnPc-NH_3, an additional bond is formed between the Mn center and the ammonia. The surface trans effect [185] then leads to a weakening of the bond between the Mn ion and Pb. In ref. [187], Isvoranu *et al.* studied iron phthalocyanine (FePc) on Au(111) and the effect of different axial ligands on the spin state and electronic coupling to the substrate. They found an electronic decoupling of the iron center from the surface due to the adsorption of different ligands. In a

different study, calculations on ammonia-coordinated nickel porphin on Co(100) found that the Ni center was pulled away from the surface towards the ammonia ligand, increasing the Co-Ni distance by about 0.5 Å [192].

In the present system, we expect the ammonia ligand to affect the system in a similar way. In the model of a classical spin, the Shiba state energy is related to the exchange coupling parameter J according to Eq. (3.26). An electronic decoupling and a lift of the Mn center away from the surface upon NH_3 coordination reduces J and thus shifts the Shiba state energy towards positive energies. This is in agreement with the observations in the dI/dV spectra in Fig. 6.2(b) and (c). The coupling strength still depends on the adsorption site, but is generally reduced for MnPc-NH_3. The non-linearity of the shift of the Shiba states from MnPc to MnPc-NH_3 could be explained by the nonlinear dependence of the Shiba state energy on the exchange coupling J, as found in Eq. (3.26). A quantitative analysis of the energy shift of the Shiba states and its relation to the exchange coupling strength remains for a future analysis. The quantum mechanical nature of the impurity spin should be taken into account, which includes internal spin dynamics such as Kondo screening. Based on the observations, we conclude that the shift of the Shiba states is caused by a reduction of the exchange coupling strength upon ammonia adsorption.

MnPc-NH_3 is likely in the "free-spin" ground state with a spin of S=1, similar to MnPc (cf. chapter refchap:MnPc). In contrast to measurements on MnPc, where three anisotropy split Shiba states were observed, here only one Shiba state is present. This is in contrast to the assumption of a spin state of $S = 1$. Besides a change of the total spin of the system [187, 188, 192, 193], a modification of the anisotropy parameters can account for the absence of multiple Shiba states. In the "free-spin" ground state, the levels of the $S = 1$ are split by magnetic anisotropy and thermally occupied [124]. If the level splitting exceeds the thermal energy at 1.1 K, higher levels are not populated and only one Shiba state can be seen. Measurements at elevated temperatures could reveal additional Shiba states corresponding to anisotropy-split ground state levels.

6.3.2 Thermal Occupation of Anisotropy-Split Shiba States

At temperatures as low as 1.1 K, we only observe one pair of Shiba states on MnPc-NH_3. To check for ground state levels at higher energies, we increased the temperature stepwise up to 4.0 K. Fig. 6.4(a) shows a 2D color map of dI/dV spectra at different temperatures measured on a MnPc-NH_3 molecule, where only the spectral intensity at positive energies is shown. At approximately 1.8 K, a second Shiba state develops at energies closer to E_F and at 2.4 K a third Shiba state is observed. An overall reduction of the Shiba state energies is observed with increasing temperature. Within our spectral energy resolution, this behavior is in line with the temperature-dependent reduction of the superconducting gap, seen by the equivalent shift of the superconducting gap edge (light green step on the right of the Shiba states). The intensities of the additional Shiba states increase at higher temperatures. At all temperatures, the outer Shiba state is most intense and the inner Shiba state has the lowest intensity. This is similar to MnPc in the "free-spin" ground state. We can assume that MnPc-NH_3 is also in the "free spin" ground state, which is split by magnetic anisotropy. Up to three Shiba states are observed on different MnPc-NH_3 molecules, whereas in some cases, only two Shiba states could be resolved. In Fig. 6.4(b), two examples of dI/dV spectra at temperatures of 1.1 K and 4.0 K are presented.

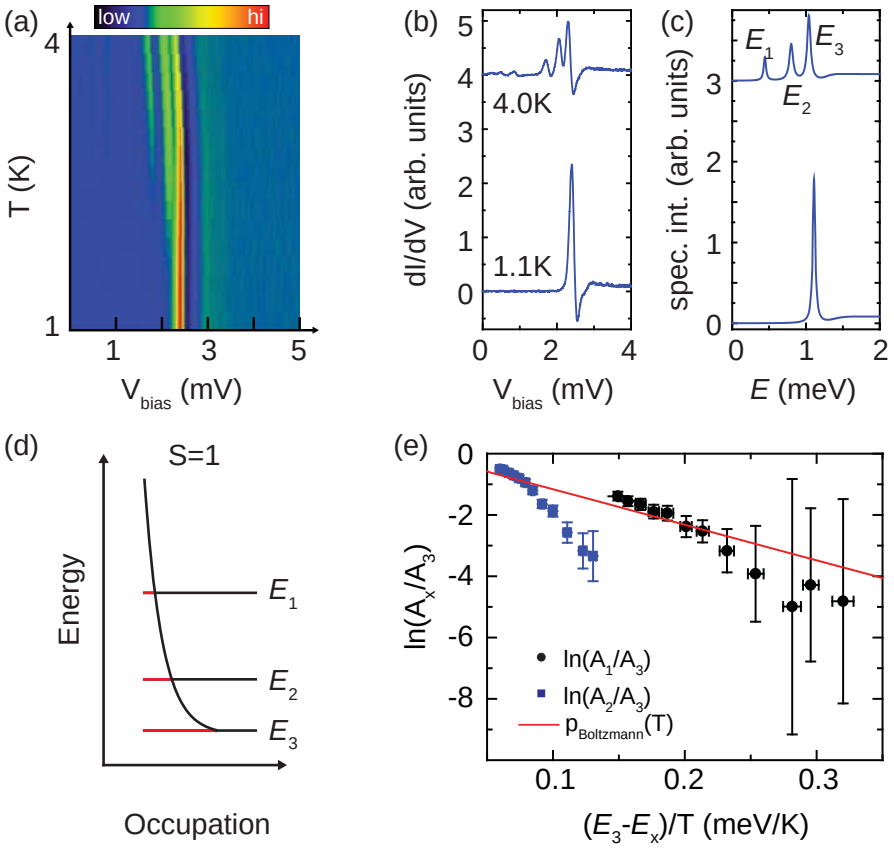

Figure 6.4: (a) 2D color map of the positive energy part of dI/dV spectra on MnPc-NH_3 at different temperatures. The highest temperature is 4.0 K (top) and temperature intervals are 0.2 K down to 1.2 K. The bottom spectrum is measured at 1.1 K. With increasing temperature, additional Shiba states evolve at energies closer to E_F. (b) Positive part of the dI/dV spectrum at 1.1 K (lower spectrum) and 4.0 K (upper spectrum) from MnPc-NH_3 in (a). Additional Shiba states at 4.0 K are present. Spectra are offset for clarity. (c) Deconvoluted spectral intensity of spectra in (b). (d) Illustration of the anisotropy-split ground state levels (black) and occupation (red) due to a Boltzmann distribution. (e) Plot of the logarithm of the Shiba state area ratios as a function of the energy splitting divided by temperature. For a thermal occupation of the Shiba states, the points should follow a Boltzmann distribution (solid red line). Feedback for spectra opened at: V_{bias}=5 mV, I_{tunnel}=200 pA.

For a quantitative analysis of the peak intensities, we deconvolve the dI/dV spectra using the method described in appendix I. The deconvoluted signal of the spectra in Fig. 6.4(b) is shown in Fig. 6.4(c). We label the Shiba state energies as E_1, E_2 and E_3. Their respective intensities A_1, A_2 and A_3 correspond to the integrated peak area. No change of the energy splitting of the three Shiba states with increasing temperature is observed. Their respective energy splittings are E_3-

E_2=0.24 ± 0.01 meV and E_2-E_1=0.36 ± 0.02 meV. The error of the energy splittings corresponds to the standard deviation of the determined splittings obtained at different temperatures. The determination of the energy splitting of the Shiba states on multiple MnPc-NH_3 molecules, which exhibit three Shiba states, yields a variation of E_3-E_2 between 0.19 meV and 0.41 meV. For E_2-E_1 the peak splittings vary between 0.26 meV and 0.40meV. In most MnPc-NH_3 molecules, the Shiba state splitting is larger than for MnPc on Pb(111). A change of the splitting is not surprising because the coordination of ammonia is expected to change the magnetic anisotropy in the system. The ligand field of the complex becomes more octahedral and, at the same time, lifts the Mn ion away from the surface. This changes the strength of the ligand field. It has been shown that a coupling of metal atoms to the conduction electrons in the substrate leads to a renormalization of the magnetic anisotropies [194]. This renormalization causes a decrease of the magnetic anisotropy. In the case of MnPc-NH_3 on Pb(111), an electronic decoupling could reduce a renormalization and thus contribute to an increase of the magnetic anisotropy.

The presence of up to three Shiba states supports the assumption of a "free spin" ground state with $S = 1$ split by magnetic anisotropy. The intensity distribution of the Shiba states can yield further evidence to support this assumption. In thermal equilibrium, we expect the relative occupations of the Shiba states to scale with the temperature according to the Boltzmann distribution, given as:

$$\frac{N(E_x)}{N(E_3)} = \exp\left(-\frac{E_3 - E_x}{k_\mathrm{B}T}\right). \tag{6.2}$$

In this equation, E_x corresponds to the energy of level x and k_B is the Boltzmann factor. A schematic illustration of the level occupation for a system with three levels is shown in Fig. 6.4(d), where the relative occupation of the different levels is indicated in red. The Boltzmann distribution is shown by the black curve. We analyze the Shiba state intensities for the MnPc-NH_3 molecule shown in Fig. 6.4(a) to (c). For the Shiba state splitting E_3-E_2= 0.24 meV, we expect a relative occupation of 8 % for the level E_2 with respect to level E_3 at 1.1 K. A second peak with a relative intensity of 8 % should be observable. However, in the spectrum at 1.1 K, no trace of a second Shiba state is present.

A more detailed analysis of the relative Shiba state intensities at different temperatures is shown in Fig. 6.4(e). The graph contains a plot of the logarithm of the peak area ratios A_x/A_3, determined from the Shiba state intensities, as a function of the energy difference divided by the temperature, $(E_3 - E_x)/T$. The blue squares in Fig. 6.4(e) correspond to the peak area ratio A_2/A_3, whereas the black circles correspond to the peak ratio A_1/A_3. The energy splitting $E_3 - E_x$ is extracted from the deconvolved data for each temperature. Due to the different energy splittings E_3-E_2 and E_3-E_1, both intensity ratios need to be considered individually. Additionally, it should be noted that 1.8 K is the lowest temperature at which multiple Shiba states were observed. Experimental data in Fig. 6.4(e) thus correspond to the temperature interval between 1.8 K and 4 K.

According to Eq. (6.2), we expect a linear change of the area ratios with a slope of $-1/k_\mathrm{B}$, as we simply substitute $x = (E_x - E_3)/T$ and $y = \ln(N_x/N_3)$:

$$y = -\frac{x}{k_\mathrm{B}}. \tag{6.3}$$

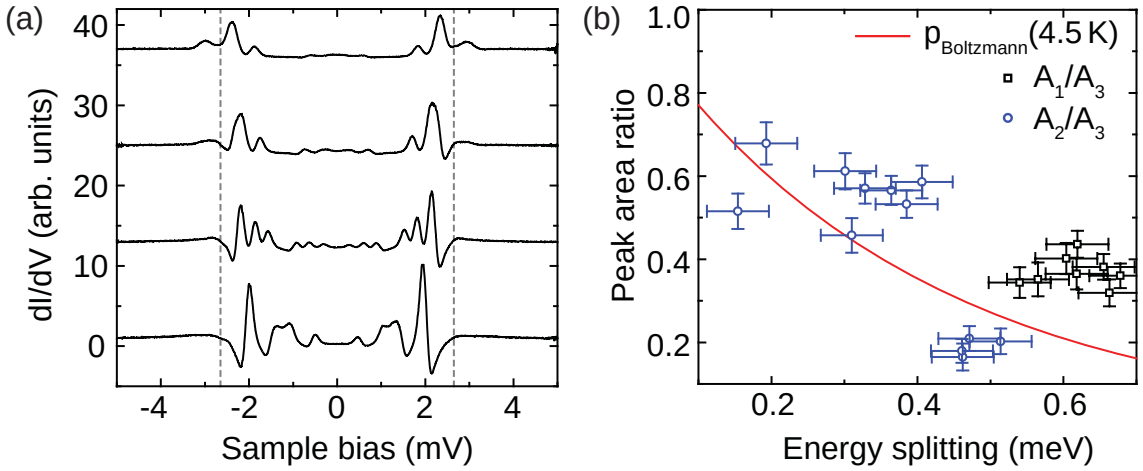

Figure 6.5: (a) Selection of MnPc-NH_3 with Shiba bound states at different energies, decreasing from top to bottom. Gray dashed lines indicate the superconducting gap. Feedback opened at: V_{bias}=5 mV, I_{tunnel}=0.2 nA. (b) Shiba peak area ratios versus their respective energy splitting for MnPc-NH_3 at 4.5 K. The red line represents a Boltzmann distribution at 4.5 K.

The expected linear behavior is shown as a red line in Fig. 6.4(e). Strikingly, there is poor agreement between the experimental data and the predicted Boltzmann distribution. At low temperatures, the intensity ratios are lower than predicted, while they exceed the expected ratios at high temperatures. The total intensity of all Shiba states, *i.e.*, the sum of the three Shiba state intensities, increases with the temperature by approximately 35 % (not shown here).

There seems to be a smaller deviation of the relative Shiba state intensities Fig. 6.4(e) at higher temperatures. We check the Shiba intensity distribution at 4.5 K for different MnPc-NH_3 molecules with respect to their energy splitting in Fig. 6.5. Four representative dI/dV spectra of MnPc-NH_3 molecules within a molecular island are shown in Fig. 6.5(a). They exhibit Shiba states at slightly different energies and with different splittings. The spectra are ordered by their Shiba state energy, decreasing from top to bottom. In the top spectrum, only two Shiba states are present. As the Shiba states shift further into the superconducting gap, up to three Shiba states can be distinguished. In the dI/dV spectrum at the bottom, the innermost Shiba state already overlaps with its thermally excited Shiba state. These spectra are not considered for a quantitative analysis. In Fig. 6.5(b) the peak area ratios are displayed as a function of Shiba state splitting. With increasing Shiba state splitting, the relative intensity of the additional Shiba states decreases. However, the behavior deviates from the Boltzmann distribution, indicated by the red line. The relative intensities of the inner Shiba peaks exceed the expected thermal occupation for temperatures ≈4.5 K, in agreement with the findings for high temperatures in Fig. 6.4(e).

A deviation from the expected thermal occupation can be an indication that the system is out of thermal equilibrium. One way to drive a system out of equilibrium is with high tunneling currents, such that the average time between two tunneling events is shorter than the time required for a thermal relaxation to the ground state. For tunneling currents of I_{tunnel}=200 pA, the average

time between two tunnel events is approximately 0.8 ns. Excited spin states of molecules on a superconductor have been found to have lifetimes of ≈10 ns, which is considerably longer [53]. The spin state was excited by inelastic electron tunneling. As particle-hole excitations around the Fermi level are blocked by the formation of the superconducting gap, relaxation to the ground state is hindered. For MnPc-NH_3, similar processes lead to a thermal excitation of the spin states in the ground state. It is possible that the superconducting gap blocks the formation of electron-hole pairs to occupy the higher spin projection levels of the ground state. In order to check this assumption, distance-dependent measurements at elevated temperatures have to be performed. The thermal behavior of multiple Shiba states thus can not be fully explained at this point. However, an influence of the temperature on the occupation of ground state levels at higher energy is evident from the occurrence of Shiba states at increased temperatures.

From the presence of multiple Shiba states at temperatures above 1.8 K, we can already make some assumptions about the spin state of MnPc-NH_3 on Pb(111). A system with a spin $S = 1$ can account for three anisotropy-split Shiba states. From the fact that the intensities of the three Shiba states in MnPc-NH_3 are different and depend on the temperature, we conclude that the system is in the "free-spin" ground state and has a spin of $S = 1$. The Shiba states correspond to excitations of the system to a state with $S = 1/2^*$. This assumption is supported by the fact that MnPc-NH_3 exhibits a higher spectral intensity of the Shiba components at positive energies. We therefore conclude that ammonia adsorption leads to a weakening of the exchange coupling strength of the adsorbate spin with the quasiparticles of the substrate. In comparison to MnPc on Pb(111), the total spin of the system is not changed. An evaluation of the Shiba state splittings for different molecules indicates that an easy-axis anisotropy ($D < 0$) is present and additional transverse anisotropy E. We obtain anisotropy parameters for D in the range from -0.33 ± 0.03 meV to -0.24 ± 0.03 meV and for E from 0.00 ± 0.01 meV to 0.10 ± 0.01 meV. In molecules, which exhibit only two Shiba states, we assume the transverse anisotropy is to small to observe a splitting into three Shiba states.

In previous studies, a change of the spin was observed upon ammonia coordination. An increase of the spin in phthalocyanine derivatives on ferromagnetic Co substrates was observed [188, 192]. In these systems, the $3d_{z^2}$ orbital is doubly occupied. Bond formation to ammonia involves the $3d_{z^2}$ orbital, which is lifted in energy. The d_{z^2} orbital and $d_{x^2-y^2}$ orbital are then at similar energies. Single occupation of both orbitals becomes energetically favorable, which results in an increase of the spin. On the other hand, in iron phthalocyanine molecules adsorbed on Au(111), the d_{z^2} orbital is only singly occupied [187, 193]. Ammonia adsorption raises the energy of the d_{z^2} orbital such that an anti-parallel pairing to the electrons in the d_π orbitals is favored. This reduces the spin.

Fig. 6.6(a) shows the energy alignment of the $3d$ orbitals in MnPc when adsorbed on Pb(111), which was obtained by numerical renormalization group theory calculations [172]. In the "free spin" ground state the unpaired electron in the d_{z^2} orbital is only weakly Kondo screened and below the d_π orbitals. A tentative scheme for the level alignment in MnPc-NH_3 is shown in Fig. 6.6(b). Adsorption of ammonia probably lifts the d_{z^2} orbital in energy. A slight increase of the d_π orbitals is conceivable as well, caused by a lift of the Mn ion away from the surface into the phthalocyanine ligand. This rearrangement of the $3d$ orbitals can well account for a change of the magnetic anisotropies, thus leading to a different Shiba state splitting. However, the total

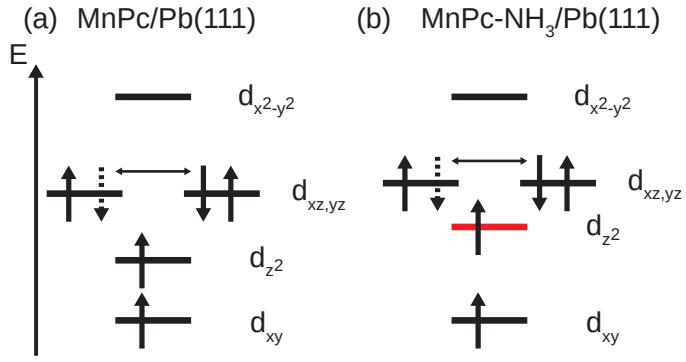

Figure 6.6: (a) $3d$ orbital arrangement of MnPc on Pb(111). Arrows represent spins occupying the levels (adapted from [172]). (b) Tentative level arrangement for MnPc-NH_3 on Pb(111). The d_{z^2} level is shifted to higher energies, shown in red.

spin is retained in this situation. If the strong hybridization of the d_π orbitals with the organic ligand still screens the unpaired spin in this orbital, the total spin state of MnPc-NH_3 is assumed to be $S = 1$.

6.3.3 Inelastic Spin Excitations and Shiba States

Besides the presence of Shiba states, we observe low-intensity resonances outside the superconducting gap. Fig. 6.7(a) shows a $\mathrm{d}I/\mathrm{d}V$ spectrum, where two peaks are present at ≈3 mV. Interestingly, the intensity of these features outside the superconducting gap is related to the energy of the Shiba state. A graph with multiple $\mathrm{d}I/\mathrm{d}V$ spectra of MnPc-NH_3 is shown in Fig. 6.7(b). The spectra are ordered by their Shiba state energy, increasing from red to green. In the spectra with Shiba states lowest in energy, no features outside the gap are observed. With increasing Shiba state energies, the intensity of the resonances outside the gap increases. However, their small intensities and close energies complicate a clear distinction.

For $\mathrm{d}I/\mathrm{d}V$ spectra that allow a determination of the resonance energies, we find energies from (3.0±0.1) to (3.2±0.1) meV for the resonance lowest in energy and from (3.2±0.1) mV to (3.3±0.1) mV for the resonance at highest energy. For these molecules, the Shiba state position varies from (2.4±0.1) mV to (2.6±0.1) mV, which is in the same order as the variation of the resonances outside the superconducting gap. A spectrum recorded on the same MnPc-NH_3 as in Fig. 6.7(a) but at 4.5 K reveals that the energy difference between the resonances and the respective Shiba states is in the order of the Shiba state splitting [Fig. 6.7(c)]. One additional Shiba state is present in the superconducting gap at 4.5 K. At this temperature, only one resonance is observed outside the superconducting gap, as an effect of thermal broadening. Tentative fits of Lorentzian line profiles to these features do not match the experimental data well. However, rough estimation of the peak energies can be done. Only a small number of MnPc-NH_3 molecules was investigated at 4.5 K, therefore a direct comparison of the Shiba state splittings with features outside the superconducting gap is not reliable. We can still argue about the origin of these resonances by looking at the properties of the system in the superconducting state.

Narrow peaks outside the superconducting gap have been assigned to inelastic spin excitations of a high-spin molecule ($S = 5/2$) on a superconductor [53, 195]. On a superconductor, spin excitations are seen as a convolution of a step and a peak. This is due to the peculiar DOS of

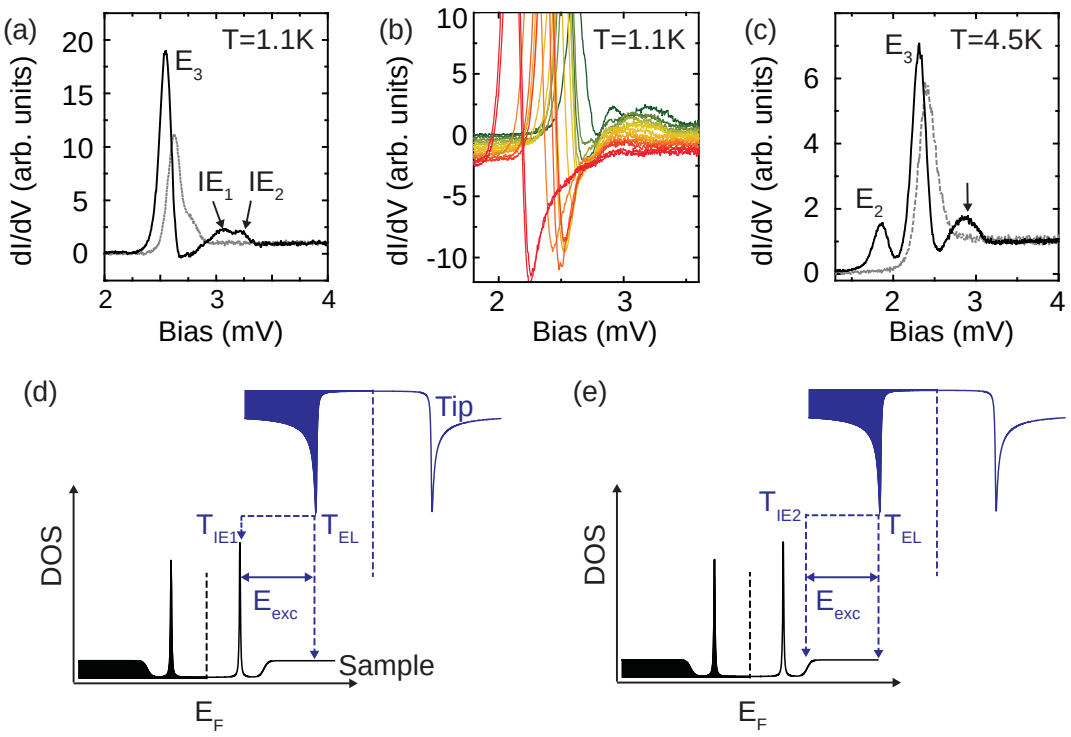

Figure 6.7: (a) dI/dV spectrum recorded on MnPc-NH_3 at 1.1 K. Low-intensity features are present at energies slightly above the BCS quasiparticle peaks. The gray spectrum is recorded on pristine Pb. Feedback opened at V_{bias}=5 mV and I_{tunnel}=0.2 nA. (b) Multiple dI/dV spectra recorded on different MnPc-NH_3 molecules, sorted by the Shiba state energy increasing from red to green (spectra offset for clarity). (c) dI/dV spectra of the same MnPc-NH_3 molecule as (a), but at 4.5 K. An additional Shiba state is present at lower energies. (d) Illustration of the involved elastic and inelastic tunneling processes in the model to explain the resonances outside the gap. Tunneling pathways are indicated as T_{EL}, T_{IE1} and T_{IE2}.

the BCS superconductor. Inelastic tunneling only occurs at bias voltages above the excitation threshold. In a superconductor, inelastic tunneling can only occur at a bias, which is the sum of the excitation energy and the energy of the superconducting gap. The sharp BCS quasiparticles at the gap edge lead to the peak shape of inelastic excitations.

We can explain the peaks outside the gap on MnPc-NH_3 as inelastic excitations of the anisotropy-split ground state levels. Up to two inelastic excitations are possible in a system with three levels. This is in agreement with the peaks shown in the spectrum in Fig. 6.7(a). In the case of MnPc-NH_3, inelastically tunneling electrons can tunnel into or out of Shiba states. An example of a tunnel junction is shown in Fig. 6.7(d). The tip DOS (blue) exhibits the well-known BCS quasiparticle peaks at the edge of the superconducting gap. The sample DOS (black) exhibits Shiba states inside the step-like superconducting gap. The inelastic excitation has an energy of E_{exc}.

Then the inelastic channel opens at a bias of $V_{bias}=\Delta_{tip} + E_{Shiba} + E_{exc}$. The elastic tunneling path is denoted as T_{EL} and the inelastic path is denoted as T_{IE1}. In this case, the inelastic path leads to a tunneling via the Shiba state. However, a second inelastic channel (T_{IE2}) opens at a higher bias voltage $V_{bias}=\Delta_{tip} + \Delta_{sample} + E_{exc}$, as shown in Fig. 6.7(e). In this case, the same inelastic excitation as in Fig. 6.7(d) leads to a tunneling into the normal states outside the superconducting gap, after donating the energy to the spin excitation. Due to the low intensity of the superconducting gap, the second channel will not lead to a strong step-like increase in the dI/dV signal. When the Shiba state is close to the superconducting gap, both tunneling paths are at the same energy and their intensities add up. A downshift of the Shiba state energy leads to a separation of the inelastic channels and therefore a reduction of the intensity of the inelastic signal. At the same time, the threshold bias of T_{IE1} decreases and shifts to energies inside the superconducting gap. The behavior observed for the resonances outside of the superconducting gap on MnPc-NH_3 can be qualitatively explained within this model.

It is certainly an interesting scenario when the same energy levels can be addressed and probed by two different mechanisms. Firstly, the Shiba states give a hint about the ground state levels, which can be thermally occupied. Secondly, even at low temperatures, where only the lowest ground state level is thermally occupied, inelastic electron tunneling spectroscopy can be used to occupy higher levels within the same spin state.

In contrast to Shiba states, inelastic spin-flip excitations can be observed in the normal conducting state. In the following section, we will study the normal state properties of MnPc-NH_3 on Pb(111). The weak exchange coupling of the molecular spin should be reflected by a very weak Kondo screening or its complete absence. Furthermore, we will check for inelastic spin-flip excitations in the normal state.

6.4 Kondo Effect in the Weak Coupling Regime

The coexistence of exchange coupling between the impurity spin with the superconducting quasiparticles on the one hand and superconducting pair formation on the other hand is evidenced by the Shiba states in the superconducting state. In the normal metallic state, no superconducting pairing is present. However, the exchange coupling can lead to the emergence of a Kondo resonance, whose width is related to the exchange coupling strength and can be compared to the Shiba state spectrum in the superconducting state. Shiba states on MnPc-NH_3 exhibited higher intensity at positive energies, suggesting a weak coupling. Thus we expect to find a Kondo resonance with a low Kondo temperature.

Here, we check for the presence of a Kondo resonance in the superconducting and the normal conducting state of the system. In the superconducting state, the convolution of the sharp BCS quasiparticle peaks in the tip DOS and the Shiba states in the sample DOS lead to intense features in dI/dV spectra, easily concealing a resonance around E_F.

In a magnetic field stronger than the critical field, the superconductivity is quenched. Bulk Pb has a critical magnetic field of $B_c \approx 80\,mT$. Pb coated tips can larger critical magnetic fields due to finite-size effects known from granular superconductors [196]. It has been shown to increase critical fields by a factor up to 5 for superconducting tips [197]. To still be able to measure at low magnetic fields, we use tips coated with Au, which have a rather flat DOS around E_F.

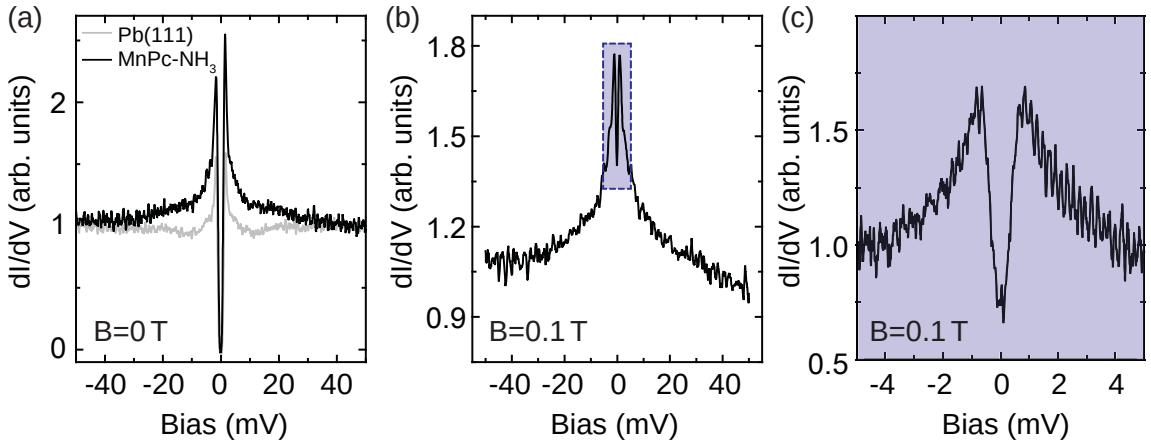

Figure 6.8: (a) dI/dV spectra on MnPc-NH_3 (black) and Pb (gray) with a Au tip. Feedback opened at V_{bias}=50 mV and I_{tunnel}=200 pA. (b) dI/dV spectrum on the same MnPc-NH_3 molecule as in (a), but with a magnetic field of B=0.1 T applied perpendicular to the surface. (c) Spectrum in a narrow energy range around E_F to resolve the dip feature in the blue box in (b). Feedback opened at V_{bias}=5 mV and I_{tunnel}=200 pA.

The black curve in Fig. 6.8(a) shows a dI/dV spectrum recorded on a typical MnPc-NH_3 molecule at B=0 T and T =1.1 K. The sample is still in the superconducting state. For comparison, a Pb spectrum is shown in gray. On MnPc-NH_3, the superconducting gap can still be observed and the presence of Shiba states is evidenced by the asymmetry of the peaks. In contrast to the spectrum on the clean substrate, the onset of a broad resonance around the Fermi level appears. In order to resolve the full resonance, we performed measurements with an applied magnetic field of 0.1 T to quench the superconductivity in the sample. An intense broad resonance around E_F appears in the spectral signal in Fig. 6.8(b), reminiscent of the Kondo effect. This resonance has some peculiar properties. First, the width of the resonance clearly exceeds the size of the superconducting gap in the superconducting state, which contrasts the assumption of the "free-spin" ground state in the superconducting state. Moreover, a narrow dip on top of the broad peak is observed, highlighted by the blue box in Fig. 6.8(b). A more detailed spectrum of this dip around the Fermi level is shown in Fig. 6.8(c). A broad zero-bias resonance superimposed with a narrow dip has been observed on impurities with spins $S > 1/2$ and were explained by a second Kondo screening channel with a considerably lower Kondo temperature [198]. A second possibility, which is more likely to account for the present case, is related to inelastic excitations that lead to a pair of conductance steps symmetric around E_F. These include the excitation of molecular vibrations [199] or different spin projections in the presence of magnetic anisotropy [56]. The nature of the dip in the conductance will be investigated in section 6.6.

An understanding of the origin of the broad peak around E_F can be gained from its temperature dependence (cf. Eq. (3.5)). dI/dV spectra of an exemplary MnPc-NH_3 molecule were recorded at different temperatures up to 36.2 K. The experimental spectra are shown in Fig. 6.9(a). Already

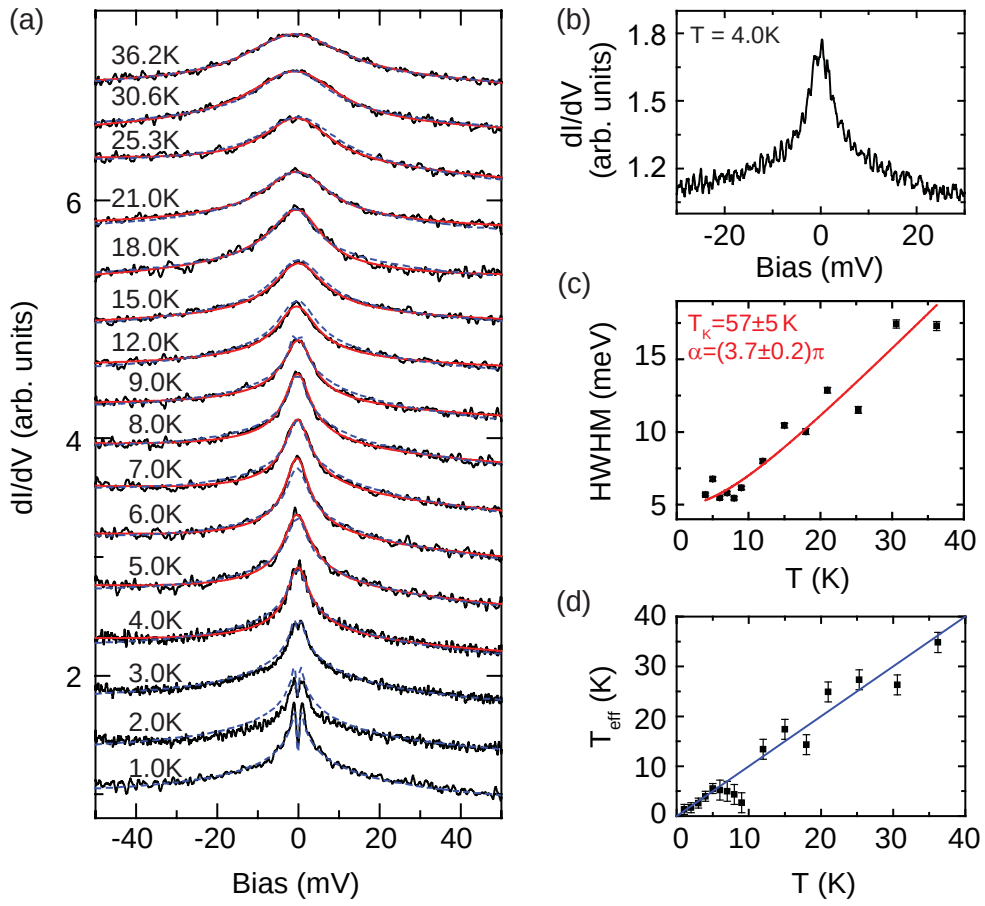

Figure 6.9: (a) $\mathrm{d}I/\mathrm{d}V$ spectra recorded on MnPc-NH_3 measured with a Au tip at different temperatures in a magnetic field of B=100 mT (spectra offset for clarity). Temperatures are given in the graph. Red lines are best fits with a Fano-Frota transmission function convoluted with the derivative of a Fermi-Dirac distribution. The blue dashed lines are best fits to the data with a scattering approach used in [101, 102]. Feedback opened at V_{bias}=50 mV, I_{tunnel}=200 pA and a bias modulation of V_{rms}=0.5 mV. (b) $\mathrm{d}I/\mathrm{d}V$ spectrum at 4 K, where the dip around E_F is absent due to thermal broadening. (c) Half-width at half maximum (HWHM) extracted from the best fits of the Fano-Frota functions in (a) plotted as a function of temperature. The red line is a fit of the temperature dependence of the Kondo resonance in the strong coupling regime with α as free fit parameter. The obtained fit parameters are given in the graph. (d) Extracted effective temperatures from fits of the scattering model to (a). The identity line is shown in blue.

at 4.0 K, the narrow dip can not be resolved anymore, probably due to thermal broadening. A single peak remains, centered around E_F [Fig. 6.9(b)]. The broadening of the resonance with increasing temperature is clearly visible in the experimental data. In order to disentangle the

intrinsic width of the Kondo resonance and the thermal broadening of the tip states, the spectra were fitted by a convolution of a Fano-Frota transmission function (cf. Eq. (3.9)), convolved with the derivative of the Fermi-Dirac distribution at the experimental temperature.

The red lines in Fig. 6.9(a) are the results of the best fits to the data from 4 K to 36.2 K. Spectra at lower temperatures can not be captured within this model due to the dip around E_F. From these fits, the HWHM of the Fano-Frota resonance is extracted and plotted as a function of the temperature T in Fig. 6.9(c). For an impurity with a spin of 1/2, which is strongly coupled to the electron bath in the substrate ($T_K \gg T$), the HWHM of the Kondo resonance follows the relation given in Eq. (3.5):

$$\mathrm{HWHM} = \frac{1}{2}\sqrt{(\alpha k_B T)^2 + (2k_B T_K)^2}. \tag{6.4}$$

A fit of this function to the experimental data with α and the Kondo temperature T_K as fit parameters results in T_K=(57±5) K and α=(3.7±0.2) π. Such a high value of the Kondo temperature indicates a complete screening of one channel of the impurity spin, thus reducing the total spin by 1/2. This result suggests that the many-body ground state of MnPc-NH_3 on Pb is the "Kondo-screened" state, strongly contradicting the findings for the system based on the analysis of the Shiba states in the superconducting state. However, the strong coupling regime Kondo regime is described by Fermi liquid theory [200, 201]. In this case, the temperature dependence of the width of the Kondo resonance is modeled using α=2π [86]. The deviation to larger values in the present case is a sign that the system is not in the strong coupling regime and an estimation of T_K within this framework is erroneous [101].

A different interpretation of the temperature dependence of the zero-bias peak can be given within a perturbative approach based on a model by Anderson and Appelbaum [98–102]. This model is introduced in section 3.2.2. It accounts for localized impurities that couple weakly to the electron bath in the sample. It includes spin exchange interactions up to third order effects. In this case, a logarithmic zero-bias resonance is found, which has no intrinsic width but only scales with the temperature. The model can be applied to systems with $S \geq 1$. Magnetic anisotropy in these systems is included by the spin Hamiltonian, introduced in 3.1. This leads to steps in the conductance, which have a peak-like shape due to third order processes.

The perturbative model is implemented in a fit routine by Markus Ternes. Fits to the experimental data are shown as blue dashed lines in Fig. 6.9(a). With an impurity spin of $S = 1$ and easy-axis anisotropy $D = -0.4$ meV, the model reproduces the $\mathrm{d}I/\mathrm{d}V$-signal reasonably well. Even $\mathrm{d}I/\mathrm{d}V$ spectra at temperatures below 4 K are described reasonably well within this model. There, the dip is a result of the axial anisotropy that was assumed. The fit parameters in the model are a constant background conductance, a linear background slope and the experimental temperature T_{eff}. We restricted the exchange coupling constant to $J\rho_0$=-0.235. The extracted temperatures T_{eff} are plotted as a function of the experimental temperature T in Fig. 6.9(d). The identity T_{eff}=T, shown in blue, confirms the good agreement of the model with the experimental data. A systematic deviation from the expected behavior is found for temperatures from 5 K to 9 K, where T_{eff} decreases with increasing temperature. The reason for this deviation could be due to the thermal broadening of the dip shape, which changes the spectral appearance of the peak. However, the true origin of this deviation is unclear. Throughout the large temperature range,

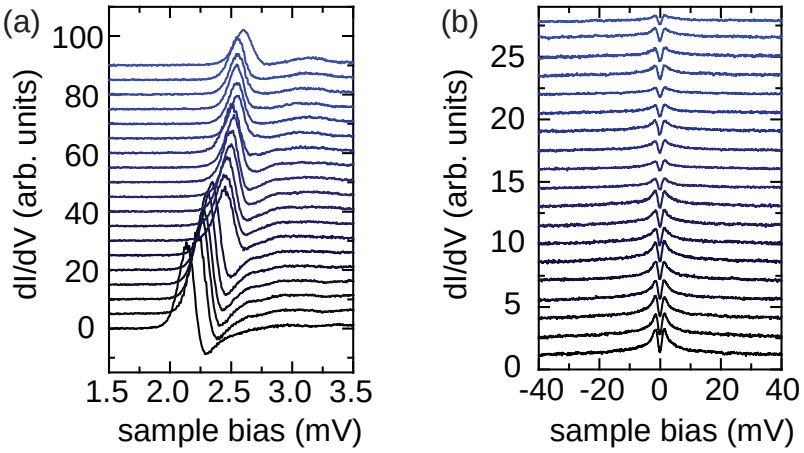

Figure 6.10: (a) dI/dV spectra of different MnPc-NH_3 molecules at 1.1 K sorted with decreasing Shiba state energies from top to bottom (Spectra offset for clarity). Feedback opened at V_{bias}=5 mV and I_{tunnel}=200 pA. (b) dI/dV spectra in a larger energy range of the same MnPc-NH_3 molecules as in (a), but at a magnetic field of B =2.7 T. Feedback opened at V_{bias}=50 mV and I_{tunnel}=200 pA.

the extracted fit results are in agreement with the expected behavior. Therefore, we conclude that the perturbative model gives an accurate description of the system. However, the large exchange coupling constant of $J\rho_0$=-0.235 indicates that the system is at the limit of the perturbative approach [102, 194]. Due to the good agreement of the model, we exclude a Kondo screening of the impurity spin. These results further support the assumption of the "free-spin" ground state in MnPc-NH_3 on Pb(111).

6.5 Comparison of the Shiba States to the Zero-Bias Resonance

As the spectra in the normal state are performed with a Au tip, Shiba states in the superconducting gap are broadened according to the Fermi-Dirac statistics. Here, we use a superconducting tip and correlate the Shiba state energies with the zero-bias resonance, measured in a magnetic field of 2.7 T. Fig. 6.10(a) shows dI/dV spectra of different MnPc-NH_3 molecules in the superconducting state. All spectra are measured at a temperature of 1.1 K. The spectra are ordered according to the Shiba state energy, decreasing from top to bottom. In Fig. 6.10(b), spectra in a larger energy range on the respective MnPc-NH_3 molecules are shown. The superconductivity was quenched in a magnetic field of B =2.7 T. When we compare the Shiba state energies with the intensity of the Kondo resonance, we directly notice that the intensity of the Kondo resonance is largest for MnPc-NH_3 with Shiba states deeper inside the gap. This can be related to the exchange coupling strength: for a relatively strong coupling, the Shiba states are at low energies. At the same time, a strong exchange coupling leads to strong third order contributions, which is manifested by a more intense zero-bias resonance. With decreasing exchange coupling strength,

the Shiba states shift to higher energies inside the superconducting gap and the intensity of the zero-bias resonance in the normal state decreases. In the topmost spectrum in Fig. 6.10(b), almost no resonance is observed anymore. Only the dip around the Fermi level is present. The correlation of the Shiba states with the Kondo resonance is in qualitative agreement with the predicted behavior [52, 119, 121].

In the following, we will investigate the origin of the dip around E_F observed in the dI/dV spectra in the normal state. A magnetic origin can be revealed by a characteristic shift in a magnetic field.

6.6 Magnetic-Anisotropy Split Kondo Resonance

Up to this point, the information gained about the system of MnPc-NH_3 on Pb(111) showed evidence that ammonia induces an electronic decoupling from the substrate, which reduces the exchange coupling strength to the substrate electrons. This was seen by Shiba states at positive energies in the superconducting state as well as an indication of a weakly coupled Kondo effect in the normal state. One open issue up to now is the origin of the dip at zero bias in the normal state.

This zero-bias dip overlaps with the zero-bias peak observed in spectra on MnPc-NH_3 (cf. Fig. 6.8). Inelastic excitations of molecular vibrations can account for a pair of steps symmetric around the Fermi level. However, internal vibrations of ammonia are at energies higher than 139 meV [190, 202]. Vibrations of porphyrines with axial ligands also require energies $\geq$30 meV [203, 204]. The low energy scale of the steps thus suggests magnetic spin excitations to be the origin. In order to prove this point, we performed measurements in different magnetic fields.

Experimental and theoretical studies on paramagnetic Kondo impurities with $S \geq 1$ found a splitting of the zero-bias Kondo resonance due to magnetic anisotropy [205, 206]. To observe this effect, the splitting of the impurity spin projections has to be in the order of the Kondo energy scale. This prerequisite is fulfilled in the system of MnPc-NH_3 on Pb(111) due to the weak exchange coupling strength.

We performed measurements in magnetic fields up to 3 T perpendicular to the surface. dI/dV spectra on the same molecule as in Fig. 6.9 at different magnetic fields are shown in Fig. 6.11(a). With increasing magnetic fields, the dip around the Fermi level evolves into two symmetric steps around E_F with a flat conductance base at low energies. The evolution of the spectroscopic feature in a magnetic field confirms its magnetic origin. A fit of two Fermi-Dirac step functions symmetric around E_F is shown by the red lines in Fig. 6.11(a), where the step energy E_{step} as well as the step width and the intensity are free fit parameters. The step energy E_{step} increases linearly with the magnetic field, as shown in Fig. 6.11(b). This particular dependence of the step energy on the magnetic field, combined with the sizable splitting even at fields close to zero can be explained by magnetic anisotropy.

As shown in section 3.1.2, in the presence of axial anisotropy D and transverse anisotropy E, the spin Hamiltonian (3.1) leads to a splitting of a spin 1 into three levels. The levels can be

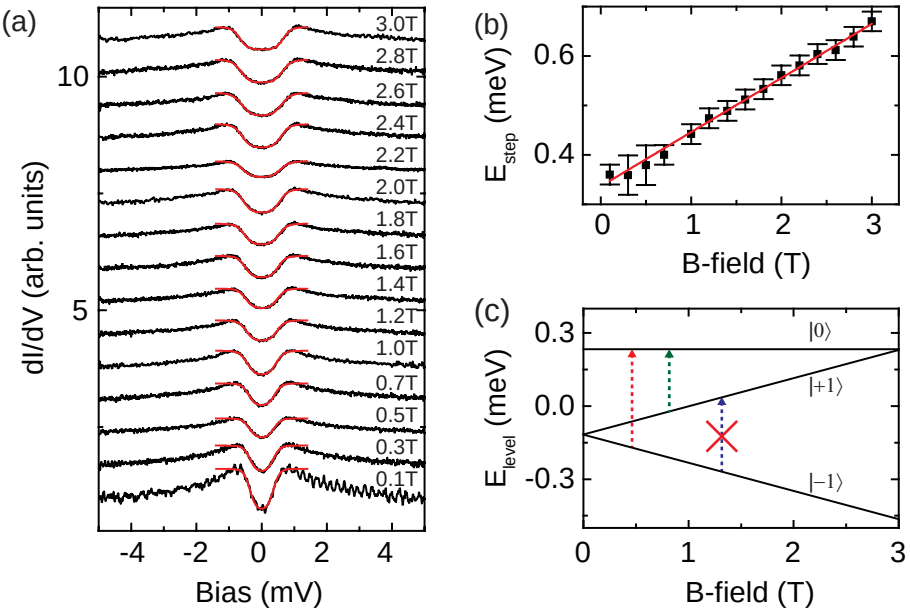

Figure 6.11: (a) $\mathrm{d}I/\mathrm{d}V$ spectra on MnPc-NH_3 in different magnetic fields (spectra offset for clarity). Spectra are shown as black lines. Fits of a pair of steps symmetric around E_F are shown as red lines. Feedback is opened for spectra: V_bias=5 mV, I_tunnel=200 pA and V_rms=50μeV. (b) Step energy E_step obtained from fits to spectra in (a) as a function of the magnetic field (dots). A fit of the model proposed in Eq. (6.11) indicates the process is an excitation of a spin 1 system from $|-1\rangle$ to $|0\rangle$. (c) Simulated energy level shift of the eigenstates of the spin projections in a spin 1 system in the presence of longitudinal D anisotropy. Allowed and forbidden excitations from the ground state to excited states with different spin quantum number m_S are indicated by the red and blue arrows.

obtained by diagonalizing the spin Hamiltonian and are given as [174]:

$$|\chi_-\rangle = \sin\gamma\,|1\rangle - \cos\gamma\,|-1\rangle \tag{6.5}$$
$$|\chi_+\rangle = \cos\gamma\,|1\rangle + \sin\gamma\,|-1\rangle \tag{6.6}$$
$$|\chi_0\rangle = |0\rangle \tag{6.7}$$

and their energies are

$$E_{\chi_-} = \frac{D}{3} - \sqrt{E^2 + (g\mu_\mathrm{B}B_\mathrm{z})^2} \tag{6.8}$$
$$E_{\chi_+} = \frac{D}{3} + \sqrt{E^2 + (g\mu_\mathrm{B}B_\mathrm{z})^2} \tag{6.9}$$
$$E_{\chi_0} = -\frac{2D}{3}. \tag{6.10}$$

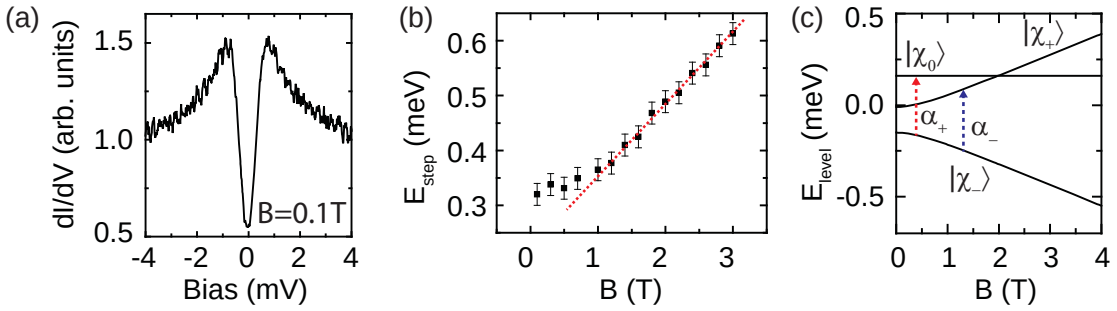

Figure 6.12: (a) dI/dV spectrum of a MnPc-NH_3 molecule where one step can be identified. The red curve is a fit of two pairs of symmetric steps at $\pm(0.22\pm0.05)$ meV and $\pm(0.45\pm0.05)$ meV. Feedback opened at V_{bias}=5 mV, I_{tunnel}=200 pA, B=0.1 T. (b) Evolution of eigenstates in a magnetic field for a system with $S = 1$ in the presence of D and E anisotropy. Values in the model are D=−0.24 meV, E=0.07 meV and g=2. (c) Step energies E_{step} plotted as a function of magnetic field. The red dashed line shows the regime where the step energy depends linearly on the magnetic field.

Neglecting transverse anisotropy for the moment ($E = 0$), the states $|\chi_-\rangle$ and $|\chi_+\rangle$ simplify to the original projections along the z-axis, $|+1\rangle$ and $|-1\rangle$, respectively. In a system with easy-axis anisotropy ($D < 0$), they form the ground state. The state $|0\rangle$ is at an energy D above the ground state. In a magnetic field, $|+1\rangle$ and $|-1\rangle$ start to split linearly with the applied field, whereas $|0\rangle$ does not shift [Fig. 6.11(c)]. Only transitions from $|-1\rangle$ to $|0\rangle$ (red arrow in Fig. 6.11(c)) and from $|+1\rangle$ to $|0\rangle$ (green arrow) are allowed. However, in a magnetic field, a finite temperature is required to thermally occupy $|+1\rangle$. The transition from $|-1\rangle$ to $|+1\rangle$ (blue arrow) is forbidden due to the selection rules for spin transitions, Δm_S=±1.

The linear shift of the step energy as a function of B (shown in Fig. 6.11(b)) agrees with the model for uniaxial anisotropy and an excitation from $|-1\rangle$ to $|0\rangle$. The excitation energy in a magnetic field is given as

$$E_{step} = -D + g\mu_B B_z. \tag{6.11}$$

A fit of the model to the data in Fig. 6.11(b) yields a g-factor of 1.89±0.04 and a uniaxial anisotropy of D=-0.34±0.01 meV. Note, that for positive D, two excitations from $|0\rangle$ to $|-1\rangle$ and $|+1\rangle$ are allowed. This is not seen here.

We find evidence for transverse magnetic anisotropy E in the shift of even a single pair of conductance steps. In Fig. 6.12(a), the dI/dV spectrum of one MnPc-NH_3 is shown, where only one step can be resolved. However, when we study the evolution of the step energy in a magnetic field, we find a deviation from the linear dependence at low magnetic fields, as indicated in Fig. 6.12(b). To understand this behavior, an illustration of the spin state levels in the case of easy-axis anisotropy and a finite transverse anisotropy is shown in Fig. 6.12(c). The transitions between the spin levels are indicated as α_- in blue and α_+ in red. The characteristic behavior observed in Fig. 6.12(b) is reminiscent of the transition from $|\chi_-\rangle$ to $|\chi_0\rangle$ in Fig. 6.12(c). The energy of this transition is

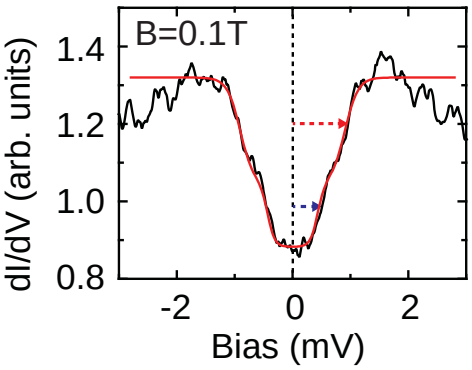

Figure 6.13: dI/dV spectrum of one MnPc-NH_3 molecule, which exhibits two steps in the differential conductance. A fit of two pairs of steps around E_F is shown in red. The two inelastic excitations are indicated by blue and red arrows. Feedback opened at V_{bias}=5 mV and I_{tunnel}=200 pA

$$E_{\chi_0} - E_{\chi_-} = -D + \sqrt{E^2 + (g\mu_B B_z)^2}. \tag{6.12}$$

A finite E enables transitions from $|\chi_-\rangle$ to $|\chi_+\rangle$ and $|\chi_-\rangle$ to $|\chi_0\rangle$. At large fields, the red line in Fig. 6.12(b) shows the linear shift of the step energy with the B-field. At low magnetic fields, where B is comparable to E, a deviation from the linear dependence is observed. The question why only one step is evident in the dI/dV spectra arises naturally. One explanation may be due to similar excitation energies. For small magnetic anisotropies, thermal occupation of excited levels play a significant role. For small values of E and finite temperatures, $|\chi_+\rangle$ is thermally populated and the transition from $|\chi_+\rangle$ to $|\chi_0\rangle$ can be excited by tunneling electrons. This excitation has almost the same energy as the excitation α_+, thus the two steps overlap in the spectra. The third possible excitation, α_- is at low energies and hardly detectable. When the magnetic field is increased, $|\chi_+\rangle$ shifts up in energy. The level becomes less occupied and the excitation energy α_- is increased. However, at the same time, the two states $|\chi_-\rangle$ and $|\chi_+\rangle$ become more spin polarized towards the original states $|-1\rangle$ and $|+1\rangle$. Therefore, the transition rates between these two states decrease and the excitation α_+ prevails.

Another MnPc-NH_3 molecule, shown in Fig. 6.13, exhibits two steps in the differential conductance. We believe the two steps correspond to inelastic spin excitations, which can be resolved in this case. From their step energies at $\pm(0.22\pm0.05)$ meV and $\pm(0.45\pm0.05)$ meV, we extract magnetic anisotropies of E=(0.11±0.03) meV and D=(-0.34±0.07) meV. Here, $E \approx D/3$ and thus is close to a change of the main anisotropy axis. These values are comparable to the anisotropies obtained from the Shiba state splitting in the superconducting state (cf. section 6.3.2).

In conclusion, we can attribute the steps in the conductance around E_F to inelastic spin excitations of the anisotropy-split levels in MnPc-NH_3. The behavior of the steps agrees with an easy-axis anisotropy and the presence of transverse anisotropy. Where parameters of the anisotropies could be determined, they agree with the values observed from the Shiba state splitting. These results support the assumption of a "free-spin" ground state of MnPc-NH_3 on Pb(111) with a spin of 1. A more detailed analysis of the anisotropies on the basis of only one conductance step requires a more complex model, which includes the transition rates between states as well as their thermal occupations.

6.7 Summary and Conclusions

In this chapter, we investigated the influence of an axial ligand adsorbed on manganese phthalocyanine on Pb(111). Ammonia (NH_3) was chosen as it does not change the oxidation state of the metal ion in the complex. Adsorption of ammonia leads to a homogeneous coverage with one ammonia molecule per MnPc, which could be desorbed by a tip-induced voltage pulse. In this way, we could confirm the reversibility of the ammonia-induced change of the properties of MnPc.

At 1.1 K, one pair of Shiba states was found on MnPc-NH_3, with the high intensity component at positive energy. An increase in temperature up to 4.5 K revealed additional Shiba states deeper inside the superconducting gap. From an analysis of the number of Shiba states, their energies and their intensities, we could determine the many-body ground state of the system. We found all MnPc-NH_3 molecules to be in the "free spin" ground state, carrying a spin of $S = 1$. The effect of ammonia can be attributed to an electronic decoupling of the Mn ion from the substrate, thus weakening the exchange coupling strength.

Low-intensity resonances were found at energies outside the superconducting gap on MnPc-NH_3. A quantitative analysis of these resonances is difficult, but their qualitative behavior suggests that they arise from inelastic spin-flip excitations involving different spin levels.

The weak exchange coupling of MnPc-NH_3 was further supported by measurements in the normal state, where the superconductivity was quenched in a magnetic field. We found a broad zero-bias resonance and a narrow dip at E_F. The zero-bias resonance shows a temperature dependence indicating a weak exchange coupling strength between the impurity spin and the electron bath in the substrate. In this case, no Kondo singlet is formed and the impurity spin is essentially unscreened. The dip was identified as inelastic spin-flip excitations to higher spin levels, in agreement with the anisotropies obtained from the Shiba state splitting.

The present findings open a way to tune the properties of a metal-organic molecule on a superconducting substrate. The immediate environment of the metal ion plays a crucial role on its properties such as magnetic anisotropy as well as the coupling strength to its surrounding. The sensitivity of the Shiba states on these changes can be exploited in systems ranging from gas sensing devices to the fabrication of coupled structures, where Majorana modes can be created.

Chapter 7

Summary and Conclusions

In this thesis, we presented studies of fundamental properties of molecules on surfaces. The motivation for such studies is to get a better understanding of processes taking place in single-molecule reactions, such as molecular switching. Moreover, the spin state of molecules adsorbed on surfaces can be used for information storage devices. Fundamental knowledge about the interactions of spins with the underlying substrate can help to tune these properties in order to design bistable spin systems. To investigate the local properties of such systems, scanning tunneling microscopy and spectroscopy were used.

The first experiment, presented in chapter 4, dealt with the tip-induced ring-closing reaction of *4,4'-(4,4'-(perfluorocyclopent-1-ene-1,2-diyl)bis(5-methylthiophene-4,2-diyl)dipyridine* (PDTE) on the Ag(111) surface. STM measurements were combined with density functional theory (DFT) calculations, performed in the group of Peter Saalfrank at the university of Potsdam. We deposited the ring-open form of PDTE, which resulted in an arrangement in ordered molecular islands, where all molecules had the same appearance. A structural change of individual PDTE molecules could be induced by a voltage pulse by the STM tip. This also led to a change in the electronic structure around the Fermi level. At negative energies, states appeared below $-1\,\mathrm{V}$ that were not present in the initial form. In complementary DFT calculations, four possible PDTE isomers on Ag(111) were considered and their adsorption energies and thermal stabilities were calculated. Two isomers were identified to be the most stable on the surface: the ring-open form in a flat configuration and the ring-closed form also flat on the surface, but with both methyl groups pointing away from the surface. The strong influence of dispersion interactions on the isomer stability is highlighted by the calculations. This shows that the surface has a large impact on the switching reaction, as certain isomers can not be stabilized on the substrate. Furthermore, the site-projected density of states was calculated and a comparison to the experimental spectra led to the assignment of the open form as initial isomer. The tip-induced change corresponds to the ring-closing reaction into the flat *cis*-configuration. It is worthy to point out that the reduction of the HOMO-LUMO gap observed in $\mathrm{d}I/\mathrm{d}V$ spectra and in the calculated DOS is in agreement with observations of transport properties in these PDTE molecules. In the ring-closed form, the conjugated π-electron system results in a higher conductivity compared to the open form. This

confirms the successful ring-closing reaction induced by the STM tip. On Ag(111), we could not induce a back reaction with the STM tip.

The switching mechanism was investigated by distance-dependent measurements of the threshold voltage at which the switching occurs. A linear dependence on the distance, combined with a minimal switching threshold at the onset of the LUMO suggests a combination of an electric-field induced switching mechanism with a contribution of tunneling electrons. Interestingly, the calculations of the reaction barriers for a direct reaction from the open flat isomer to the closed *cis*-isomer predict a large activation barrier. Nonetheless, the calculated rates for a thermal back reaction show that the closed *cis*-isomer is the only configuration that does not switch back to the open isomer, as an effect of the stabilization by the surface. Taking into account the electric field, the calculation implies the lowering of the reaction barrier for an erection of the ring open form. It is conceivable that the reaction proceeds in a two-step process, which involves an erected intermediate geometry, in which the ring-closing reaction takes place.

In a second experiment, paramagnetic manganese phthalocyanine (MnPc) molecules were studied on the superconducting Pb(111) surface in chapter 5. The aim of this study was to characterize the interaction of the magnetic metal-organic molecule with the quasiparticles in the substrate. At 1.2 K, we observed triplets of Shiba states on MnPc as a manifestation of the exchange coupling between the adsorbate spin and the superconducting quasiparticles. The formation of large molecular islands provided many different adsorption sites of MnPc on Pb(111), which enabled the study of a large range of exchange coupling strengths. A collective shift of the Shiba states was observed, depending on the adsorption site. At a certain point, the high-intensity component of the Shiba states crossed the Fermi level, which was assigned to a phase transition of the system towards a different ground state. An analysis of the relative Shiba state intensities within the triplets was used to assign the ground state of the system. Shiba states at negative energies exhibited equal relative intensities, whereas Shiba triplets at positive energies had different intensities. We found the origin of the Shiba state splitting to be due to magnetic anisotropy, which lifts the degeneracy of different spin states. In this case, equal intensities of Shiba states correspond to excitations from a single ground state level to an excited state, which is split in the presence of magnetic anisotropy. An excitation from a ground state with $S = 1/2$ to an excited state with $S = 1$ yields three Shiba states. On the other hand, the intensities of the Shiba states at positive energies were found to depend on their energy splitting and followed a Boltzmann distribution. Therefore, in this ground state the spin was assigned to be $S = 1$. There, Shiba states correspond to an excitation from thermally occupied ground state levels into an excited state with $S = 1/2$.

In the experiments, the organic ligand had two effects on the system. Firstly, different adsorption sites were provided by the intermolecular interactions leading to the formation of islands. Secondly, the magnetic anisotropy caused a splitting of the spin states and therefore the splitting of the Shiba states. These properties can be used to engineer systems with tunable exchange coupling strengths as well as the spin state, which results in a different number of Shiba states. There is an increasing interest stemming from the research of Majorana modes, which can be created by a specific configuration of Shiba bands in arrangements of impurities on superconductors. Moreover, Shiba states allow a precise observation of the effects at play. Slight changes in their energy and splitting can be directly correlated to the exchange coupling and anisotropy.

In the last experiment (chapter 6), we tried to alter the interaction of MnPc with the underlying Pb(111) substrate by adsorbing ammonia as an axial ligand. We could confirm the successful adsorption of ammonia by a change of the appearance of the respective MnPc molecules. Furthermore, a tip-induced desorption restored the initial MnPc molecules. In contrast to MnPc on Pb(111), all MnPc-NH_3 molecules exhibited Shiba states with higher spectral intensity at positive energies. At 1.1 K, only one Shiba state could be resolved. These two observations were associated with a reduction of the exchange coupling strength with the superconducting quasiparticles. Temperature-dependent measurements confirmed a thermal occupation of anisotropy-split ground state levels. At 4 K, up to three Shiba states were observed with different relative intensities. This finding is of particular interest, as it seems that ammonia adsorption does not change the spin state of the system but only reduces the strength of the exchange coupling with the substrate and affects the magnetic anisotropies. We could therefore assign a spin of $S = 1$ to the ground state, the same found for weakly coupled MnPc. Along with Shiba states, small resonances were found outside the superconducting gap on MnPc-NH_3 molecules that exhibited the weakest coupling to the substrate (Shiba states close to the gap edge). A possible explanation connects these features to inelastic spin excitations of the spin-1 ground state levels.

In a magnetic field, the superconductivity was quenched and we investigated the normal-state properties. A broad zero-bias peak superimposed by a narrow dip is present at the Fermi level. The specific temperature dependence of the resonance could not be modeled using the Fermi liquid approach for a strong coupling Kondo effect. Better agreement was found using a model based on a perturbative approach to treat weak Kondo correlations. This is another indication that MnPc-NH_3 is in the "free spin" ground state. In this weak coupling regime, no Kondo temperature can be assigned to the system, as the measurement temperature is in the range of the Kondo temperature. However, the dip superimposed on the broad peak was found to evolve into symmetric steps in a magnetic field. This suggests that the steps are caused by inelastic spin excitations. The shift of these steps with the magnetic field showed a behavior reminiscent of a spin $S = 1$ system, in agreement with the measurements in the superconducting state. From the appearance of the inelastic excitations, we conclude that the energy scale of the Kondo temperature is smaller than the magnetic anisotropies in the system. Otherwise, the width of the Kondo resonance would be larger than the anisotropy splitting and no dip could be observed.

With this experiment, we were able to show that the exchange coupling of a magnetic impurity with a superconductor can be changed by coordination of an additional ligand, in our case ammonia.

The results presented in this thesis show the importance of a proper understanding of the properties of molecules on surfaces. Switching of individual molecules that are directly attached to a metal substrate is a key ingredient for their use in electronic devices. However, in order to create actual devices, the reversibility of the switching is necessary. Therefore, the switching mechanism needs to be understood in more detail. Additionally, the role of the supporting substrate plays a role in the switching. A thin insulating layer could provide a sufficient decoupling of the switching unit from the substrate in order to study the effect of the STM tip and the current as well as the electric field on the switching. Molecular switches will have to be integrated into circuits and therefore contacted to external leads. A proper choice of those leads can provide a sufficient decoupling from the substrate and restore full functionality.

Equally important as the influence of the surface on molecular switching is the influence of a substrate on the spin state of a magnetic molecule adsorbed on it. Superconductors have shown to be precise indicators of the effect, the local environment plays for the magnetic anisotropy and therefore the spin state. Axial ligands seem to be viable candidates to tune the magnetic properties. Improving the control of the molecular environment has additional advantages. To realize systems with two stable spin states, the magnetic anisotropy barrier needs to be drastically increased. The study in this thesis indicate one possible direction in which to investigate further. Different axial ligands can lead to surprising new results. At the same time, the study of magnetic impurities reveals information about the nature of superconductivity itself. In this respect, one approach can be the use of magnetic molecules to functionalize superconductors, with for example a magnetic surface and a superconducting bulk. Further studies with improved experimental methods can lead to a fast progress of the understanding of fundamental properties of molecules on surfaces. This understanding will show ways to successfully use single molecules in electronic devices.

Appendix I

Numerical Deconvolution Procedure for Shiba State Determination

In order to obtain the binding energy E_b and the spectral intensity of the Shiba states, $\mathrm{d}I/\mathrm{d}V$-spectra were treated with the program SpectraFox [207]. It has a built-in function to deconvolute the influence of the superconducting tip on the obtained tunneling spectra. All spectra are acquired in the weak tunneling regime, which indicates the system to be in the single-electron tunneling regime and the spectral weight is proportional to the intensity of the Shiba states [118].

The experimental data are fitted by a convolution of the tip DOS with the sample DOS, where we make several assumptions about the states in the tip and sample. We calculate the tunneling current using the known expression

$$I_\mathrm{t}(V_\mathrm{bias}) \approx \int_{-\infty}^{\infty} \mathrm{d}E \; \rho_\mathrm{tip}(E+i\varepsilon,T)\,\rho_\mathrm{sample}(E+i\varepsilon+eV_\mathrm{bias},T)\,[f(E,T)-f(E+eV_\mathrm{bias},T)]\,|M_\mathrm{s,t}|^2 \;, \tag{I.1}$$

where $f(E,T)$ is the Fermi-Dirac distribution as a function of the energy E and the temperature T. For bias voltages of only a few meV as applied in the experiments, the approximation of a constant tunnel matrix element $M_\mathrm{s,t}$ is reasonable.

As the tip is covered with superconducting Pb, its density of states, ρ_tip, is that of a BCS superconductor with the superconducting gap parameter Δ_tip. Finite lifetime effects lead to a broadening of the coherence peaks, which are taken into account by an imaginary energy term $i\varepsilon$ [169, 208].

On MnPc as well as MnPc-NH_3, no BCS peaks at the gap edge are observed in $\mathrm{d}I/\mathrm{d}V$-spectra. This is due to the depletion of the BCS density of states upon the formation of Bogoliubov-de Gennes quasiparticle excitations inside the superconducting gap [116]. Consequently, the density of states of the substrate ρ_sample is modeled with symmetric step functions at $\pm\Delta_\mathrm{sample}$ to account for the superconducting gap. The Shiba states are described by Lorentzian peaks at energies $\pm E_{\mathrm{b},i}$ and have widths (Γ_i) and areas (A_i). The latter parameters are independent of each other. However, at equal peak area, a larger width of a peak is related to a smaller peak height. The

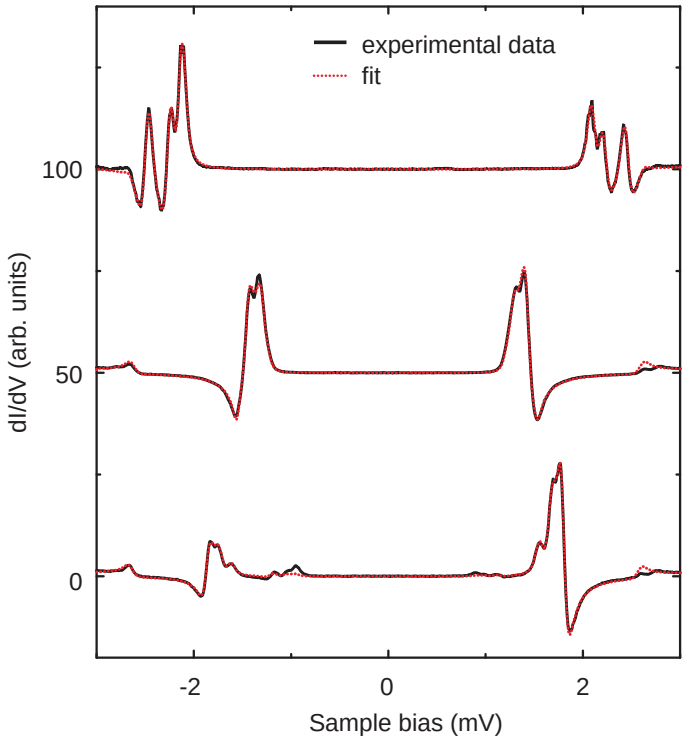

Figure I.1: Experimental dI/dV-spectra and their fits (red dashed lines) obtained with the deconvolution procedure: spectra I, II, and III of Fig. 5.4(b). Reprinted from [124].

density of states of the substrate thus reads:

$$\rho_{\mathrm{sample}}(E) = C\left[3 - \frac{1}{1+\exp\left(\frac{E-\Delta_{\mathrm{sample}}}{w}\right)} + \frac{1}{1+\exp\left(\frac{E+\Delta_{\mathrm{sample}}}{w}\right)}\right] + \sum_{i=1}^{3}\frac{2A_i}{\pi}\left(\frac{\Gamma_i}{4(E-E_{bi})^2+\Gamma_i^2} + R\,\frac{\Gamma_i}{4(E+E_{bi})^2+\Gamma_i^2}\right). \tag{I.2}$$

Here, C is the amplitude of the step function and w its width. The ratio R accounts for the height asymmetry of the Lorentzian peaks at positive and negative bias, respectively. The tunneling current $I_{\mathrm{t}}(V_{\mathrm{bias}})$ is calculated using the assumed density of states of the tip and the sample and a numerical derivative of it is fitted to the experimental data.

Some experimental spectra on MnPc/Pb(111) and their fits are shown in Fig. I.1. These correspond to the three spectra I, II and III of Fig. 5.4(b). The fits reproduce the experimental spectra very well besides some deviations of the height of the *thermal* resonances at $eV = \pm(\Delta_{\mathrm{tip}} - |E_{\mathrm{b},i}|)$, most prominent in spectrum III.

References

[1] The Nobel Prize in Chemistry 2016 (2016). URL `https://www.nobelprize.org/nobel_prizes/chemistry/laureates/2016/`. Visited: 10/22/2016.

[2] Kudernac, T., Ruangsupapichat, N., Parschau, M., Macia, B., Katsonis, N., Harutyunyan, S. R., Ernst, K.-H. & Feringa, B. L. Electrically driven directional motion of a four-wheeled molecule on a metal surface. *Nature* **479**, 208–211 (2011).

[3] Aviram, A. & Ratner, M. A. Molecular rectifiers. *Chemical Physics Letters* **29**, 277–283 (1974).

[4] Song, H., Kim, Y., Jang, Y. H., Jeong, H., Reed, M. A. & Lee, T. Observation of molecular orbital gating. *Nature* **462**, 1039–1043 (2009).

[5] Fuechsle, M. *et al.* A single-atom transistor. *Nat Nano* **7**, 242–246 (2012).

[6] Green, J. E. *et al.* A 160-kilobit molecular electronic memory patterned at 1011 bits per square centimetre. *Nature* **445**, 414–417 (2007).

[7] Cuevas, J.-C. & Scheer, E. *Molecular Electronics: An Introduction to Theory and Experiment*, vol. 1 of *Nanoscience and Nanotechnology* (World Scientific, 2010).

[8] David, L. SpaceX Founder Set to Unveil Humans-to-Mars Plan in September (2016). URL `https://www.scientificamerican.com/article/spacex-founder-set-to-unveil-humans-to-mars-plan-in-september/`. Visited: 10/22/2016.

[9] von Hippel, A. Molecular Engineering. *Science* **123**, 315 (1956).

[10] Zhang, J. L., Zhong, J. Q., Lin, J. D., Hu, W. P., Wu, K., Xu, G. Q., Wee, A. T. S. & Chen, W. Towards single molecule switches. *Chemical Society Reviews* **44**, 2998–3022 (2015).

[11] Koumura, N., Zijlstra, R. W. J., van Delden, R. A., Harada, N. & Feringa, B. L. Light-driven monodirectional molecular rotor. *Nature* **401**, 152–155 (1999).

[12] Fletcher, S. P., Dumur, F., Pollard, M. M. & Feringa, B. L. A Reversible, Unidirectional Molecular Rotary Motor Driven by Chemical Energy. *Science* **310**, 80 (2005).

[13] Perera, U. G. E. *et al.* Controlled clockwise and anticlockwise rotational switching of a molecular motor. *Nat Nano* **8**, 46–51 (2013).

[14] Kudernac, T., van der Molen, S. J., van Wees, B. J. & Feringa, B. L. Uni- and bi-directional light-induced switching of diarylethenes on gold nanoparticles. *Chemical Communications* 3597–3599 (2006).

[15] Alemani, M., Peters, M., Hecht, S., Rieder, K.-H., Moresco, F. & Grill, L. Electric Field-Induced Isomerization of Azobenzene by STM. *Journal of the American Chemical Society* **128**, 14446–14447 (2006).

[16] Liljeroth, P., Repp, J. & Meyer, G. Current-Induced Hydrogen Tautomerization and Conductance Switching of Naphthalocyanine Molecules. *Science* **317**, 1203 (2007).

[17] Comstock, M. J. *et al.* Reversible Photomechanical Switching of Individual Engineered Molecules at a Metallic Surface. *Physical Review Letters* **99**, 038301 (2007).

[18] Quek, S. Y., Kamenetska, M., Steigerwald, M. L., Choi, H. J., Louie, S. G., Hybertsen, M. S., NeatonJ. B. & VenkataramanLatha. Mechanically controlled binary conductance switching of a single-molecule junction. *Nat Nano* **4**, 230–234 (2009).

[19] Fernandez-Torrente, I., Monturet, S., Franke, K. J., Fraxedas, J., Lorente, N. & Pascual, J. I. Long-Range Repulsive Interaction between Molecules on a Metal Surface Induced by Charge Transfer. *Physical Review Letters* **99**, 176103 (2007).

[20] Mugarza, A. *et al.* Orbital Specific Chirality and Homochiral Self-Assembly of Achiral Molecules Induced by Charge Transfer and Spontaneous Symmetry Breaking. *Physical Review Letters* **105**, 115702 (2010).

[21] Ishii, H., Sugiyama, K., Ito, E. & Seki, K. Energy Level Alignment and Interfacial Electronic Structures at Organic/Metal and Organic/Organic Interfaces. *Advanced Materials* **11**, 605–625 (1999).

[22] van der Molen, S.J. and Liljeroth, P. Charge transport through molecular switches. *Journal of Physics: Condensed Matter* **22**, 133001 (2010).

[23] Piantek, M. *et al.* Reversing the Thermal Stability of a Molecular Switch on a Gold Surface: Ring-Opening Reaction of Nitrospiropyran. *Journal of the American Chemical Society* **131**, 12729–12735 (2009).

[24] Henzl, J., Bredow, T. & Morgenstern, K. Irreversible isomerization of the azobenzene derivate Methyl Orange on Au(111). *Chemical Physics Letters* **435**, 278–282 (2007).

[25] Binnig, G., Rohrer, H., Gerber, C. & Weibel, E. Tunneling through a controllable vacuum gap. *Applied Physics Letters* **40**, 178–180 (1982).

[26] Binnig, G., Rohrer, H., Gerber, C. & Weibel, E. Surface Studies by Scanning Tunneling Microscopy. *Physical Review Letters* **49**, 57–61 (1982).

[27] Binnig, G. & Rohrer, H. Scanning tunneling microscopy. *Surface Science* **126**, 236–244 (1983).

[28] Crommie, M. F., Lutz, C. P. & Eigler, D. M. Confinement of Electrons to Quantum Corrals on a Metal Surface. *Science* **262**, 218 (1993).

[29] Manoharan, H. C., Lutz, C. P. & Eigler, D. M. Quantum mirages formed by coherent projection of electronic structure. *Nature* **403**, 512–515 (2000).

[30] Rueß, F. J., Goh, K. E. J., Butcher, M. J., Reusch, T. C. G., Oberbeck, L., Weber, B., Hamilton, A. R. & Simmons, M. Y. Narrow, highly P-doped, planar wires in silicon created by scanning probe microscopy. *Nanotechnology* **18**, 044023 (2007).

[31] Moon, C. R., Mattos, L. S., Foster, B. K., Zeltzer, G. & Manoharan, H. C. Quantum holographic encoding in a two-dimensional electron gas. *Nat Nano* **4**, 167–172 (2009).

[32] Kalff, F. E., Rebergen, M. P., Fahrenfort, E., Girovsky, J., Toskovic, R., Lado, J. L., Fernández-Rossier, J. & Otte, A. F. A kilobyte rewritable atomic memory. *Nat Nano* **advance online publication** (2016).

[33] Shilov, A. Seagate: Hard Disk Drives Set to Stay Relevant for 20 Years (2015). URL `http://www.anandtech.com/show/9858/seagate-hard-disk-drives-set-to-stay-relevant-for-20-years`. Visited: 10/22/2016.

[34] Gambardella, P. *et al.* Giant Magnetic Anisotropy of Single Cobalt Atoms and Nanoparticles. *Science* **300**, 1130 (2003).

[35] Hirjibehedin, C. F., Lin, C.-Y., Otte, A. F., Ternes, M., Lutz, C. P., Jones, B. A. & Heinrich, A. J. Large Magnetic Anisotropy of a Single Atomic Spin Embedded in a Surface Molecular Network. *Science* **317**, 1199 (2007).

[36] Hirjibehedin, C. F., Lutz, C. P. & Heinrich, A. J. Spin Coupling in Engineered Atomic Structures. *Science* **312**, 1021–1024 (2006).

[37] Heinrich, B. W., Ahmadi, G., Müller, V. L., Braun, L., Pascual, J. I. & Franke, K. J. Change of the Magnetic Coupling of a Metal–Organic Complex with the Substrate by a Stepwise Ligand Reaction. *Nano Letters* **13**, 4840–4843 (2013).

[38] Kondo, J. Resistance Minimum in Dilute Magnetic Alloys. *Progress of Theoretical Physics* **32**, 37–49 (1964).

[39] Zhou, L., Wiebe, J., Lounis, S., Vedmedenko, E., Meier, F., Blugel, S., Dederichs, P. H. & Wiesendanger, R. Strength and directionality of surface Ruderman-Kittel-Kasuya-Yosida interaction mapped on the atomic scale. *Nat Phys* **6**, 187–191 (2010).

[40] Yan, S., Choi, D.-J., BurgessJacob A. J., Rolf-Pissarczyk, S. & Loth, S. Control of quantum magnets by atomic exchange bias. *Nat Nano* **10**, 40–45 (2015).

[41] Khajetoorians, A. A., Wiebe, J., Chilian, B. & Wiesendanger, R. Realizing All-Spin–Based Logic Operations Atom by Atom. *Science* **332**, 1062 (2011).

[42] Loth, S., Baumann, S., Lutz, C. P., Eigler, D. M. & Heinrich, A. J. Bistability in Atomic-Scale Antiferromagnets. *Science* **335**, 196 (2012).

[43] Rau, I. G. *et al.* Reaching the magnetic anisotropy limit of a 3d metal atom. *Science* **344**, 988 (2014).

[44] Yu, L. Bound State in Superconductors with Paramagnetic Impurities. *Acta Sin. Phys.* **21**, 75–91 (1965).

[45] Shiba, H. Classical Spins in Superconductors. *Progress of Theoretical Physics* **40**, 435–451 (1968).

[46] Rusinov A.I. On the theory of gapless superconductivity in alloys containing paramagnetic impurities. *Sov. Phys. JETP* **29**, 1101–1106 (1969).

[47] De Franceschi, S., Kouwenhoven, L., Schonenberger, C. & Wernsdorfer, W. Hybrid superconductor-quantum dot devices. *Nat Nano* **5**, 703–711 (2010).

[48] Pillet, J.-D., Joyez, P., Žitko, R. & Goffman, M. F. Tunneling spectroscopy of a single quantum dot coupled to a superconductor: From Kondo ridge to Andreev bound states. *Physical Review B* **88**, 045101 (2013).

[49] Yazdani, A., Jones, B. A., Lutz, C. P., Crommie, M. F. & Eigler, D. M. Probing the Local Effects of Magnetic Impurities on Superconductivity. *Science* **275**, 1767–1770 (1997).

[50] Ji, S.-H. *et al.* High-Resolution Scanning Tunneling Spectroscopy of Magnetic Impurity Induced Bound States in the Superconducting Gap of Pb Thin Films. *Physical Review Letters* **100**, 226801 (2008).

[51] Franke, K. J., Schulze, G. & Pascual, J. I. Competition of Superconducting Phenomena and Kondo Screening at the Nanoscale. *Science* **332**, 940–944 (2011).

[52] Bauer, J., Pascual, J. I. & Franke, K. J. Microscopic resolution of the interplay of Kondo screening and superconducting pairing: Mn-phthalocyanine molecules adsorbed on superconducting Pb(111). *Physical Review B* **87**, 075125 (2013).

[53] Heinrich, B. W., Braun, L., Pascual, J. I. & Franke, K. J. Protection of excited spin states by a superconducting energy gap. *Nat Phys* **9**, 765–768 (2013).

[54] Jaklevic, R. C. & Lambe, J. Molecular Vibration Spectra by Electron Tunneling. *Physical Review Letters* **17**, 1139–1140 (1966).

[55] Stipe, B. C., Rezaei, M. A. & Ho, W. Single-Molecule Vibrational Spectroscopy and Microscopy. *Science* **280**, 1732–1735 (1998).

[56] Heinrich, A. J., Gupta, J. A., Lutz, C. P. & Eigler, D. M. Single-Atom Spin-Flip Spectroscopy. *Science* **306**, 466–469 (2004).

[57] Shirato, N., Cummings, M., Kersell, H., Li, Y., Stripe, B., Rosenmann, D., Hla, S.-W. & Rose, V. Elemental Fingerprinting of Materials with Sensitivity at the Atomic Limit. *Nano Letters* **14**, 6499–6504 (2014).

[58] Bardeen, J. Tunnelling from a Many-Particle Point of View. *Physical Review Letters* **6**, 57–59 (1961).

[59] Tersoff, J. & Hamann, D. R. Theory of the scanning tunneling microscope. *Physical Review B* **31**, 805–813 (1985).

[60] Lang, N. D. Spectroscopy of single atoms in the scanning tunneling microscope. *Physical Review B* **34**, 5947–5950 (1986).

[61] Selloni, A., Carnevali, P., Tosatti, E. & Chen, C. D. Voltage-dependent scanning-tunneling microscopy of a crystal surface: Graphite. *Physical Review B* **31**, 2602–2605 (1985).

[62] Stanford Research Systems. About Lock-In Amplifiers. URL `http://www.thinksrs.com/downloads/PDFs/ApplicationNotes/AboutLIAs.pdf`. Visited: 09/15/2016.

[63] Klein, J., Léger, A., Belin, M., Défourneau, D. & Sangster, M. J. L. Inelastic-Electron-Tunneling Spectroscopy of Metal-Insulator-Metal Junctions. *Physical Review B* **7**, 2336–2348 (1973).

[64] Kröger, J., Limot, L., Jensen, H., Berndt, R., Crampin, S. & Pehlke, E. Surface state electron dynamics of clean and adsorbate-covered metal surfaces studied with the scanning tunnelling microscope. *Progress in Surface Science* **80**, 26–48 (2005).

[65] Ho, W. Single-molecule chemistry. *The Journal of Chemical Physics* **117**, 11033–11061 (2002).

[66] Franke, K. J. and Pascual, J. I. Effects of electron–vibration coupling in transport through single molecules. *Journal of Physics: Condensed Matter* **24**, 394002 (2012).

[67] Besocke, K. An easily operable scanning tunneling microscope. *Surface Science* **181**, 145–153 (1987).

[68] Li, J., Schneider, W.-D. & Berndt, R. Local density of states from spectroscopic scanning-tunneling-microscope images: Ag(111). *Physical Review B* **56**, 7656–7659 (1997).

[69] Dante Gatteschi, Roberta Sessoli & Jacques Villain. *Molecular Nanomagnets* (Oxford University Press, 2006).

[70] De Haas, W. & Van Den Berg, G. The electrical resistance of gold and silver at low temperatures. *Physica* **3**, 440–449 (1936).

[71] Madhavan, V., Chen, W., Jamneala, T., Crommie, M. F. & Wingreen, N. S. Tunneling into a Single Magnetic Atom: Spectroscopic Evidence of the Kondo Resonance. *Science* **280**, 567–569 (1998).

[72] Li, J., Schneider, W.-D., Berndt, R. & Delley, B. Kondo Scattering Observed at a Single Magnetic Impurity. *Physical Review Letters* **80**, 2893–2896 (1998).

[73] Cronenwett, S. M., Oosterkamp, T. H. & Kouwenhoven, L. P. A Tunable Kondo Effect in Quantum Dots. *Science* **281**, 540–544 (1998).

[74] Goldhaber-Gordon, D., Göres, J., Kastner, M. A., Shtrikman, H., Mahalu, D. & Meirav, U. From the Kondo Regime to the Mixed-Valence Regime in a Single-Electron Transistor. *Physical Review Letters* **81**, 5225–5228 (1998).

[75] Kouwenhoven, L. and Glazman, L. Revival of the Kondo effect. *Physics World* **14**, 33 (2001).

[76] Hewson, A. C. *The Kondo Problem to Heavy Fermions* (Cambridge University Press, 1997).

[77] Zhao, A. *et al.* Controlling the Kondo Effect of an Adsorbed Magnetic Ion Through Its Chemical Bonding. *Science* **309**, 1542–1544 (2005).

[78] Iancu, V., Deshpande, A. & Hla, S.-W. Manipulating Kondo Temperature via Single Molecule Switching. *Nano Letters* **6**, 820–823 (2006).

[79] Dubout, Q. *et al.* Controlling the Spin of Co Atoms on Pt(111) by Hydrogen Adsorption. *Phys. Rev. Lett.* **114**, 106807 (2015).

[80] Ternes, M. and Heinrich, A. J. and Schneider, W.-D. Spectroscopic manifestations of the Kondo effect on single adatoms. *Journal of Physics: Condensed Matter* **21**, 053001 (2009).

[81] Liu, L. *et al.* Revealing the Atomic Site-Dependent g Factor within a Single Magnetic Molecule via the Extended Kondo Effect. *Physical Review Letters* **114**, 126601 (2015).

[82] Anderson, P. W. Localized Magnetic States in Metals. *Physical Review* **124**, 41–53 (1961).

[83] Baruselli, P. P., Requist, R., Fabrizio, M. & Tosatti, E. Ferromagnetic Kondo Effect in a Triple Quantum Dot System. *Physical Review Letters* **111**, 047201 (2013).

[84] van der Wiel, W. G., Franceschi, S. D., Fujisawa, T., Elzerman, J. M., Tarucha, S. & Kouwenhoven, L. P. The Kondo Effect in the Unitary Limit. *Science* **289**, 2105 (2000).

[85] Haldane, F. D. M. Scaling Theory of the Asymmetric Anderson Model. *Physical Review Letters* **40**, 416–419 (1978).

[86] Nagaoka, K., Jamneala, T., Grobis, M. & Crommie, M. F. Temperature Dependence of a Single Kondo Impurity. *Physical Review Letters* **88**, 077205 (2002).

[87] Wahl, P., Diekhöner, L., Schneider, M. A., Vitali, L., Wittich, G. & Kern, K. Kondo Temperature of Magnetic Impurities at Surfaces. *Physical Review Letters* **93**, 176603 (2004).

[88] Knorr, N., Schneider, M. A., Diekhöner, L., Wahl, P. & Kern, K. Kondo Effect of Single Co Adatoms on Cu Surfaces. *Physical Review Letters* **88**, 096804 (2002).

[89] Limot, L. & Berndt, R. Kondo effect and surface-state electrons. *Proceedings of the Seventh International Symposium on Atomically Controlled Surfaces, Interfaces and Nanostructures* **237**, 572–576 (2004).

[90] Choi, D.-J., Rastei, M. V., Simon, P. & Limot, L. Conductance-Driven Change of the Kondo Effect in a Single Cobalt Atom. *Physical Review Letters* **108**, 266803 (2012).

[91] Fano, U. Effects of Configuration Interaction on Intensities and Phase Shifts. *Physical Review* **124**, 1866–1878 (1961).

[92] Frota, H. O. & Oliveira, L. N. Photoemission spectroscopy for the spin-degenerate Anderson model. *Physical Review B* **33**, 7871–7874 (1986).

[93] Frota, H. O. Shape of the Kondo resonance. *Phys. Rev. B* **45**, 1096–1099 (1992).

[94] Frank, S. & Jacob, D. Orbital signatures of Fano-Kondo line shapes in STM adatom spectroscopy. *Physical Review B* **92**, 235127 (2015).

[95] Costi, T. A. Kondo Effect in a Magnetic Field and the Magnetoresistivity of Kondo Alloys. *Physical Review Letters* **85**, 1504–1507 (2000).

[96] Quay, C. H. L., Cumings, J., Gamble, S. J., Picciotto, R. d., Kataura, H. & Goldhaber-Gordon, D. Magnetic field dependence of the spin-1/2 and spin-1 Kondo effects in a quantum dot. *Physical Review B* **76**, 245311 (2007).

[97] Žitko, R., Peters, R. & Pruschke, T. Splitting of the Kondo resonance in anisotropic magnetic impurities on surfaces. *New Journal of Physics* **11**, 053003 (2009).

[98] Anderson, P. W. Localized Magnetic States and Fermi-Surface Anomalies in Tunneling. *Physical Review Letters* **17**, 95–97 (1966).

[99] Appelbaum, J. "s-d" Exchange Model of Zero-Bias Tunneling Anomalies. *Physical Review Letters* **17**, 91–95 (1966).

[100] Appelbaum, J. A. Exchange Model of Zero-Bias Tunneling Anomalies. *Physical Review* **154**, 633–643 (1967).

[101] Zhang, Y.-h. *et al.* Temperature and magnetic field dependence of a Kondo system in the weak coupling regime. *Nat Commun* **4** (2013).

[102] Ternes, M. Spin excitations and correlations in scanning tunneling spectroscopy. *New Journal of Physics* **17**, 063016 (2015).

[103] Kammerlingh Onnes, H. *Proc. K. Ned. Akad. Wet.* **13**, 1274 (1911).

[104] Kammerlingh Onnes, H. *Proc. K. Ned. Akad. Wet.* **14**, 113 (1911).

[105] van Delft, D. & Kes, P. The discovery of superconductivity. *Europhysics News* **42**, 21–25 (2011).

[106] Clay, J. & Kammerlingh Onnes, H. On the change of the resistance of metals at very low temperatures and the influence excerted on it by small amounts of mixtures. I. *KNAW, Proceedings* **10 I**, 207–215 (1907).

[107] Cooper, L. N. Bound Electron Pairs in a Degenerate Fermi Gas. *Physical Review* **104**, 1189–1190 (1956).

[108] Carsten Timm. Theory of Superconductivity (2016). URL `https://www.physik.tu-dresden.de/~timm/personal/teaching/thsup_w11/Theory_of_Superconductivity.pdf`. Visited: 09/30/2016.

[109] M. Tinkham. *Introduction to Superconductivity* (Dover Publications Inc., 2004), second edn.

[110] Bardeen, J., Cooper, L. N. & Schrieffer, J. R. Theory of Superconductivity. *Physical Review* **108**, 1175–1204 (1957).

[111] Bardeen, J., Cooper, L. N. & Schrieffer, J. R. Microscopic Theory of Superconductivity. *Physical Review* **106**, 162–164 (1957).

[112] Anderson, P. Theory of dirty superconductors. *Journal of Physics and Chemistry of Solids* **11**, 26–30 (1959).

[113] Flatté, M. E. & Byers, J. M. Local Electronic Structure of a Single Magnetic Impurity in a Superconductor. *Physical Review Letters* **78**, 3761–3764 (1997).

[114] Flatté, M. E. & Byers, J. M. Local electronic structure of defects in superconductors. *Physical Review B* **56**, 11213–11231 (1997).

[115] Sakurai, A. Comments on Superconductors with Magnetic Impurities. *Progress of Theoretical Physics* **44**, 1472–1476 (1970).

[116] Salkola, M. I., Balatsky, A. V. & Schrieffer, J. R. Spectral properties of quasiparticle excitations induced by magnetic moments in superconductors. *Physical Review B* **55**, 12648–12661 (1997).

[117] Balatsky, A. V., Vekhter, I. & Zhu, J.-X. Impurity-induced states in conventional and unconventional superconductors. *Reviews of Modern Physics* **78**, 373–433 (2006).

[118] Ruby, M., Pientka, F., Peng, Y., von Oppen, F., Heinrich, B. W. & Franke, K. J. Tunneling Processes into Localized Subgap States in Superconductors. *Physical Review Letters* **115**, 087001 (2015).

[119] Matsuura, T. The Effects of Impurities on Superconductors with Kondo Effect. *Progress of Theoretical Physics* **57**, 1823–1835 (1977).

[120] Satori, K., Shiba, H., Sakai, O. & Shimizu, Y. Numerical Renormalization Group Study of Magnetic Impurities in Superconductors. *Journal of the Physical Society of Japan* **61**, 3239–3254 (1992).

[121] Sakai, O., Shimizu, Y., Shiba, H. & Satori, K. Numerical Renormalization Group Study of Magnetic Impurities in Superconductors. II. Dynamical Excitation Spectra and Spatial Variation of the Order Parameter. *Journal of the Physical Society of Japan* **62**, 3181–3197 (1993).

[122] Deacon, R. S., Tanaka, Y., Oiwa, A., Sakano, R., Yoshida, K., Shibata, K., Hirakawa, K. & Tarucha, S. Tunneling Spectroscopy of Andreev Energy Levels in a Quantum Dot Coupled to a Superconductor. *Physical Review Letters* **104**, 076805 (2010).

[123] Lee, E. J. H., Jiang, X., Houzet, M., Aguado, R., Lieber, C. M. & De Franceschi, S. Spin-resolved Andreev levels and parity crossings in hybrid superconductor-semiconductor nanostructures. *Nat Nano* **9**, 79–84 (2014).

[124] Hatter, N., Heinrich, B. W., Ruby, M., Pascual, J. I. & Franke, K. J. Magnetic anisotropy in Shiba bound states across a quantum phase transition. *Nat Commun* **6** (2015).

[125] Liang, W., Shores, M. P., Bockrath, M., Long, J. R. & Park, H. Kondo resonance in a single-molecule transistor. *Nature* **417**, 725–729 (2002).

[126] Xiang, D., Jeong, H., Kim, D., Lee, T., Cheng, Y., Wang, Q. & Mayer, D. Three-Terminal Single-Molecule Junctions Formed by Mechanically Controllable Break Junctions with Side Gating. *Nano Letters* **13**, 2809–2813 (2013).

[127] Grill, L., Rieder, K.-H., Moresco, F., Rapenne, G., Stojkovic, S., Bouju, X. & Joachim, C. Rolling a single molecular wheel at the atomic scale. *Nat Nano* **2**, 95–98 (2007).

[128] Tierney, H. L. *et al.* Experimental demonstration of a single-molecule electric motor. *Nat Nano* **6**, 625–629 (2011).

[129] Irie, M. Diarylethenes for Memories and Switches. *Chemical Reviews* **100**, 1685–1716 (2000).

[130] B. Feringa. *Molecular Switches* (Wiley-VCH: Weinheim, 2001), 2nd edn.

[131] Comstock, M. J. *et al.* Determination of Photoswitching Dynamics through Chiral Mapping of Single Molecules Using a Scanning Tunneling Microscope. *Physical Review Letters* **104**, 178301 (2010).

[132] Qiu, X. H., Nazin, G. V. & Ho, W. Mechanisms of Reversible Conformational Transitions in a Single Molecule. *Physical Review Letters* **93**, 196806 (2004).

[133] Henzl, J., Mehlhorn, M., Gawronski, H., Rieder, K.-H. & Morgenstern, K. Reversible cis–trans Isomerization of a Single Azobenzene Molecule. *Angewandte Chemie International Edition* **45**, 603–606 (2006).

[134] Feringa, B. L. The Art of Building Small: From Molecular Switches to Molecular Motors. *The Journal of Organic Chemistry* **72**, 6635–6652 (2007).

[135] Tegeder, P. Optically and thermally induced molecular switching processes at metal surfaces. *Journal of Physics: Condensed Matter* **24**, 394001 (2012).

[136] Mielke, J. *et al.* Imine Derivatives on Au(111): Evidence for "Inverted" Thermal Isomerization. *ACS Nano* **5**, 2090–2097 (2011).

[137] Shimizu, T. K., Jung, J., Imada, H. & Kim, Y. Adsorption-induced stability reversal of photochromic diarylethene on metal surfaces. *Chemical Communications* **49**, 8710–8712 (2013).

[138] Schmidt, P. M., Horn, K., Hugo Dil, J. & Kampen, T. U. Conformational isomers of stilbene on Si(100). *Surface Science* **601**, 1775–1780 (2007).

[139] Piantek, M., Miguel, J., Krüger, A., Navío, C., Bernien, M., Ball, D. K., Hermann, K. & Kuch, W. Temperature, Surface, and Coverage-Induced Conformational Changes of Azobenzene Derivatives on Cu(001). *The Journal of Physical Chemistry C* **113**, 20307–20315 (2009).

[140] Bronner, C., Schulze, M., Hagen, S. & Tegeder, P. The influence of the electronic structure of adsorbate–substrate complexes on photoisomerization ability. *New Journal of Physics* **14**, 043023 (2012).

[141] Bronner, C., Priewisch, B., Rück-Braun, K. & Tegeder, P. Photoisomerization of an Azobenzene on the Bi(111) Surface. *The Journal of Physical Chemistry C* **117**, 27031–27038 (2013).

[142] Henningsen, N., Rurali, R., Franke, K. J., Fernández-Torrente, I. & Pascual, J. I. Trans to cis isomerization of an azobenzene derivative on a Cu(100) surface. *Applied Physics A* **93**, 241–246 (2008).

[143] Tam, E. S. *et al.* Single-Molecule Conductance of Pyridine-Terminated Dithienylethene Switch Molecules. *ACS Nano* **5**, 5115–5123 (2011).

[144] Kim, Y. *et al.* Charge Transport Characteristics of Diarylethene Photoswitching Single-Molecule Junctions. *Nano Letters* **12**, 3736–3742 (2012).

[145] Briechle, B., Kim, Y., Ehrenreich, P., Erbe, A., Sysoiev, D., Huhn, T., Groth, U. & Scheer, E. Current–voltage characteristics of single-molecule diarylethene junctions measured with adjustable gold electrodes in solution. *Beilstein Journal of Nanotechnology* **3**, 798–808 (2012).

[146] Katsonis, N., Kudernac, T., Walko, M., van der Molen, S., van Wees, B. & Feringa, B. Reversible Conductance Switching of Single Diarylethenes on a Gold Surface. *Advanced Materials* **18**, 1397–1400 (2006).

[147] Arramel, Pijper, T., Kudernac, T., Katsonis, N., van der Maas, M., Feringa, B. & van Wees, B. Reversible light induced conductance switching of asymmetric diarylethenes on gold: surface and electronic studies. *Nanoscale* **5**, 9277–9282 (2013).

[148] Pakiari, A. H. & Jamshidi, Z. Nature and strength of M-S Bonds (M = Au, Ag, and Cu) in Binary Alloy Gold Clusters. *The Journal of Physical Chemistry A* **114**, 9212–9221 (2010).

[149] Woodward, R. B. & Hoffmann, R. The Conservation of Orbital Symmetry. *Angewandte Chemie International Edition in English* **8**, 781–853 (1969).

[150] Rob Knowles. The Conservation of Orbital Symmetry (2007). URL `https://www.princeton.edu/chemistry/macmillan/group-meetings/RRK-orbital.pdf`. Visited: 10/10/2016.

[151] Wirth, J. *et al.* Diarylethene Molecules on a Ag(111) Surface: Stability and Electron-Induced Switching. *The Journal of Physical Chemistry C* **119**, 4874–4883 (2015).

[152] Nguyen, M.-T., Pignedoli, C. A., Treier, M., Fasel, R. & Passerone, D. The role of van der Waals interactions in surface-supported supramolecular networks. *Physical Chemistry Chemical Physics* **12**, 992–999 (2010).

[153] Toyama, T., Higashiguchi, K., Nakamura, T., Yamaguchi, H., Kusaka, E. & Matsuda, K. Photoswitching of Conductance of Diarylethene–Gold Nanoparticle Network Based on the Alteration of π-Conjugation. *The Journal of Physical Chemistry Letters* **7**, 2113–2118 (2016).

[154] Perdew, J. P. Density functional theory and the band gap problem. *International Journal of Quantum Chemistry* **28**, 497–523 (1985).

[155] Menzel, D. & Gomer, R. Desorption from Metal Surfaces by Low-Energy Electrons. *The Journal of Chemical Physics* **41**, 3311–3328 (1964).

[156] Redhead, P. A. Interaction of Slow Electrons with Chemisorbed Oxygen. *Canadian Journal of Physics* **42**, 886–905 (1964).

[157] Antoniewicz, P. Model for electron- and photon-stimulated desorption. *Physical Review B* **21**, 3811–3815 (1980).

[158] Wirth, J. A. *Chemische Reaktionen in Substrat-Adsorbat-Systemen*. Doctoral Thesis, University of Potsdam (2014). URL `https://publishup.uni-potsdam.de/opus4-ubp/frontdoor/index/index/docId/7244`.

[159] Iavarone, M. and Karapetrov, G. and Fedor, J. and Rosenmann, D. and Nishizaki, T. and Kobayashi, N. The local effect of magnetic impurities on superconductivity in Co x NbSe 2 and Mn x NbSe 2 single crystals. *Journal of Physics: Condensed Matter* **22**, 015501 (2010).

[160] Ginsberg, D. M. Consequences of Shiba's theory of magnetic impurities in superconductors, beyond s-wave scattering. *Physical Review B* **20**, 960–962 (1979).

[161] Kunz, A. B. & Ginsberg, D. M. Band calculation of the effect of magnetic impurity atoms on the properties of superconductors. *Physical Review B* **22**, 3165–3172 (1980).

[162] Moca, C. P., Demler, E., Jankó, B. & Zaránd, G. Spin-resolved spectra of Shiba multiplets from Mn impurities in MgB_2. *Physical Review B* **77**, 174516 (2008).

[163] Golež, D., Bonča, J. & Žitko, R. Vibrational Andreev bound states in magnetic molecules. *Physical Review B* **86**, 085142 (2012).

[164] Žitko, R., Bodensiek, O. & Pruschke, T. Effects of magnetic anisotropy on the subgap excitations induced by quantum impurities in a superconducting host. *Physical Review B* **83**, 054512 (2011).

[165] Kim, Y., Zhang, J., Rossi, E. & Lutchyn, R. M. Impurity-Induced Bound States in Superconductors with Spin-Orbit Coupling. *Phys. Rev. Lett.* **114**, 236804 (2015).

[166] Ji, S.-H. and Fu, Y.-S. and Zhang, T. and Chen, X. and Jia, J.-F. and Xue, Q.-K. and Ma, X.-C. Kondo Effect in Self-Assembled Manganese Phthalocyanine Monolayer on Pb Islands. *Chinese Physics Letters* **27**, 087202 (2010).

[167] Stróżecka, A., Soriano, M., Pascual, J. I. & Palacios, J. J. Reversible Change of the Spin State in a Manganese Phthalocyanine by Coordination of CO Molecule. *Physical Review Letters* **109**, 147202 (2012).

[168] Kügel, J., Karolak, M., Senkpiel, J., Hsu, P.-J., Sangiovanni, G. & Bode, M. Relevance of Hybridization and Filling of 3d Orbitals for the Kondo Effect in Transition Metal Phthalocyanines. *Nano Letters* **14**, 3895–3902 (2014).

[169] Ruby, M., Heinrich, B. W., Pascual, J. I. & Franke, K. J. Experimental Demonstration of a Two-Band Superconducting State for Lead Using Scanning Tunneling Spectroscopy. *Physical Review Letters* **114**, 157001 (2015).

[170] Hao, D., Song, C., Ning, Y., Wang, Y., Wang, L., Ma, X.-C., Chen, X. & Xue, Q.-K. Self-assembly of manganese phthalocyanine on Pb(111) surface: A scanning tunneling microscopy study. *The Journal of Chemical Physics* **134** (2011).

[171] Liao, M.-S., Watts, J. D. & Huang, M.-J. DFT Study of Unligated and Ligated ManganeseII Porphyrins and Phthalocyanines. *Inorganic Chemistry* **44**, 1941–1949 (2005).

[172] Jacob, D., Soriano, M. & Palacios, J. J. Kondo effect and spin quenching in high-spin molecules on metal substrates. *Phys. Rev. B* **88**, 134417 (2013).

[173] Kügel, J., Karolak, M., Krönlein, A., Senkpiel, J., Hsu, P.-J., Sangiovanni, G. & Bode, M. State identification and tunable Kondo effect of MnPc on Ag(001). *Physical Review B* **91**, 235130 (2015).

[174] Tsukahara, N. *et al.* Adsorption-Induced Switching of Magnetic Anisotropy in a Single Iron(II) Phthalocyanine Molecule on an Oxidized Cu(110) Surface. *Physical Review Letters* **102**, 167203 (2009).

[175] Nadj-Perge, S. *et al.* Observation of Majorana fermions in ferromagnetic atomic chains on a superconductor. *Science* **346**, 602–607 (2014).

[176] Ghosh, D., Parida, P. & Pati, S. K. Spin-State Switching of Manganese Porphyrin by Conformational Modification. *The Journal of Physical Chemistry C* **120**, 3625–3634 (2016).

[177] Otte, A. F., Ternes, M., von Bergmann, K., Loth, S., Brune, H., Lutz, C. P., Hirjibehedin, C. F. & Heinrich, A. J. The role of magnetic anisotropy in the Kondo effect. *Nat Phys* **4**, 847–850 (2008).

[178] Jacobson, P., Herden, T., Muenks, M., Laskin, G., Brovko, O., Stepanyuk, V., Ternes, M. & Kern, K. Quantum engineering of spin and anisotropy in magnetic molecular junctions. *Nature Communications* **6**, 8536 (2015).

[179] Flechtner, K., Kretschmann, A., Steinrück, H.-P. & Gottfried, J. M. NO-Induced Reversible Switching of the Electronic Interaction between a Porphyrin-Coordinated Cobalt Ion and a Silver Surface. *Journal of the American Chemical Society* **129**, 12110–12111 (2007).

[180] Seufert, K., Auwärter, W. & Barth, J. V. Discriminative Response of Surface-Confined Metalloporphyrin Molecules to Carbon and Nitrogen Monoxide. *Journal of the American Chemical Society* **132**, 18141–18146 (2010).

[181] Isvoranu, C., Wang, B., Ataman, E., Knudsen, J., Schulte, K., Andersen, J. N., Bocquet, M.-L. & Schnadt, J. Comparison of the Carbonyl and Nitrosyl Complexes Formed by Adsorption of CO and NO on Monolayers of Iron Phthalocyanine on Au(111). *The Journal of Physical Chemistry C* **115**, 24718–24727 (2011).

[182] Isvoranu, C., Wang, B., Ataman, E., Schulte, K., Knudsen, J., Andersen, J. N., Bocquet, M.-L. & Schnadt, J. Pyridine Adsorption on Single-Layer Iron Phthalocyanine on Au(111). *The Journal of Physical Chemistry C* **115**, 20201–20208 (2011).

[183] Hermanns, C. F. and Bernien, M. and Krüger, A. and Miguel, J. and Kuch, W. Switching the electronic properties of Co-octaethylporphyrin molecules on oxygen-covered Ni films by NO adsorption. *Journal of Physics: Condensed Matter* **24**, 394008 (2012).

[184] Zhang, J. L. *et al.* Single-Molecule Imaging of Activated Nitrogen Adsorption on Individual Manganese Phthalocyanine. *Nano Letters* **15**, 3181–3188 (2015).

[185] Hieringer, W. *et al.* The Surface Trans Effect: Influence of Axial Ligands on the Surface Chemical Bonds of Adsorbed Metalloporphyrins. *Journal of the American Chemical Society* **133**, 6206–6222 (2011).

[186] Heinrich, B. W., Braun, L., Pascual, J. I. & Franke, K. J. Tuning the Magnetic Anisotropy of Single Molecules. *Nano Letters* **15**, 4024–4028 (2015).

[187] Isvoranu, C. and Wang, B. and Schulte, K. and Ataman, E. and Knudsen, J. and Andersen, J. N. and Bocquet, M. L. and Schnadt, J. Tuning the spin state of iron phthalocyanine by ligand adsorption. *Journal of Physics: Condensed Matter* **22**, 472002 (2010).

[188] Wackerlin, C. *et al.* On-surface coordination chemistry of planar molecular spin systems: novel magnetochemical effects induced by axial ligands. *Chemical Science* **3**, 3154–3160 (2012).

[189] Gopakumar, T. G., Tang, H., Morillo, J. & Berndt, R. Transfer of Cl Ligands between Adsorbed Iron Tetraphenylporphyrin Molecules. *Journal of the American Chemical Society* **134**, 11844–11847 (2012).

[190] Pascual, J. I., Lorente, N., Song, Z., Conrad, H. & Rust, H.-P. Selectivity in vibrationally mediated single-molecule chemistry. *Nature* **423**, 525–528 (2003).

[191] Lorente, N., Pascual, J. I. & Ueba, H. Two-electron processes of desorption of a single ammonia molecule from Cu(100). *Surface Science* **593**, 122 – 132 (2005). Proceedings of the Tenth International Workshop on Desorption Induced by Electronic Transitions.

[192] Wäckerlin, C. *et al.* Ammonia Coordination Introducing a Magnetic Moment in an On-Surface Low-Spin Porphyrin. *Angewandte Chemie International Edition* **52**, 4568–4571 (2013).

[193] Isvoranu, C., Wang, B., Ataman, E., Schulte, K., Knudsen, J., Andersen, J. N., Bocquet, M.-L. & Schnadt, J. Ammonia adsorption on iron phthalocyanine on Au(111): Influence on adsorbate–substrate coupling and molecular spin. *The Journal of Chemical Physics* **134** (2011).

[194] Oberg, J. C., Calvo, M. R., Delgado, F., Moro-Lagares, M., Serrate, D., Jacob, D., Fernandez-Rossier, J. & Hirjibehedin, C. F. Control of single-spin magnetic anisotropy by exchange coupling. *Nat Nano* **9**, 64–68 (2014).

[195] Berggren, P. & Fransson, J. Theory of spin inelastic tunneling spectroscopy for superconductor-superconductor and superconductor-metal junctions. *Physical Review B* **91**, 205438 (2015).

[196] Cohen, R. W. & Abeles, B. Superconductivity in Granular Aluminum Films. *Physical Review* **168**, 444–450 (1968).

[197] Kohen, A., Noat, Y., Proslier, T., Lacaze, E., Aprili, M., Sacks, W. & Roditchev, D. Fabrication and characterization of scanning tunneling microscopy superconducting Nb tips having highly enhanced critical fields. *Physica C: Superconductivity* **419**, 18–24 (2005).

[198] Minamitani, E., Tsukahara, N., Matsunaka, D., Kim, Y., Takagi, N. & Kawai, M. Symmetry-Driven Novel Kondo Effect in a Molecule. *Physical Review Letters* **109**, 086602 (2012).

[199] Lauhon, L. & Ho, W. Effects of temperature and other experimental variables on single molecule vibrational spectroscopy with the scanning tunneling microscope. *Review of Scientific Instruments* **72**, 216–223 (2001).

[200] Nozières, P. A "fermi-liquid" description of the Kondo problem at low temperatures. *Journal of Low Temperature Physics* **17**, 31–42 (1974).

[201] Costi, T. A. and Hewson, A. C. and Zlatic, V. Transport coefficients of the Anderson model via the numerical renormalization group. *Journal of Physics: Condensed Matter* **6**, 2519 (1994).

[202] Léonard, C., Handy, N. C., Carter, S. & Bowman, J. M. The vibrational levels of ammonia. *Spectrochimica Acta Part A: Molecular and Biomolecular Spectroscopy* **58**, 825–838 (2002).

[203] Lauhon, L. J. & Ho, W. Single-molecule vibrational spectroscopy and microscopy: CO on Cu(001) and Cu(110). *Physical Review B* **60**, R8525–R8528 (1999).

[204] Burema, S. R., Seufert, K., Auwärter, W., Barth, J. V. & Bocquet, M.-L. Probing Nitrosyl Ligation of Surface-Confined Metalloporphyrins by Inelastic Electron Tunneling Spectroscopy. *ACS Nano* **7**, 5273–5281 (2013).

[205] Parks, J. J. *et al.* Mechanical Control of Spin States in Spin-1 Molecules and the Underscreened Kondo Effect. *Science* **328**, 1370–1373 (2010).

[206] Žitko, R., Peters, R. & Pruschke, T. Properties of anisotropic magnetic impurities on surfaces. *Physical Review B* **78**, 224404 (2008).

[207] Ruby, M. SpectraFox: A free open-source data management and analysis tool for scanning probe microscopy and spectroscopy. *SoftwareX* (2016).

[208] Dynes, R. C., Narayanamurti, V. & Garno, J. P. Direct Measurement of Quasiparticle-Lifetime Broadening in a Strong-Coupled Superconductor. *Physical Review Letters* **41**, 1509–1512 (1978).

List of Abbreviations

AFM	atomic force microscopy
DOS	(local) density of states
DFT	density functional theory
FeOEP-Cl	iron octaethylporphyrine-chlorine
FePc	iron phthalocyanine
HOMO	highest occupied molecular orbital
HWHM	half width at half maximum
LUMO	lowest unoccupied molecular orbital
MEP	minimum energy path
MnPc	manganese phthalocyanine
MnPc-NH_3	manganese phthalocyanine (ammonia ligated)
NEB	nudged elastic band
PDOS	site-projected density of states
STM	(low temperature) scanning tunneling microscopy
STS	scanning tunneling spectroscopy
UHV	ultra high vacuum
XMCD	X-ray magnetic circular dichroism
XPS	X-ray photoemission spectroscopy

List of Publications

J. Wirth, N. Hatter, R. Drost, T. R. Umbach, S. Barja, M. Zastrow, K. Rück-Braun, J. I. Pascual, P. Saalfrank and K. J. Franke
Diarylethene Molecules on a Ag(111) Surface: Stability and Electron-Induced Switching
The Journal of Physical Chemistry C **119**, 4874-4883 (2015)

N. Hatter, B. W. Heinrich, M. Ruby, J. I. Pascual and K. J. Franke
Magnetic anisotropy in Shiba bound states across a quantum phase transition
Nature Communications, **6:8988** (2015)

Conference Contributions

2013

- Workshop of the SFB 658-Integrated Research Training Group, Zeuthen, Germany 16.05 - 17.05.2013
  (Oral presentation) *Probing the spin state and magnetic anisotropy of metalorganic molecules on a superconductor*

- 543^{th} WE-Heraeus Seminar: Electron Transport through Atoms, Molecules and Nanowires: Advances in Experiment and Theory, Bad Honnef, Germany, 28.10 - 31.10.2013
  (Poster) *Diarylethene molecules on a Ag(111) surface: stability and electric-field induced switching of single molecules*

2014

- DPG Spring Meeting of the Condensed Matter Section, Dresden, Germany, 30.03 - 04.04.2014
  (Oral presentation) *Diarylethene molecules on a Ag(111) surface: stability and electric-field induced switching of single molecules*

- 563^{th} WE-Heraeus Seminar: Functional Molecules at Surfaces, Bad Honnef, Germany, 19.05 - 21.05.2014
  (Poster) *Diarylethene molecules on a Ag(111) surface: stability and electric-field induced switching of single molecules*

- Summer School of the International Max Planck Research School for Condensed Matter Science:
  Superconductivity and Magnetism at the Nanoscale, Stuttgart, Germany, 30.06 - 03.07.2014
  (Poster) *Surface-assisted ring-closure reaction of a low-spin porphyrin complex*

- Workshop of the SFB 658-Integrated Research Training Group, Lübbenau, Germany 09.10 - 10.10.2014
  (Oral presentation) *Diarylethene molecules on a Ag(111) surface: stability and electric-field induced switching of single molecules*

2015

- DPG Spring Meeting of the Condensed Matter Section, Berlin, Germany, 15.03 - 20.03.2015
  (Poster) *On-surface reactions of porphin molecules on Au(111)*

- European Conference on Surface Science (ECOSS) 31, Barcelona, Spain, 31.08 - 04.09.2015
  (Poster) *On-surface reactions of porphin molecules on Au(111)*

- 598^{th} WE-Heraeus Seminar: Frontiers in Scanning Probe Microscopy, Bad Honnef, Germany, 2.11. - 5.11.2015 (Poster) *Magnetic anisotropy in Shiba bound states across a quantum phase transition*

2016

- DPG Spring Meeting of the Condensed Matter Section, Regensburg, Germany, 06.03 - 11.03.2016
  (Oral presentation) *Magnetic anisotropy in Shiba bound states across a quantum phase transition*

Acknowledgements

As most things in life, also this thesis would not have been possible without the help of many people.

First, I would like to express my deep gratitude towards Prof. Katharina Franke, who gave me the opportunity to continue my research studies in her group. She was always helpful in all matters. I could always come to her office and ask all the questions I had. Katharina always tries to create a good group spirit, which is essential for a good collaboration within the group. This is a special trait, which I value a lot.

I also want to thank Prof. Martin Wolf from the Fritz Haber Institut, for accepting to be my second supervisor.

Benjamin Heinrich always gave a helping hand and shared good ideas. He taught me everything I know about STM and how to deal with the specialties of different machines. I also thank him for proof-reading a couple of the chapters of this thesis.

I thank Michael Ruby as a friend and colleague, who adjusted his program SpectraFox according to all the wishes I had. He also inspired me with his work ethic to push a bit more everytime. Besides that, I also thank him for the good times we had on various conferences.

Special thanks goes also to Daniela Rolf and Isabel Fernandez-Torrente, who read many chapters of this thesis and gave valuable feedback on them. Daniela also supported me mentally in the times when writing was frustrating and always happily joined me in thinking about scientific problems.

I also want to thank all other present and former members of AG Franke, with whom I crossed ways during my time here: Gelavizh Ahmadi, Wibke Bronsch, Bo Chen, Xianwen Chen, Laetitia Farinacci, Marc Font Gual, Janina Ladenthin, Julia Läger, Eva Liebhaber, Philip Loche, Christian Lotze, Nils Krane, Nikolai Paßler, Olof Peters, Gael Reecht, Andreas Riemann, Sonja Schubert, Rika Simon, Paul Stoll, Sergey Trishin, Tobias Umbach, Max Weigand, Kristina Weinel and Clemens Winkelmann.

Birgit Dabisch always helped with the bureaucracy and took care of the things that need to be done, but nobody usually sees. Thank you for that. I also thank Christian Roth, who helped us to repair the microsopes more than once.

I am thankful for the fruitful collaboration with Jonas Wirth and Peter Saalfrank from University of Potsdam.

Markus Ternes provided us with his program, in which the perturbative approach of the Kondo effect is implemented. I am grateful for this helpful tool.

I want to thank my family for their support during all those year. They always gave me a place, where to disconnect from work. And they also encouraged me to in all my endeavours and believed in me. Thank you.

Financial support from the Freie Universität Berlin through the research project “Nanoscale“ and from the DFG through research project “FR 2726/4-1“ is gratefully acknowledged.

Selbstständigkeitserklärung

Hiermit erkläre ich, dass ich die vorliegende Arbeit selbständig und nur unter Verwendung der angegebenen Literatur und Hilfsmittel angefertigt habe. Zudem erkläre ich, dass diese Arbeit in keinem früheren Promotionsverfahren eingereicht und dort angenommen oder für ungenügend befunden wurde.

Berlin, 28. Oktober 2016